Lung Patient Treatment Plan Optimization in the Presence of Magnetic Fields

by

Daniel Alexander Musashi Tamagi

A thesis submitted in partial fulfillment of the requirements for the degree of

Master of Science

in

Medical Physics

Department of Oncology
University of Alberta

ABSTRACT

The integration of clinical linear accelerators (linacs) with magnetic resonance imaging (MRI) systems represent the next generation of image guidance technologies in radiotherapy. Linac-MR systems have several potential advantages over the current X-ray based state-of-the-art image guidance systems, including superior soft tissue contrast and real-time tumour tracking. However the main magnetic field of the MRI system can have significant effects on dose deposition in the patient, particularly in low density regions such as lung. In this work, we investigated the impact of magnetic fields and tissue heterogeneity on the inverse-planning process for a Linac-MR system. Two Linac-MR configurations were studied, where the main magnetic field of the MRI system was either parallel or perpendicular to the linac beam central axis. These two magnetic field orientations affect the patient dose distribution differently. A 10 beam stereotactic body radiation therapy treatment plan for a lung patient was simplified to 3 beams for this study. We used a research version of the RayStation treatment planning system, which implemented discrete superposition of user supplied Monte Carlo simulated beamlet dose kernels for dose calculation. Dose distributions were compared for three cases: 1) the magnetic field was ignored during treatment planning; 2) the magnetic field was modeled during the forward calculation stage only; and 3) the magnetic field was modeled throughout the planning process. Comparison of these cases helped to determine the importance of modeling the main magnetic field of the MRI at the optimization and forward calculation stages, respectively. The results showed that the magnetic field effects for the parallel Linac-MR configuration were minimal, and that the magnetic field could be likely ignored during inverse-planning without a significant degradation of plan quality. The magnetic field effects for the perpendicular

configuration were much more significant, and resulted in large dose inhomogeneity in the target volume when the magnetic field was ignored at either the optimization or forward calculation stage of the inverse-planning process.

PREFACE

This thesis is an original work by Daniel Alexander Musashi Tamagi. No part of this thesis has been previously published.

DEDICATION/ACKNOWLEDGMENTS

I would like to acknowledge the contributions of my supervisors Mr. Colin Field and Dr. Brad Warkentin, my supervisory committee (Dr. Gino Fallone, Dr. Satyapal Rathee, Dr Matthew Larocque), and of my colleague Dr. Amir Keyvanloo. I thank them for their support, guidance, encouragement, patience, and kindness in helping me to complete this research and my Masters Thesis.

TABLE OF CONTENTS

List of Tables

List of Figures

Chapter 1: Introduction

Two out of every five Canadians will be diagnosed with some form of cancer in their lifetime according to 2010 estimates by the government of Canada. It is the leading cause of mortality, accounting for 30% of all deaths in Canada (1). It is therefore no surprise that cancer care research and clinical practice are of great interest to Canadians. This chapter will paint a broad picture of the evolution of radiotherapy since the discovery of X-rays and radioactivity at the turn of the 20th century. It will discuss the impact of large developments in radiotherapy technology and practice that have resulted in major improvements in the quality of care provided to cancer patients. Finally it will introduce one such development, the work being done on integrating magnetic resonance imaging (MRI) devices with clinical treatment units for advanced image guided radiotherapy treatments. I will describe the significance of this work within the context of radiotherapy as a whole, and the motivation for my research based on the current state of the art.

1.1 The History of Radiotherapy

1.1.1 X-rays, Radioactivity, and their Early Applications in Medicine

X-rays were first discovered in 1895 by the German physicist William Röntgen while performing research on the discharge of high voltages through gases in Crookes vacuum tubes (2, 3). Röntgen was fascinated by these strange invisible rays, which travelled in straight lines, were not deflected by magnetic fields, and could penetrate through solid objects. Unlike anything that could be explained by contemporary science, he dubbed this unusual radiation "*X*"-rays for

"*unknown"*. Röntgen's research would prove to be one of the most significant scientific discoveries of all time, and would lead to countless other innovations over the following century (and beyond). One such groundbreaking invention was the field of Röntgen photography, which would later become known as radiography. The penetrating power of X-rays allowed them to expose photographic plates through solid objects of sufficiently low density. He used this process to produce the world's first radiograph of his wife's hand (and wedding ring), shown in Figure 1.1 below (2). Although X-ray imaging is something that we take for granted today, the ability to non-invasively see inside the human body was a miraculous and revolutionary innovation at the time. This new technology would have a profound impact on the medical sciences, and for his groundbreaking research on X-rays Röntgen was awarded the first Nobel Prize in Physics in 1901 (4).

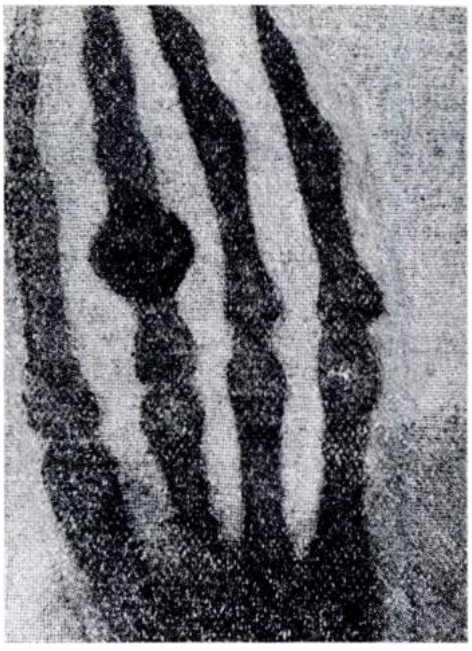

Figure 1.1: The world's first radiograph of Röntgen's wife's hand, with her wedding ring (2).

Röntgen's research became the hot topic of the contemporary scientific community, and prompted a worldwide frenzy of scientific research into X-rays and their applications (3). The

curiosity sparked by his discovery would result in the discovery of radioactivity a year later by French scientist Henri Becquerel (5, 6). Upon discovering that photographic plates stored in darkness next to a mineral containing uranium had been exposed, Becquerel theorized that phosphorescent materials might emit X-ray like radiation. After further investigation, he was surprised to discover that uranium salts spontaneously emitted this radiation without any need for external stimulation or energy, unlike the X-rays produced by vacuum tubes (6). His research was carried on by two other scientists in his lab, Marie and Pierre Curie. Becquerel and the Curies are considered the pioneers of radioactivity research, and shared the Nobel Prize in Physics in 1903 for their contributions (7). Marie Curie was later awarded the Nobel Prize in Chemistry in 1911 for her work on polonium and radium, making her the first person (and the only woman ever) to be awarded two Nobel Prizes (7). French physicist Paul Villard would discover the electromagnetic component of radioactive decay in 1900 while studying radium, although his discovery is seldom discussed beneath the shadows of Röntgen, Becquerel, and the Curies (8). British physicist Ernest Rutherford would name this radiation "gamma rays" in a publication in 1903, due to their superior penetrating power relative to the other products of the radioactive decay of radium, alpha (helium nuclei) and beta particles (electrons) (9).

Despite little being known about the dangers of ionizing radiation, it wasn't long before they were being used in a long list of applications (10). Within 6 months of Röntgen's discovery, scientists in the USA and Canada had used X-rays to produce medical radiographs (11), and it wasn't long before the biological effects of exposure to X-rays were noticed. Both patients who had been radiographed, and the equipment technicians who operated the equipment began to develop skin inflammation on exposed parts of their bodies (10). Although not much was understood about these biological effects at the time, immediately people began to investigate the

potential therapeutic applications of X-rays. Less than 60 days after Röntgen's discovery of X-rays, Emil Grubbe used them to treat a ulcerated breast cancer in January of 1896 in Chicago USA, giving birth to the field of clinical radiotherapy (12). The biological effects of gamma rays from radioactive substances, and their potential therapeutic uses were also discovered early on. Becquerel himself developed a burn underneath his waist coat pocket in which he carried a vial of pure radium, which was one of the first well documented biological effects from radioactivity (6, 13). Pierre Curie subsequently became interested in the potential medical applications of radioactive substances. Pierre was a pioneer of research on the subject, conducting some experiments on his own arm, as well as providing radium to a hospital in Paris for the first radium therapies (13).

Initially the methods for quantifying the amount of radiation dose delivered were approximate at best. Early X-ray technologies were non-standardized and primitive making them difficult to control, and there were initially no established metrics for measuring exposure quantitatively. This combined with the fact that very little was known about how X-rays interacted with matter made it very difficult to determine the overall efficacy of radiotherapy treatments, or their associated dangers. It was however recognized early on that quantifying the amount of radiation exposure to a patient or technician was important, and so the field of radiation dosimetry was born. In 1925, the international commission on radiological units (ICRU) was established to provide an international standard for the measurement of the ionizing radiation from both X-rays and radioactivity (10). A reliable and reproducible unit to quantify X-ray exposure was established in 1928, and named the 'Röntgen' in honour of the man who discovered them. This unit was also adopted for the measurement of gamma rays in 1937 (14). The ability to accurately measure radiation dose using an internationally accepted standard was a

critical step towards developing safe and effective radiotherapy treatments through scientific research and clinical trials.

Clinical research in radiotherapy required collaboration between many different disciplines including radiology, biology, physics, oncology and more. The early 1900s saw the development of many fundamental concepts and practices which would shape the future of radiotherapy. It quickly became apparent that the way in which you delivered radiation had an enormous effect on the patient outcome. Antoine Béclère pioneered the use of multiple radiation fields to treat a 16-year-old acromegaly patient in 1909 (15). This technique is still in use today, as it delivers radiation to the tumour from multiple angles thereby reducing healthy tissue dose and skin irritation. In the 1920s, concepts such as depth dose and isodose diagrams emerged, which were essential in establishing a firm scientific basis for clinical radiotherapy (16). There was also much to be learned about how living tissue reacted to radiation exposure, and radiobiology emerged as one of the most important areas of research for radiotherapy. The concept of delivering radiation in multiple smaller doses rather than a single large dose was used as early as 1900 by Thor Stenbeck to cure a skin cancer patient (5, 17). This practice would not be rigorously investigated or adopted till the 1920s. In 1928 French scientist Claude Regaud and his team found that skin reactions on the scrotum when sterilizing ram testis could be drastically reduced when radiation was delivered in multiple small doses, as opposed to a single large dose (5). His research demonstrated the difference in response between different healthy tissue (skin) and cancerous tissue (represented by the self-regenerating testis), and would serve as the scientific basis for fractionated radiotherapy (another fundamental practice which remains in use to this day) (5). This work led fellow French scientists Henri Coutard and Francois Baclesse to breakthroughs in understanding the relationships between dose, time, volume, and their effect on

tissue response (5, 18). The critical concept of radiosensitivity, and the factors which determined it such as cell-type and oxygenation were also developed during this period (5).

This research in the early days of radiotherapy greatly improved the quality of care available to cancer patients, and established the foundation upon which modern radiotherapy would be built. Technological developments in the coming years would enable further refinement of these early concepts, as well as the development of far more sophisticated and effective treatments. Over the course of the 20th century enormous amounts of time and energy have been poured into deepening our understanding of how radiation is produced, and how it interacts with matter. Nuclear physics, radiochemistry, relativity, and quantum mechanics are just a few of the fields that have contributed to research on the many forms of radiation and their applications. This knowledge has allowed us to develop increasingly powerful and complex radiation sources, as well as more advanced imaging devices for use in medicine. The next two sections will highlight some of the most important technological developments in the fields of radiotherapy and diagnostic imaging.

1.1.2 The Evolution of Radiotherapy Sources

In the first half of the 20th century, much of the focus in radiology was on improving the quality and reliability of radiation sources. Early X-ray equipment was primitive by today's standards, and controlling the quantity and quality (energy) of the X-rays was one of the biggest challenges in the early days of radiotherapy. The output of the Crookes tube design used by Röntgen in his experiments depended on the gas pressure inside the tube, which changed over time. Early X-ray tubes were low energy (<150 kV), which meant they could not penetrate very

deeply, and that a significant portion of the radiation dose was deposited at the surface of the patient (14). This meant that their therapeutic usefulness was limited to superficial tumours at short distances, and the high surface dose often resulted in severe skin reactions (5). However in 1913 William Coolidge invented the hot-cathode tube, which accelerated electrons via thermionic emission (14). The development of this technology greatly benefited the field of radiology, allowing for independent control of both the quality and quantity of X-rays produced. This led Coolidge to the development of the 'deep therapy tube' released in 1922, which was capable of 140 kV (14). This invention was the first X-ray tube capable of treating deeper seated tumours (~4-6 cm in soft tissues), and marked the beginning of the 'orthovoltage era' which lasted until the end of World War 2 (5, 19). The early 1930s saw the development of X-ray generators up to 750 kV, although they relied on many high voltage transformers in series making them impractically massive (up to 30 ft long) (14). In 1934 R.J. Van de Graff developed an electrostatic generator at MIT capable of a 7MV accelerating potential, but no compatible X-ray tube was available at the time. This technology would be used to treat the first patient with a 'true' (constant) megavoltage beam in March of 1937 (14). Further development of this experimental technology signaled the advent of the 'megavoltage era', which included the development of more advanced X-ray and electron sources such as betatrons, and linear accelerators (19).

Although it was not fully appreciated initially, the gamma rays from radium have an average energy of ~1.1 MeV, meaning that they are much higher energy and deeply penetrating than early X-rays. This meant that while engineers and physicists spent 50 years trying to create higher energy X-ray tubes for deeper radiotherapy treatments, the very first radioactive element was capable of megavoltage radiotherapy (albeit at a very low dose rate). Radium therapies

resulted in less skin irritation due to their greater depth dose (higher energy), and were generally considered less dangerous and complicated to operate than the high voltage X-ray tubes of the time. By the 1920s many physicists and clinicians understood this advantage, however radium would largely remain limited to brachytherapy prior to 1922 due to its scarcity and cost (14). Within 20 years of its discovery, radium had become the most valuable and rare element on the planet, with a single gram being worth over $100,000 (USD) at its peak (20). By 1930 new sources of radium containing ores in Canada, Africa, and South America had been discovered. These discoveries, along with the development of more efficient separation chemistry began to reduce the cost of radium, making it accessible for use in gamma teletherapy research (20). The 1930s also saw great advancements in nuclear physics which made the synthesis of artificial radionuclides using particle accelerators possible. One such radioisotope, Cobalt-60 was first produced around 1935, but research papers on it were only published in 1945 after the end of the Second World War due to security concerns (high energy physics research was largely focused around the development of the atomic bomb) (14, 19). This radioisotope had a longer half-life and higher specific activity than other radionuclides available at the time, making it a promising candidate for use in (external beam) radiotherapy. The main drawbacks to radium teletherapy: cost, scarcity and low dose rate were no longer issues with Cobalt-60. The clinical Cobalt-60 unit was developed between 1949 and 1951 by Harold E. Johns at the University of Saskatchewan (21), and found widespread use in the United States and Canada. This innovation brought inexpensive megavoltage therapy to the world, since MV therapies had previously been limited to large academic or metropolitan centers (14). Due to its reliability and simplicity it remained the ‘workhorse’ of North American radiotherapy clinics until about 1980. For the same reasons,

Cobalt-60 units are still popular worldwide, although very few are still in clinical operation in North America.

In the early 1980's, the Cobalt-60 unit was overtaken in popularity by the linear accelerator (linac) in North American cancer clinics (14). This device was developed between 1935 and 1945 using technology developed for RADAR radiofrequency (RF) power sources during the war (5). It is interesting and somewhat ironic that many technologies developed for war were so critical to the development of modern radiotherapy, and have been instrumental in the healing millions of people. The first medical linac for radiotherapy was developed and implemented by D.W. Fry et al. at Hammersmith hospital in London UK in 1948 (5, 22). In contrast to the gamma radiation (photons) from cobalt-60 used for therapy, linacs allowed for treatment with either high energy photons *or* electrons. They were also capable of variable dose rates and energies, with a maximum photon energy much higher than that of Cobalt-60 which made them even better for treating deep seated tumours (19). These advantages made linacs more versatile than Cobalt-60 units, but it also made them more complicated and less reliable, which is why linacs remained less popular until the 1980s (14). Other forms of radiation treatment using neutrons and charged ions have been investigated near the end of the 20th century, though megavoltage photons and electrons are still used for the vast majority of radiotherapy treatments to this day, and alternative therapies using other forms of radiation are limited to a relatively small number of specialized cancer centers.

Improved radiation sources, clinical practices, and standardized measurements protocols have vastly improved the efficacy of radiation treatments. However the usefulness of these improvements would be limited if not for critical innovations in the fields of diagnostic imaging and computer technology. Being able to produce precise quantities and qualities of ionizing

radiation would not be medically useful without the ability to also precisely localize the delivery of that radiation. While the first half of the 20th century saw the greatest advances in the production of radiation, the second half would see incredible advances in the field of diagnostic imaging that would have been hard for Röntgen to imagine when he produced the first radiograph. The next section will focus on developments in the field of diagnostic imaging, and how they have shaped modern radiotherapy and treatment planning.

1.1.3 Diagnostic imaging and the Advent of Modern Treatment Planning

In the early days of radiotherapy, to estimate the position of a patient's organs oncologists relied on tomographic atlases, literally books filled with pictures of a person who had been cut up into slices. Today, nearly every radiotherapy patient's treatment is planned on a three dimensional scan of their body, tailoring the treatment to their unique anatomy. The transition from basic projection radiography to three dimensional imaging techniques took almost 80 years of rigorous research and progress in the fields of radiology, mathematics, and computer technology. Although projection radiography was immediately adopted by scientists and medical practitioners around the world upon its discovery, the limitations of projected two dimensional images quickly became apparent (3). Resolving structures which overlapped in the projected images was a significant challenge for radiologists and engineers, who would propose a myriad of different approaches to solve this problem. Less than a year after X-rays were discovered, E. Thompson attempted to produce X-ray images with depth perspective by taking two offset radiographs and viewing them through a stereoscope (3). By 1915, radiologists started to experiment with movement of the radiation source, film, and object being imaged. This process

could blur unwanted shadows from overlapping structures in the three dimensional volume, producing an image where the only unblurred shadows were from structures contained in a two dimensional imaging plane within the object and parallel to the film. Variations of this practice would be 'discovered' independently by at least eight different investigators in four separate countries, and patented five times by 1929 (23). It would receive an assortment of different names including 'body section radiography', 'tomography', 'stratigraphy', 'planigraphy', and 'laminography', until finally in 1962 the ICRU appointed a five member committee which settled on the name 'tomography' (23). This analog process using film to produce the sectional image is now known as 'conventional tomography'.

True three dimensional imaging would be based on many of the principles of conventional radiography, but would require innovation from other fields in order to become a reality. The field of mathematics would establish the theoretical basis for reconstructing a three dimensional object from a series of two dimensional projections. The 'Radon transform' was invented in 1917 by Austrian Mathematician Johann Radon, which established that a function could be reproduced from an infinite set of its projections (24). In 1937 Polish mathematician Stefan Kaczmarz would publish a paper detailing his method for finding an approximate solution to a system of linear equations (25). Although these two developments provided the theoretical basis for three dimensional image reconstruction, the time for a human to perform the required calculations made it prohibitively impractical for clinical use. What was required was a calculating machine which could speed up the process, the device which permeates every aspect of our lives today: the computer. Alan Turing, who is widely considered the father of modern computer science, was the first to envision such a device which he described in a publication in 1937 (26) . He theorized that it was possible to construct an analytical thought process through a

finite series of simple instructions which could then be executed by a machine. The first real computer would be yet another fruit borne of activity during World War 2 which would have far reaching benefits outside of warfare. “Colossus I’, the world’s first computer was designed by Turing while working for the British Military to crack the ‘unbreakable’ Enigma code used by the German army to encrypt their transmissions. His device changed the course of the war, and was a closely kept secret until 1976 when the project was finally declassified (3). Early computers were massive, complicated and unreliable, and it would take significant advances in engineering such as the invention of the transistor in 1948, and the integrated circuit in 1969 before they would become more dependable and compact (3). Now with both the mathematical theory for tomographic image reconstruction, and computers capable of rapidly performing the computations, the stage was set for the next stage of evolution in diagnostic imaging.

In 1956 South African physicist Allan Cormack began to work on X-ray image reconstruction at Harvard University (3). By 1963 he had solved the problem theoretically, and validated his work experimentally, publishing his results in the Journal of Applied Physics (3, 27). Being a theoretical physicist, Cormack was more interested in the problem itself than it’s applications to medicine. English engineer Godfrey Hounsfield would be the one to develop the first clinical computed tomography scanner at EMI Central Research Laboratories (3). Beginning his work in 1967, Hounsfield’s initial apparatus used a low output Americium gamma ray source which required long exposures of up to nine days in order to accumulate the information required for the image reconstruction (3). The required data consisted of around 28 thousand measurements, and it took the computer about two and a half hours to perform the reconstruction (3). This process produced a 80x80 pixel image with enough contrast to visualize differences in brain tissues in the imaged slice. Hounsfield would patent his device in 1968, and by 1971 he

had developed the EMI Mark I scanner which would be installed at Atkinson Morley Hospital in Wimbledon England (3, 28). The Mark I could produce the same resolution image significantly faster with a scan time of under 5 minutes and a 20 second reconstruction time. This speed increase was a result of another contribution from mathematicians, the algebraic reconstruction technique (ART) developed a year earlier at New York state University (29). This made the CT scanner much more practical for clinical use, and in October of 1971 the first clinical patient was scanned using the device (3). By the end of 1973 the first commercial CT scanner was released, the EMI CT 1000. Even more advanced than its predecessor, the CT 1000 scanner was capable of acquiring a 320x320 pixel image in just 20 seconds (3). The invention of the computed tomography scanner represents another milestone in the evolution of radiotherapy (and diagnostic imaging) rivaled in significance perhaps only by the discovery of X-rays themselves at the turn of the century. The CT scanner would re-revolutionize medicine, laying the foundation for the development of three dimensional imaging techniques which would be essential to the development modern radiotherapy. For their contributions to the development of computer assisted tomography, Hounsfield and Cormack would share the Nobel Prize in Medicine in 1979, and would be the first non-medically trained researchers ever to be honoured with the award (30).

The invention of the clinical CT scanner would spur an avalanche of technological development in diagnostic imaging, as companies around the world raced to capture as much of this new market as possible. Soon CT scanners could image several adjacent slices in order to reconstruct a truly three dimensional volume. This prompted the creation of 3D treatment planning systems (TPS) for radiotherapy treatments which made use of the radiological information provided by the CT scanner to provide patient specific dose calculations. Since CT

scanners produce images by detecting how much radiation is absorbed in the body, they naturally provide the electron density information needed for radiotherapy dose calculations. Today CT scanners are used in virtually every modern cancer hospital as the starting point for radiotherapy treatments. The technology and theoretical basis for the CT scanner was also adapted to other 3D imaging techniques such as the PET/SPECT scanner which detects radiation from injected radionuclides, and magnetic resonance imaging (MRI) which detects the magnetic response of molecules inside the body. Together these technologies have revolutionized medicine, ushering in diagnostic tools of such power and precision that they had previously only been imagined in science fiction. It is around this time in history that we start to see the inherent synergy and interdependence between diagnostic imaging and radiotherapy. The increasingly precise knowledge of the tumour size, shape and location provided by new imaging modalities would lead to the development of many more advanced treatment techniques, and usher in the era of modern radiotherapy.

1.2 Modern Radiotherapy and IGRT

The modern practice of frequently imaging a patient during a course of external beam radiation therapy in order to guide decision making is known as image guided radiotherapy (IGRT). One of the main goals of IGRT is to deliver a lethal dose of radiation to malignant tissues, while sparing healthy tissue as much as possible. This combination provides the highest tumour control probability (TCP) with the lowest probability of normal tissue complications (NTCP) (31). With the invention of the CT scanner, clinicians had a powerful new tool to facilitate this goal, and for the first time could localize many tumours with relative accuracy. Armed with this information, radiation could be delivered from multiple angles with shapes conformed to the target in order to achieve greater sparing of normal tissues without sacrificing

tumour coverage. This technique was dubbed 3D conformal therapy, and found widespread use in the 1980s after the introduction of clinical CT scanners and 3D TPSs (31). The beam shaping for 3D-CRT was originally done by using custom molded blocks, which would be changed by hand for each beam angle. However a more advanced beam shaping device which used electronically controlled mechanical leaves would soon take the place of molded blocks: the multi-leaf collimator (MLC). This device was actually first developed prior to the invention of the CT scanner (32, 33), however its true potential would be unlocked by modern imaging techniques and computer technologies. The implementation of digitally controlled MLCs would lead to the development of intensity modulated radiotherapy (IMRT) in the late 1980s (34, 35). Unlike 3D-CRT which delivers uniform fluence within each field shape, intensity modulated radiotherapy is capable of delivering non-uniform fluences to a target from each beam angle. IMRT is able to deliver more precise dose distributions to the target volume and even escalate dose to more aggressive tumour cells, while further reducing the dose to healthy tissue (compared to 3D-CRT) (35). A computer algorithm can be used to determine the non-uniform fluences for an optimized the dose distribution in the TPS to attain clinical and dosimetric objectives, and this process is known as *inverse-planning*. This is in contrast to conventional forward-planning, where the planner defines beam shapes conformed to the target first, and then calculates the dose delivered (repeating this process until an acceptable dose distribution is achieved).

Progress in imaging and computer technology has made the development of sophisticated techniques such as 3D-CRT and IMRT possible, which have greatly improved the quality of care provided to cancer patients. The effectiveness of a radiotherapy treatment is dependent on the ability to accurately localize and deliver radiation dose to the tumour, which is primarily limited

by two factors. The first factor is the ability of the radiation oncologist to accurately delineate the tumour from healthy tissues, which is largely dependent on the quality of images at his disposal. Unfortunately all radiography based imaging techniques share a common weakness. Since most tissue is more or less equivalent to water radiologically, these techniques do not have good soft tissue contrast. This means that X-ray imaging devices can tell the difference between bone and tissue quite well, but have trouble differentiating different types of soft tissue such as organs and tumours. Furthermore, the X-rays attenuated inside the patient which allow images to be produced deposit some radiation dose. Although radiation can be used effectively to treat cancer, the damage it causes also increases the risk of developing cancer. It is therefore important to reduce the amount of radiation anyone receives by as much as possible. There are however several modern imaging techniques that do not rely on attenuation of X-rays to produce images. Of particular importance to this research are magnetic resonance imaging (MRI) techniques. MRI scanners produce their images by measuring the magnetic response and relaxation of the molecules in a patient's body once they have been excited out of equilibrium. This type of imaging is much more versatile, because many different types of information can be extracted depending on the selected imaging technique (36). MRI generally has vastly superior soft tissue contrast compared to other imaging modalities, and can also yield information on blood flow, chemical composition, brain activity and more. Although in some cases it cannot be used for patients with metallic implants and prostheses, it is generally considered safer than X-ray based techniques since it does not produce ionizing radiation. It has become commonplace to use complementary imaging devices (such as CT and MRI) for radiotherapy treatment planning.

The second main factor which affects the accurate delivery of radiation is uncertainty in patient position with respect to the radiation beam(s) which occurs over the course of treatment

either during (intrafractional), or between fractions (interfractional). Intrafractional uncertainties are usually due to patient movement over a short time, or anatomical changes resulting from bowel movements, swallowing, or heart and lung motion during treatment. Interfractional uncertainties are a result of either anatomical changes between treatments (e.g. weight loss and/or tumour shrinkage), or difficulties reproducing of the patient setup on the treatment couch. The ICRU has issued two reports which provide guidelines for defining target volumes and margins to account for these positional uncertainties (37, 38). Figure 1.2 below shows the relationships between these concentric target volumes. The gross tumour volume (GTV) is defined as "the gross demonstrable extent and location of the malignant growth", and is determined by either diagnostic imaging or clinical examination (37). The GTV is then enlarged to account for any "microscopic spread of tumour cells that are not detectable in the planning images", and this new structure is called the clinical target volume (CTV) (37, 39). Finally the planning target volume (PTV) is created by adding two more margins to the CTV: the internal margin (IM) which accounts for intrafractional uncertainties; and the setup margin (SM) which accounts for interfractional uncertainties (37, 38).

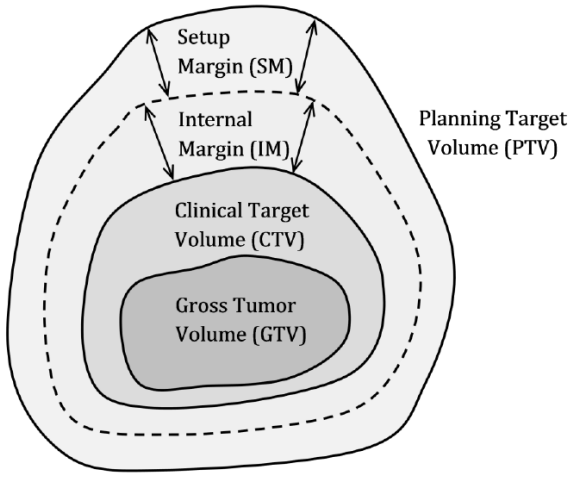

Figure 1.2 ICRU 50 and ICRU 62 margins for radiation therapy (39)

These margins have been established in order to ensure that no tumour cells are missed by the radiation, which could result in failure of local control or future disease recurrence. However the associated cost is that a significant amount of healthy tissue is also irradiated, which increases the likelihood of undesired complications. Therefore much of the focus of IGRT research and development is on minimizing the size of the IM and SM by reducing their associated positional uncertainties. In-room lasers and computer controlled treatment couches help facilitate accurate reproduction of the patient setup, and hence a reduction of interfractional uncertainties. The use of standardized coordinate systems between imaging and treatment modalities can also be useful, and CT simulators which have the same treatment couches and coordinate systems as the linacs are typically used in order to better match the patient positioning between imaging and treatment (40). As imaging technology improved and became smaller, it was possible to image more frequently (before, after and even during fractions) in order to guide treatment decision making and delivery. It is now standard for linacs to be equipped with KV radiographic imaging along with cone-beam (CBCT) and electronic portal imaging devices (EPIDs). Patients are imaged before each fraction, and this image set is registered with the set on which the treatment was planned, allowing for corrective shifts or rotations to be applied to the treatment couch. Radiation therapists also make frequent use of immobilization devices in order to reproduce the patient setup during treatment. These practices can significantly reduce the interfractional setup error associated with radiotherapy treatments, and hence contribute to reducing the size of the SM. In order to reduce intrafractional uncertainties and the IM, clinicians have developed techniques for predicting organ motion (41-43). Although IGRT using imaging before and after treatment has proven very effective, the ability to image *during* treatment in

order to track organ and/or tumour motion and guide radiation delivery in real time would provide even greater reduction of intrafractional uncertainty.

1.3 The Next generation of IGRT: Real-time Imaging and Linac-MR Systems

Several methods have been proposed for real time imaging which make use of external or surgically implanted markers in or close to the tumour which follow its motion during treatment using radiographic (X-ray fluoroscopy), electromagnetic (radio-frequency transponders), or optical (infrared reflectors) tracking (44-47). However these techniques track the surrogate marker instead of the tumour itself: the main limitations of these real-time imaging techniques are that the surrogate motion is not always correlated with tumour motion, and changes in the tumour shape are not accounted for. Ultrasound imaging is a non-invasive technique capable of providing volumetric information that is being investigated for real time IGRT (48, 49). However the usefulness of ultrasound is limited by its relatively poor image quality and it cannot be used effectively in regions which contain large density changes such as bone or gas cavities.

One of the most promising areas of research in the next generation of IGRT technologies is the work being done on integrating MRI scanners with clinical treatment units for on-board imaging. As previously mentioned, MRI scanners have superior soft tissue contrast and versatility in available imaging techniques compared to current KV CBCT. They are also capable of rapidly acquiring volumetric image sets without any need for the mechanical rotation inherent to CT scanners, which makes them more suitable for real time imaging. These factors combined with the fact that MRI scanners do not use ionizing radiation make them a promising new tool for real-time imaging. There are however significant mechanical and physical challenges which

must be overcome in the development of this new hybrid technology, and there is no single answer to the question of how to most effectively integrate the MRI scanner into a clinical radiotherapy treatment unit. There are currently five research groups worldwide investigating this exciting new technology, each of which has developed a unique design and approach to its associated challenges (50-54). These groups include researchers in Australia (52), Canada (50, 51), the Netherlands (53), and the United States (54).

Our research group at the Cross Cancer Institute in Edmonton, Alberta, Canada has developed a prototype system using a 6MV linac and a 0.56T magnet MRI that is capable of two different configurations. The rotating bi-planar (RBP) system rotates around the patient such that the main magnetic field of the MRI is always perpendicular to the superior-inferior axis of the patient. The linac can be mounted in either: 1) the perpendicular configuration, where the central beam axis is perpendicular to the main magnetic field of the MRI; or, 2) the parallel configuration, where the central beam axis is parallel to the main magnetic field of the MRI (Figure 1.3). In both cases, the entire assembly of the linac and MRI rotates together such that the relative orientation of the linac and magnetic field remains constant for all gantry angles. In the development of our working prototype, many challenges were addressed, including image distortion, radiation induced current, magnetic shielding, magnet design and perturbed dosimetry (50). The details of the research and development of our prototype can be found in over 35 peer reviewed publications available for viewing at http://linacmr.ca/publications.html.

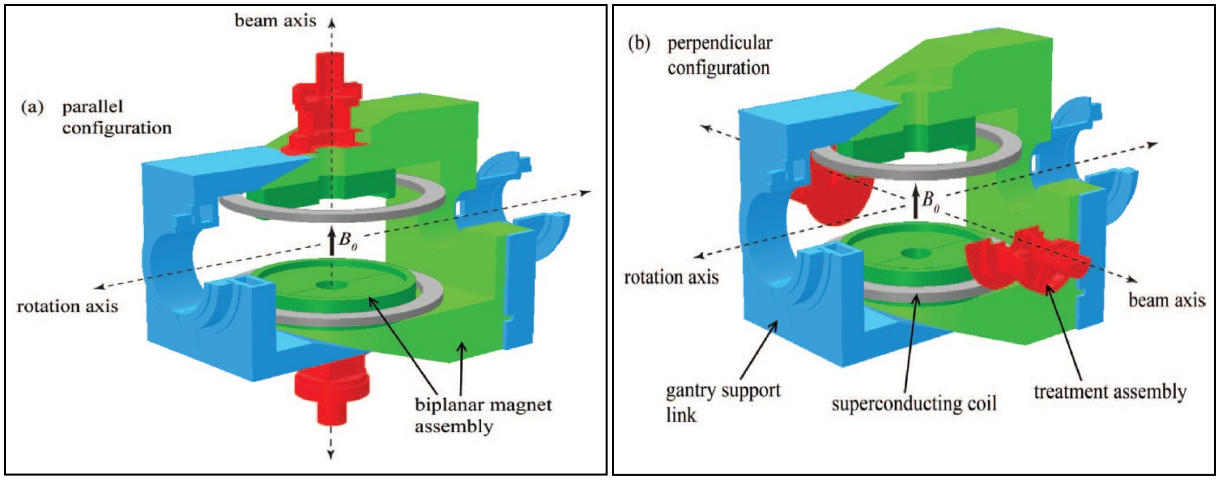

Figure 1.3 CCI Linac-MR prototype configurations: a) is the parallel configuration where the linac is mounted parallel to the main magnetic field of the MRI; b) is the perpendicular configuration where the linac is mounted perpendicular to the main magnetic field of the MRI (55)

1.4 Research Motivation : Linac-MR Dosimetry for Inverse-planning in Lung

Linac-MR systems have the potential to be the most advanced and effective form of IGRT to date, facilitating significant reductions of IM and SM (and hence normal tissue irradiation and complication). However with the reduction of these margins the accuracy of radiation delivery becomes even more critical. The main magnetic field of the MRI scanner significantly alters the dose deposition due to the Lorentz force it exerts on moving charged particles such as secondary electrons, particularly in low density regions such as lung where their mean free path is longer. The resulting dosimetric effects are different depending on the direction of particle travel relative to the magnetic field of each Linac-MR configuration, and have been investigated thoroughly by our research group and others (56-61). For the perpendicular configuration, the magnetic field causes electrons to be curved away from the beam axis which can result in a lateral shift in dose distribution, decrease in skin dose, change in depth dose, and

the electron return effect (ERE), which increases exit dose at tissue-air interfaces (56, 58, 61, 62). For the parallel configuration, the magnetic field actually confines scattered electrons to constant gyroradii, preventing them from scattering out of the beam. This confinement has several effects including a reduction of penumbral width, an increase in skin and PTV dose, and hotter (colder) dose distributions inside (outside) the beam edges, particularly at higher magnetic field strengths and in areas traversing low density regions such as lung (57, 59, 63). The impact of these dosimetric effects on treatment plan optimization through inverse-planning has been investigated by the Lagendyk et al. (Utrecht University, Netherlands), who found that the magnetic field did not have a clinically significant effect on their optimized treatment plans (64). However, their study only investigated the effects on their perpendicular configuration prototype, and did not include a study in lung where the magnetic field would have the largest effect.

This thesis aims to address the gap in current research regarding the dosimetric implications of inverse-planning on a Linac-MR system in lung, for both the parallel and perpendicular configurations. My goal is to answer the question of whether the magnetic field of a Linac-MR system is important to model for inverse-planning of a lung patient. To achieve this goal, I will be investigating the following three cases:

Case #1) the magnetic field is not modeled at any stage of the treatment planning process;
Case #2) the magnetic field is modeled during forward calculation only;
Case #3) the magnetic field is modeled during both optimization and forward calculation.

By comparing these three cases, I will determine the importance of modeling the magnetic field during these stages of the inverse-planning process. Dose calculation in the presence of magnetic fields is computationally time intensive. If it were possible to ignore the magnetic field during

either optimization or forward calculation (or both), then it would significantly reduce the time and complexity of the treatment planning process for a lung patient on a Linac-MR system.

Here is a short roadmap of the chapters to come. Chapter 2 will cover the background and theory relevant to this project, including: basic particle interactions; Lorentz forces and their effect on dose deposition; dose calculation (collapsed cone convolution and Monte Carlo calculation); treatment planning (basic forward planning, inverse-planning, and plan quality evaluation). Chapter 3 will outline the methodology used for this research including: patient and treatment plan selection; establishment of a calculation framework; inverse-planning algorithm and objectives; metrics used for treatment plan comparison. Chapter 4 will present the results of my research, including: validation of the calculation framework; the impact of magnetic fields and tissue heterogeneities on unmodulated treatment plans; the impact of magnetic fields on optimized fluences; the impact of magnetic fields on optimized dose distributions. Finally, Chapter 5 will summarize the conclusions of my research, their implications, and areas of future work.

Chapter 2: Background & Theory

This chapter presents the theoretical background for this research project. Section 2.1 describes how radiation interacts with matter within the context of radiotherapy. This includes photon interactions, the generation of the secondary electrons that subsequently deposit energy (dose) inside a patient, and the Lorentz force on charged particles moving in a magnetic field. Section 2.2 will cover the effect of the Lorentz force on dose deposition for the two Linac-MR configurations to be studied (parallel and perpendicular). Finally Section 2.3 will deal with treatment planning systems including: the treatment planning process; forward and inverse-planning; dose calculation; treatment plan evaluation and comparison metrics; associated parameters and coordinate systems.

2.1 Interaction of Ionizing Radiation with Matter

Electromagnetic (EM) radiation is the transport of energy through massless particles called photons, which are essentially oscillating electric and magnetic fields. The energy of the radiation is proportional to its frequency, and inversely proportional to its wavelength:

$$E = h\upsilon = h\frac{c}{\lambda}$$ Photon Energy Equation 1

Where: E is the photon energy [J]

ν is the photon frequency [s^{-1}]

λ is the photon wavelength [m]

c is the speed of light [$m \cdot s^{-1}$]

h is Planck's constant [J·s]

EM radiation is classified according to specific energy ranges, which include (from lowest to highest energy): radio/micro waves, infrared/visible/ultraviolet light, X-rays and gamma rays. As described in the previous chapter, X-rays and gamma rays are named based on how they are produced, not because one is inherently higher energy than the other. Both sit at the top of the EM energy spectrum, and are part of a class known as ionizing radiation. As the name suggests, this type of radiation has enough energy to strip electrons from atoms, thereby ionizing them. There are two types of ionizing radiation. Directly ionizing radiation consists of charged particles such as electrons, protons, alpha particles, and other heavy ions. Directly ionizing radiation deposits energy through Coulomb interactions with the atoms and orbital electrons of the medium it traverses. Indirectly ionizing radiations are uncharged particles (photons and neutrons) that produce directly ionizing charged particles within the medium, which then go on to deposit energy. As previously mentioned, photons or electrons are the ionizing radiation used in the majority of modern radiotherapy treatments. I will therefore describe the process of dose deposition through primary photon interactions, and how they generate secondary particles which then deposit energy within a patient.

2.1.1 Photon Interactions

There are four main processes through which photons can interact with a medium: Rayleigh (coherent) scattering; the photo-electric effect; Compton (incoherent) scattering; and pair/triplet production. A brief description of these processes is given below, and the latter three, which involve energy transfer to charged particles, are depicted in Figure 2.1.

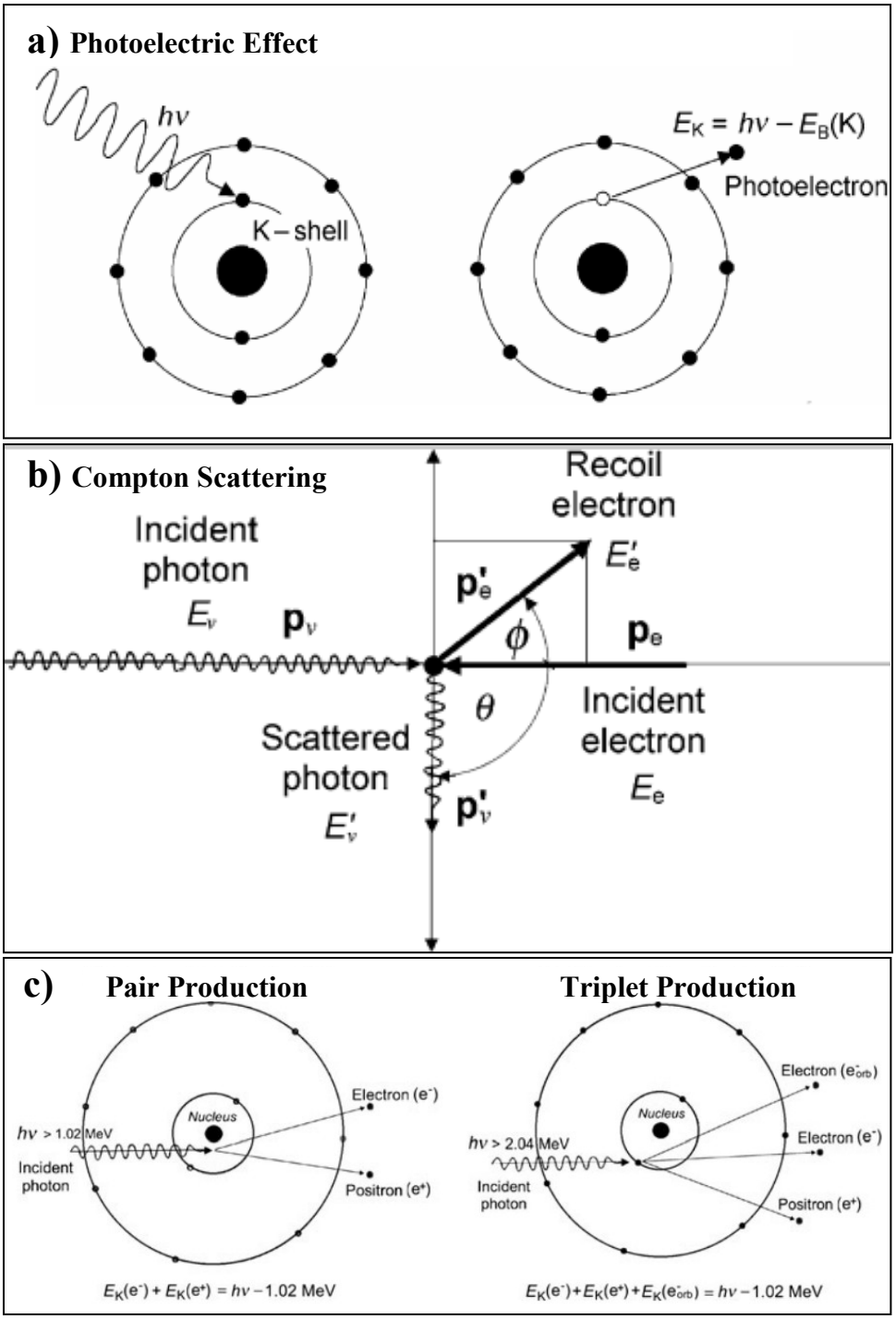

Figure 2.1 Three main processes by which photons transfer energy in a medium. a) Photo-electric effect ; b) Compton Scattering ; c) Pair/Triplet production (65)

- ***Rayleigh scattering***: an incoming photon interacts with an orbital electron, producing a scattered photon with the same energy as the incident photon but a different direction. This process does not deposit energy in the medium, and the probability of this type of interaction is negligible for energies greater than 100keV.
- ***Photo-electric effect***: an incoming photon interacts with a tightly bound orbital electron, where the energy of the photon is greater than or equal to the binding energy of the electron. The photon is absorbed, and the photo-electron is ejected with a kinetic energy equal to that of the photon minus the binding energy. The likelihood of this process occurring is highest when the energy of the incident photon just exceeds the binding energy of the electron.

$$E_K = h\nu - E_B$$ Photo-electric effect Equation 2

Where: h is Plancks constant [J·s] E_K is the kinetic energy of the photo-electron [J]
ν is the photon frequency [s^{-1}] E_B is the binding energy of the orbital electron [J]

- ***Compton Scattering***: an incoming photon interacts with an orbital electron whose binding energy is much less than the photon energy. The photon loses a portion of its energy to the 'recoil electron' which is ejected from the atom at angle ϕ, and the photon is scattered through angle θ from its original direction. The energies of the scattered photon and the recoil electron are related through conservation of energy and momentum by the following equations:

$$E_v + E_e = E_v{}' + E_e{}'$$ Compton Conservation of Energy Equation 3a

$$\lambda' - \lambda = \frac{h}{m_e c}(1 - \cos\theta)$$ Compton Scattering Equation 3b

Where: E_γ is the incident photon energy [J]
E_e is initial electron energy [J]
$E_v{}'$ is the scattered photon energy [J]
$E_e{}'$ is the scattered electron energy [J]
λ is the incident photon wavelength [m^{-1}]
λ' is the scattered photon wavelength [m^{-1}]
h is Planck's constant [J·s]
m_e is the electron mass [kg]
c is the speed of light [$m \cdot s^{-1}$]
θ is the photon scattering angle [radians]

- ***Pair production***: an incoming photon interacts with the nuclear Coulomb field, disappears and is replaced by an electron-positron pair. The minimum photon energy required for this interaction is the rest mass energy of the electron-positron pair of $2m_ec^2$=1.02 MeV. **Triplet production** is when this process occurs in the field of an orbital electron which is ejected from the atom and shares the energy of the incident photon with the electron-positron pair. The energy threshold for triplet production is $4m_ec^2$=2.04MeV.

$$E_K(e^+) + E_K(e^-) = h\nu - 1.02MeV \quad \text{Pair Production} \quad \text{Equation 4a}$$

$$E_K(e^+) + E_K(e^-) + E_K(e^-_{orb}) = h\nu - 1.02MeV \quad \text{Triplet Production} \quad \text{Equation 4b}$$

Where: h is Planck's constant [MeV·s]
ν is the incident photon frequency [s^{-1}]
E_K is the energy of the positron (e^+) or electron (e^-) [MeV]

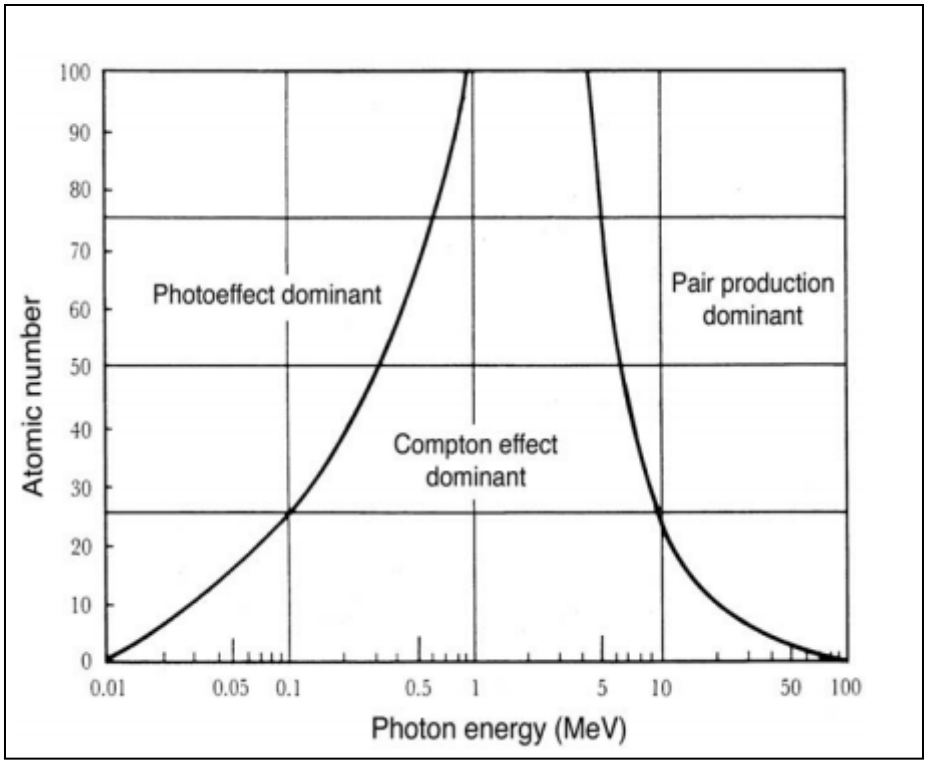

Figure 2.2 Photon interaction coefficient regions of dominance. The curves separating each region are where the probabilities are equal for those two interaction types. Energy (x) axis is on a logarithmic scale. (66)

In general, the photoelectric effect is dominant at low energies, Compton scattering dominates at intermediate energies, and pair/triplet production dominates at high energies (Figure 2.2). Since most of the human body is close to water radiologically (low effective atomic number $Z_{eff} \approx 8$), Compton scattering dominates for radiotherapy treatments where all or most photon energies are below 10 MeV. At these energies, the vacancies in the atomic shells created by the photoelectric effect, Compton scattering and triplet production mostly occur in the inner energy levels. These vacancies are filled by electrons in higher shells, which results in the release of energy through characteristic X-rays or Auger electrons. Auger electrons are outer shell electrons which are ejected by the release of energy from the orbital transition, and their kinetic energy is equal to that of the transition minus their binding energy. The electrons ejected from

atoms are known as secondary electrons, and go on to deposit energy elsewhere in the patient. The positrons from pair and triplet production almost immediately encounter a free electron with which they annihilate, producing two 0.511 MeV photons which are emitted in opposite directions. These annihilation photons and the characteristic X-rays from orbital transitions continue on and undergo more interactions within the medium.

Radiation interaction is statistical in nature, and each interaction process has an associated interaction coefficient that signifies the probability the process will occur for a given photon energy hν and atomic number Z of the medium. The total interaction coefficient μ is the sum of the coefficients from all four of these processes. When a monoenergetic narrow photon beam travels through a medium, it undergoes exponential attenuation due to photon interactions which absorb or scatter photons from the beam. Equation 5 describes this process for a homogeneous medium, and is often used in basic radiography theory since X-ray images are produced by measuring the intensity of photons that make it through a patient.

$$I(x) = I(0)e^{-\mu(h\nu,Z)x}$$ Exponential Attenuation Equation 5

Where: I is the intensity of the beam [arbitrary unit]

x is the distance through the attenuator [cm]

μ is the total interaction coefficient [cm^{-1}]

A more useful quantity for dosimetry than intensity is the fluence of particles, which is used to quantify the density of particles traversing a particular location, e.g photons or electrons in a medium. It is defined as the number of particles dN passing through a sphere of cross-sectional area dA, and is typically expressed in units of [cm^{-2}] :

$$\Phi = \frac{dN}{dA}$$ Fluence Equation 6

A closely related quantity is the energy fluence of the primary photons in units of [J · m^{-2}] :

$$\Psi = \Phi_p E$$ Energy Fluence Equation 7

Where: E is the energy of the mono-energetic photons [J]
Φ_p is the fluence of photons [m^{-2}]

The photon energy fluence can be used with the mass attenuation coefficient $\frac{\mu}{\rho}$ to calculate the TERMA. TERMA is the total energy released per unit mass through primary photon interactions by a radiation field interacting with a medium of density ρ at point $\vec{r}$:

$$T(\vec{r}) = \frac{\mu}{\rho}(\vec{r})\Psi(\vec{r})$$ TERMA Equation 8

Where: $\frac{\mu}{\rho}(\vec{r})$ is the mass attenuation coefficient at point $\vec{r}$ [m^2 · kg^{-1}]
$\Psi(\vec{r})$ is the energy fluence at point $\vec{r}$ [J · m^{-2}]
T$(\vec{r})$ is the TERMA at point $\vec{r}$ [J · kg^{-1}]

As mentioned earlier, the energy released through primary photon interactions (TERMA) is not all deposited locally, much of it is transported from the interaction point through secondary electrons, scattered photons, bremsstrahlung photons, and characteristic X-rays. The subsequent spread of this energy is most commonly described through the use of dose kernels, which will be described in Section 2.3.

2.1.2 Electron Interactions and Dose Deposition

Electrons traversing matter undergo Coulomb interactions with atomic nuclei and orbital electrons, which can be either elastic or inelastic. Elastic collisions change the direction of the incident electron but do not result in any loss of energy (analogous to coherent scattering for photons). Inelastic collisions also scatter the incident electron, but do deposit energy in the medium through either collisional or radiative losses.

From a classical approach to Coulomb scattering, the likelihood that an interaction results in a large or small transfer of energy is related to the proximity of approach of the traversing electron to the atom. The impact parameter 'b' is defined as the perpendicular distance from the center of the atom to the initial path of the electron (Figure 2.3).

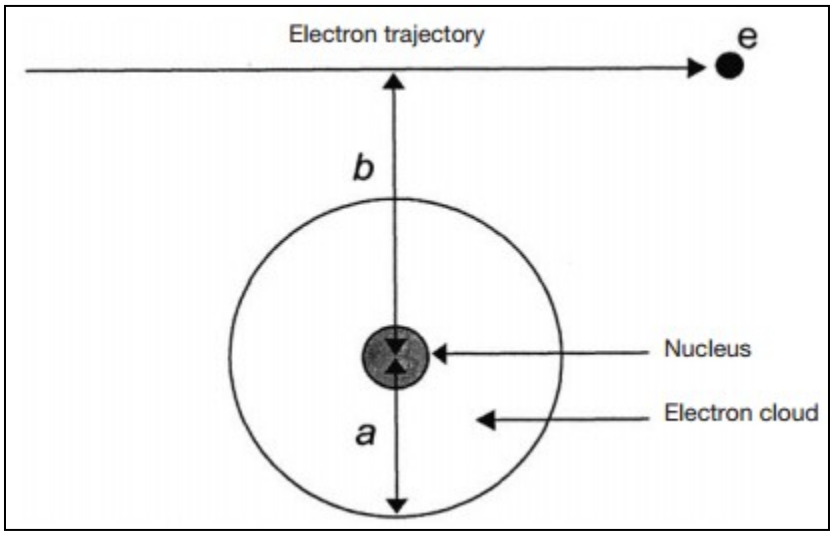

Figure 2.3 Electron interaction with an atom: the probability of interaction depends on the impact parameter b and the atomic radius a. (66)

When the impact parameter is much greater than the atomic radius 'a', the electron undergoes a 'soft collision' in which only a small amount of energy is transferred to the orbital electrons of

the atoms. When a≈b the incident electron undergoes a 'hard collision' with an orbital electron, resulting in the transfer of a significant amount of its kinetic energy. These type of collisional energy losses result in either ionization or excitation of the orbital electron. When an ionized electron has sufficient energy that it can ionize further electrons in the medium through subsequent interactions, they are called delta rays. The last type of interaction is when b is much less than the atomic radius, in which case the incident electron interacts with the atomic nucleus. This results in a radiative loss of energy through the production of bremsstrahlung (braking radiation), the second main process by which X-rays are produced (the other being characteristic X-rays). In this case the smaller the impact parameter, the higher the energy of the bremsstrahlung photon. The amount of energy lost per unit length per unit density by an electron traversing matter is described by the mass stopping power, which has both radiative and collisional components:

$$\left(S/\rho\right)_{tot} = \left(S/\rho\right)_{col} + \left(S/\rho\right)_{rad} \quad [\text{MeV}\cdot\text{cm}^2\cdot\text{g}^{-1}] \qquad \text{Mass Stopping Power} \qquad \text{Equation 9}$$

The mass stopping power is a function of the energy of the incident electrons, and the type of material they are traversing (i.e. density and atomic structure). The average distance between particle interactions for both photons and electrons is known as the 'mean free path'. Since they are massless and chargeless, the mean free path for photons is much longer than for electrons. Therefore radiative losses of energy by an electron produce photons which do not deposit energy locally, but continue on to undergo further photon interactions (much like the scattered photons and characteristic X-rays from Section 2.1.1). The energy lost through collisional interactions however is deposited locally over a short range of a few centimeters. Therefore the collisional component of the mass-energy stopping power is an important quantity

for radiation dosimetry, where the dose (energy per unit mass) deposited by electrons is given by:

$$D = \Phi_e \left(S/\rho\right)_{col}$$ Electron Dose Equation 10

Where: D is the deposited electron dose [J·kg^{-1}]

Φ_e is the fluence of electrons [m^{-2}]

$\left(S/\rho\right)_{col}$ is the collisional mass-energy stopping power [J·cm^2·kg^{-1}]

The greater the density of the medium, the higher the likelihood of interaction for an electron, and the more energy will be lost per unit length. For Linac-MR systems, dose deposition occurs under the influence of a strong magnetic field. As mentioned briefly in chapter 1, this magnetic field affects the trajectory of charged particles, and hence the energy deposition by secondary electrons in a patient.

2.1.3 Lorentz Forces

When charged particles move under the influence of electric and magnetic fields, they experience a Lorentz force according to Equation 11a below:

$$\vec{F} = q(\vec{E} + \vec{v} \times \vec{B})$$ Lorentz Force [N] Equation 11a

Where: q is the electric charge of the particle [C] $\vec{E}$ is the external electric field [N·C^{-1}]

$\vec{v}$ is the instantaneous velocity of the particle [m·s^{-1}] $\vec{B}$ is the external magnetic field [T]

When there is no external electric field, Equation 11a reduces to:

$$\vec{F} = q\vec{v} \times \vec{B}$$ Lorentz Force for magnetic field only Equation 11b

In this case, a charged particle experiences a force perpendicular to both its direction of travel and that of the applied magnetic field. The magnitude of this force is proportional to its electric charge q, instantaneous velocity $\bar{v}$, and the strength of the magnetic field $\vec{B}$. Since the magnetic Lorentz force always acts perpendicular to a particle's velocity, it does no work. Hence the kinetic energy and speed of the charged particle remain constant, and the Lorentz force will cause circular motion in this perpendicular plane. The velocity vector of a charged particle in a magnetic field can be decomposed into two orthogonal components, one that is parallel, and one that is perpendicular to $\vec{B}$. Since the cross product of two parallel vectors is always zero, the parallel velocity component contributes nothing to the cross product in Equation 11b; the remaining perpendicular component's contribution reduces to the product in Equation 11c.

$$\left|\vec{F}\right| = \left|q(\vec{v}_{\perp} + \vec{v}_{\parallel}) \times \vec{B}\right| = qv_{\perp}B \qquad \text{Equation 11c}$$

Where: $\vec{v}_{\perp}$ is the component of the particles velocity which is perpendicular to $\vec{B}$

$\vec{v}_{\parallel}$ is the component of the particles velocity which is perpendicular to $\vec{B}$

The centripetal force acting on an object moving in circular motion is given by,

$$F_c = \frac{mv^2}{r} \qquad \text{Centripetal Force} \quad [\text{N}] \qquad \text{Equation 12}$$

Where: F_c is the centripetal force on the particle [N] m is the mass of the particle [kg]

v is the instantaneous velocity [$m \cdot s^{-1}$] r is the radius of the circle [m]

Substituting Equation 11c into Equation 12 and solving for r gives the gyroradius of the magnetically induced circular motion:

$$r = \frac{mv_{\perp}}{qB}$$ Gyroradius [m] Equation 13

2.2 The Linac-MR System

As described in chapter 1, the Linac-MR prototype system at the Cross Cancer Institute in Edmonton Alberta Canada is capable of treating in either a parallel or perpendicular configuration (Figure 1.3). Parallel and perpendicular refer to the orientation of the MRI's main magnetic field B_0 relative to the beam central axis (CAX) of the linac. In the parallel configuration, the beam CAX is parallel to the direction of the main magnetic field. In the perpendicular case, the linac is mounted at a right angle to the direction of B_0 such that they are perpendicular to one another. In both cases the linac source and the MRI's magnet rotate together such that their relative orientation remains constant for all gantry angles. The Lorentz force will act in different directions for the two Linac-MR configurations, and hence will have different implications with respect to dosimetry. In both cases, the dosimetric effects of the magnetic field will be most pronounced in low density regions such as air and lung, where the mean free path between interactions for electrons is longer.

2.2.1 Parallel Configuration

Since the Lorentz force only affects the component of an electron's velocity that is perpendicular to the magnetic field, for the parallel Linac-MR configuration, electrons travelling parallel to the beam central axis will not experience any Lorentz force. However, the majority of

particles diverge from the central axis, and the perpendicular component of their velocity will be influenced by the magnetic field. The vector addition of the movement parallel to B_0 with the circular motion perpendicular to B_0 from the Lorentz force described by Equation 13 will cause the particles to move on a helical path. Therefore, the Lorentz force acts to prevent electrons from moving further away from the beam central axis, since they will move in a helical pattern with a constant gyroradius.

The Lorentz force's confinement of electrons has several dosimetric consequences for a radiotherapy patient. Electrons scattered in the head of the linac will be prevented from scattering out of the beam edges while under the influence of the uniform magnetic field of the MRI. As a result, more electrons reach the skin of the patient within the projected collimated field edges, resulting in an increase in the entry skin dose to the patient (55). In most regions inside a patient the mean free path of electrons is much shorter than in air, which reduces the impact of the magnetic field on electron trajectories. However in lung, where the mean free path is longer, dose distributions are significantly hotter within the field edges and colder outside in the presence of a parallel magnetic field (relative to the no magnetic field case). Both of these effects can be seen in the right column of Figure 2.4 below, where the difference map in the lower right corner shows a hotter skin dose, and increased dose inside the beam edges relative to the no magnetic field case (57). The confinement of electrons also results in a slightly reduced beam penumbra, by reducing the contribution from electron scatter (57).

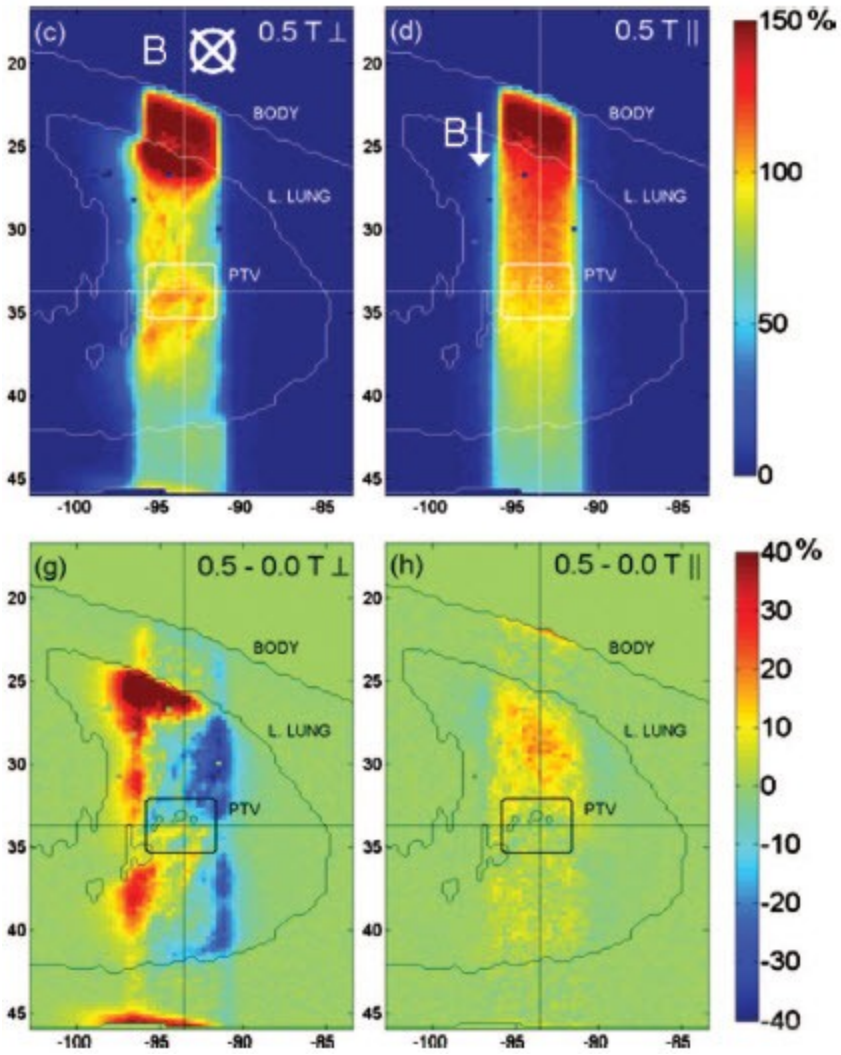

Figure 2.4 Linac-MR dosimetry for an anterior-posterior (AP) field in lung. Top row: dose distributions for a 0.5 T magnetic field, perpendicular (left) and parallel (right) configurations. Bottom row: corresponding difference maps relative to the no field cases. Dose distributions are normalized to same point dose at isocenter (57)

2.2.2 Perpendicular Configuration

For the perpendicular Linac-MR configuration, the Lorentz force on secondary electrons produces different dosimetric effects. The perpendicular magnetic field curves electrons in a direction perpendicular to both their velocity and the magnetic field described by Equation 8b. Since the magnetic field is perpendicular to the central beam axis, this results in a lateral shift in dose distribution relative to the 0T case. Hence a dose difference map of two treatment plans with and without magnetic field will be colder on one side, and hotter on the other side in the direction of the shift (Figure 2.4). The effects are again most significant in low density regions such as air (between the linac head and the patient) and lung, where the mean free path between interactions for electrons is much longer. This results in a reduction in surface dose for the perpendicular configuration, since contaminant electrons from the linac head are swept away from the central beam axis before they reach the patient (67). In regions where there is a tissue-lung/air interface, the Lorentz force can curve electrons back around to strike the exit surface of the tissue. This phenomenon is called the Electron Return Effect (ERE), and results in an increase in dose on any exit surface from tissue to lung or air for the perpendicular configuration. These effects are evident in the left column of Figure 2.4, where we see a dose difference map which is hotter on one side, colder on the other, and has enhanced exit dose at tissue-air interfaces.

2.3 Treatment Planning Systems

This section will describe the basic processes of forward- and inverse-planning, focusing on the components directly relevant to this research project. The starting point for most treatment plans is a CT image set of a patient, which is imported into the TPS to define the patient geometry. The TPS generates a density matrix based on the radiological information contained in the CT image set. The density matrix is a 3D array of electron and/or physical densities required to calculate dose in the patient. A radiation oncologist draws contours on this image set to delineate the tumour volumes, and nearby critical structures (e.g. organs). Next a variety of treatment parameters are defined, which include: number of beams and particle type(s), beam energy, isocenter location(s), field sizes and shapes, gantry/table/collimator angles, dose grid size and resolution etc. (Note that a radiation field is the 2D section perpendicular to the CAX of a radiation beam at isocenter that defines the size and shape of the beam). The way in which the final treatment plan parameters are chosen differs between forward- and inverse-planning.

In conventional forward-planning, treatment parameters are adjusted through manual iterations until an acceptable dose distribution is achieved. Thus, forward-planning is essentially a trial and error treatment planning method, whose speed and plan quality depend on the expertise of the treatment planner. Although the treatment fields can have different shapes to conform them to the PTV, the photon fluence delivered at each gantry angle is either uniform or modulated using simple beam modifying devices (*e.g.* wedges or missing tissue compensators).

2.3.1 Inverse Planning

In contrast to forward planning, inverse-planning delivers non-uniform fluence patterns that are determined by a computer optimization algorithm, and typically delivered using a MLC. Inverse-planning continues to be an active area of research, since there are many different ways to define and solve the inverse problem. This section will briefly describe some of these different approaches, mainly beamlet-based inverse-planning using an iterative, gradient-based optimization algorithm. The most common approach to inverse-planning is to optimize the fluence from each beam. Other parameters such as the number of beams and beam angles can be included as variables in the optimization, although they are commonly selected manually. Beamlet-based inverse-planning splits each radiation field into many smaller pieces called beamlets, each of which can be assigned a different weight. There are often more than a thousand beamlets for a radiotherapy treatment, and it would be impractical to optimize all of the beamlet weights manually. Therefore treatment objectives and variables must be defined in a mathematical form that can be used by a computer optimization algorithm. The algorithm then uses this objective function to determine the optimal treatment plan (i.e. beamlet weights).

2.3.1.1 Objective Functions

The objective function for an inverse-planned radiotherapy treatment uses an expression comparing the desired dose distribution (defined by the treatment objectives and/or constraints), and the actual dose distribution for a given set of beamlet weights. An optimization algorithm minimizes the difference between these two dose distributions by searching for the minimum (or maximum) of the objective function. An example of a simple objective function is shown in Equation 14 below. (Note that the equations in this section are taken from chapter 4 of Van Dyk

Vol 2 (31)). The objective expression sums contributions from all *N* targets and *M* organs at risk (OAR), with each scaled by an assigned weight that reflects the respective priority of the treatment goal for a given target or organ structure.

$$f = \sum_{n=1}^{N} p_n^T \cdot f_n^T + \sum_{m=1}^{M} p_m^{OAR} \cdot f_m^{OAR}$$ Simple Objective Function (31) Equation 14

Where: f_n^T is the objective function for the n[th] target volume
p_n^T is the weight for that target (i.e. penalty for deviating from constraint)
f_m^{OAR} is the objective function for the m[th] OAR
p_m^{OAR} is the weight for that OAR (i.e. penalty for deviating from constraint)

The best form for the objective function is a widely debated subject of the inverse-planning process. There are two main classes of objectives which can be used. Physical objectives depend only on the deposited dose in the patient. Biological objectives attempt to go a step further, by using the dose to predict the biological response to the treatment through the use of biological models. Biological objectives are thus more closely related to the actual goal of the treatment, which is the biological outcome. However, current biological models yield predictions with large uncertainties, resulting in questions about their reliability. Thus, while the use of biological objectives is an ongoing subject of research and development, it is still currently much more common in practice to use physical dose objectives.

Physical objectives can be classified as dose-based, or dose volume-based. Dose-based objectives typically define dose thresholds (i.e. minimum or maximum doses) to relevant structures. Any dose voxels within these structures which deviate from these thresholds are penalized, and contribute to the overall objective function value (sometimes called the 'plan score'). Simple examples of quadratic objective functions for the target volume and OARs are

shown below. The values of these types of objectives are smaller for more optimal plans, with the optimal plan score of 0 signifying that all objectives have been met. The Heaviside function in Equation 16 ensures that only voxels with doses above or below the dose thresholds are penalized. For the target, dose-based objectives can be made more versatile by specifying dose ranges outside which voxels are penalized, rather than computing the quadratic deviation from a single dose value. This is accomplished by splitting the target objective into two parts, one for a lower dose limit and another for a higher one (with the prescription dose lying between the two thresholds). Violations of the upper and lower limits can be assigned different penalty weightings.

Target Objective Function (31) Equation 15

$$f^T = \frac{1}{N^T}\left(p_{low} \cdot \sum_i H(D_{low} - D_i) \cdot (D_i - D_{low})^2 + p_{high} \cdot \sum_i H\left(D_i - D_{high}\right) \cdot \left(D_i - D_{high}\right)^2\right)$$

Where: N^T is the number of voxels for the target, and the summation is over the dose voxels
D_{low} is the lower dose threshold for the target
D_{high} is the upper dose threshold for the target
p_{high} and p_{low} are the weights of the upper and lower dose threshold objectives
H is the Heaviside function defined below

$$H(D_1 - D_2) = \begin{cases} 1, D_1 > D_2 \\ 0, D_1 \leq D_2 \end{cases}$$ Heaviside Function Equation 16

$$f^{OAR} = \frac{1}{N_{OAR}} \sum_{i=1}^{N_{OAR}} H(D_i - D_0^{OAR}) \cdot (D_i - D_0^{OAR})^2$$ OAR Objective Function (31) Equation 17

Where: N_{OAR} is the number of voxels in an OAR
D_i is the dose to the i^{th} voxel
D_0^{OAR} is the chosen tolerance dose for the OAR
H is the Heaviside function

The dose in voxel i is the sum of the contributions from all beamlets:

$$D_i = \sum K_{ij} \cdot \omega_j \qquad \text{Summed Beamlets (31)} \qquad \text{Equation 18}$$

Where: K_{ij} is the dose contribution from the j^{th} beamlet to the i^{th} voxel
ω_j is the fluence weighting of the j^{th} beamlet

Dose-volume objectives incorporate fractional volume into the objective function, and are more commonly used than dose-based objectives due to several advantages. These advantages include: better control of resulting dose distributions; more flexibility in the optimization process; and the ability to use research on clinical outcomes resulting from specific dose-volume end points to define objectives (particularly for OARs). Dose-volume histograms (Section 2.3.5) are an essential tool for treatment plan evaluation, and by using dose-volume objectives these evaluation criteria can be directly incorporated into the optimization. To incorporate dose-volume objectives, it is necessary to parametrize the volume constraints into dose values in the objective function. For example, you can specify that the volume V of a structure which receives dose greater than D_1 must be less than V_1 , i.e. $V(>D_1)<V_1$. In this case the dose value D_2 on the current DVH where $V(D_2)=V_1$ is used to construct an objective based on dose only, with implicit volumetric information (31).

$$f = \frac{1}{N}(p \cdot \sum_i H(D_2 - D_i) \cdot H(D_i - D_1) \cdot (D_i - D_1)^2 + \cdots) \qquad \text{Dose Volume Based Objective (31)} \qquad \text{Equation 19}$$

Where: N is the number of voxels for the structure
p is the weight of the objective for this structure
D_i is the dose to the i^{th} voxel
D_1 is the tolerance dose defined in the objective
D_2 is the current cumulative dose value to the specified volume V_1
… signifies that multiple objectives for the same structure can be used

In addition to dose or dose-volume formulations, objectives using the concept of equivalent uniform dose (EUD) are not uncommon, and represent a hybrid of physical and biological objectives. The generalized form of EUD can be applied to both tumours and OARs, and represents the uniform dose that would result in the same amount of cell killing (tumour) or risk of injury (OAR) as the heterogeneous dose distribution. It is mathematically defined as follows:

$$EUD = \left(\frac{1}{N}\sum_{i=1}^{N} D_i^a\right)^{\frac{1}{a}}$$ Equivalent Uniform Dose Equation 20

Where: N is the number of voxels in the structure

D_i is the dose in the i^{th} voxel

a is the tissue specific parameter that describes the biological dose-volume effect

The value of the parameter 'a' dictates the relationship between EUD and the dose-volume distribution. When *a* is set to +∞ (-∞) then the EUD is equal to the maximum (minimum) dose for the structure. When it set to 1 the EUD is the arithmetic mean dose to the structure, and when it is set to 0 it is the geometric mean. Relevant to the understanding of EUD is tissue architecture and the concept of functional subunits (FSUs) constituting each OAR. OARs are classified as either: serial, where the FSUs are organized in series, and if any subunit receives more than the tolerance dose then the organ as a whole cannot function properly (e.g. spinal cord); or parallel, where the FSUs are organized in parallel, and the fractional volume receiving a certain dose is the threshold for complications (e.g. lung). Tumours typically would have large negative 'a' values assigned, corresponding to the minimum dose being the most important quantity with respect to tumour control. Serial structures typically have large positive values, making the maximum dose the most important metric for overall biological response, and risk of

unwanted complications. In contrast, parallel structures typically have 'a' values close to 1 such that the mean dose is the metric best describing the biological response of the OAR. The parameter 'a' can be determined empirically using dose-volume data, or can be treated as an adjustable parameter used to achieve the best possible dose distribution.

2.3.1.2 Optimization Algorithms

The form of the objective function often determines the appropriate type of optimization algorithm to be used. As described in Van Dyk (31), there are many different types of optimization algorithms, each with associated strengths and weaknesses. The most common types of algorithms are iterative, meaning that they repeatedly go through the process of adjusting the treatment parameters (beamlet weights), calculating dose distributions, and evaluating the objective function score until the optimal solution is found. Iterative algorithms can be classified into two main types: statistical algorithms, and gradient-based (deterministic) algorithms. For statistical optimization algorithms, the step size and direction for each iteration is random. This typically requires many more iterations than gradient-based algorithms to reach an acceptable plan score, since they are more random in nature. There are often limitations placed on the number of iterations or the total computation time, and under these conditions there is no guarantee that the final plan is the most optimal. This type of optimization is typically used when the objective function is not analytically differentiable. The main advantage of statistical methods is that they do not get trapped in local minima as easily as gradient-based methods.

Gradient-based algorithms calculate the gradient (and sometimes higher order derivatives) of the objective function, in order to calculate the direction in which it is decreasing. These derivatives can be computed either analytically (which requires an appropriate form of the

objective function), or numerically (which is generally much slower). The objective function derivatives determine the direction of changes to the parameters for the optimization, and often the step size for the iteration (although this may also be set manually). Gradient-based algorithms are generally faster than statistical algorithms, since they require fewer iterations to converge to the optimal solution (objective function minimum). However they limit the form of the objective function, since it must be appropriately differentiable. The main drawback of this type of algorithm is that it can become trapped in local minima that may be far from the optimal solution (global minimum) if the objective function is not convex. Sequential Quadratic Programming (SQP) is an example of an iterative optimization method that is used for nonlinear optimization problems. It requires that the objective function (and constraints if they are present) be twice continuously differentiable. The SQP algorithm uses Taylor expansions to replace the objective and constraint functions with quadratic and linear approximations respectively. It generates a quadratic sub-problem for each iteration, which it must solve to generate the next step. The SQP method can be considered a generalization of Newton's method of optimization, which finds the stationary points of a twice differentiable function. With the same step size, Newton's method is able to find the function minimum (or maximum) faster than methods relying on the gradient (first order derivative) only.

2.3.2 Dose Calculation

There are two main approaches to dose calculation for radiotherapy treatments: correction-based methods, and model-based methods. With correction-based methods, tabulated data measured in water is used to first calculate an equivalent dose in the patient assuming that

the patient is homogeneous, and then correction factors are applied to account for heterogeneities. Correction-based methods provide reasonable accuracy in many clinical situations; however the accuracy is dependent on very well defined conditions, such as charged particle equilibrium (CPE) in both the lateral and depth directions, and the geometry of heterogeneities being relatively simple (e.g. slab-like where there is no large change in contour, like in a flat water tank). Therefore, correction-based methods do not work well in dose buildup regions, or for complex patient anatomies, such as at tissue-lung interfaces. Since this study will focus on magnetic field effects in lung, correction-based methods are not acceptable for dose calculation due to their limited accuracy for complex heterogeneities, and their inability to model magnetic field effects.

Model-based dose calculation methods model radiation transport more explicitly, giving them improved accuracy in complex situations. One large advantage of model-based methods is that they describe how the energy due to scattered photons and electrons spreads out in a medium; since they incorporate electron transport, they are superior in regions where CPE does not exist. Convolution and superposition algorithms are model-based methods that use dose deposition kernels. These kernels describe how energy fluence at a given location deposits energy everywhere in a patient or phantom. Dose kernels can be either spatially invariant, or spatially variant. Spatially invariant kernels are only strictly applicable for homogeneous mediums. Under such isotropic radiological conditions the same spatially invariant kernel can be used to describe the spread of energy from any given location. Spatially variant kernels become necessary as soon as heterogeneities are introduced, since for example a given energy fluence in water will deposit dose differently in lung.

In TPSs, these kernels are typically parametrized in either two dimensions (pencil kernels) or three dimensions (point kernels). Pencil kernels describe how fluence in a given 2D plane deposits energy in the 3D calculation volume. They are specified as functions of both lateral directions at given depths; thus when calculating the contributions from a given fluence element to a specific dose voxel, contributions of the point fluences along the depth direction are effectively pre-integrated. Point kernels describe the fraction of energy originating from a 3D point of interaction that reaches a 3D dose calculation point, and are parametrized as a function of all three directions (*i.e.* are also a function of the depth direction). Point kernels are better able to account for the effects of complex changes in dose distributions due to heterogeneities since the primary fluence is transported through heterogeneous media along the depth direction. To calculate the dose at a given point in a patient, the kernel contributions from all points of interaction in the patient are integrated. This process is known as superposition, and for a pencil (point) kernel approach is described by Equation 21a (21b) below.

$$D(x,y,z) = \iint \Phi_{2D}(x',y')K(x',y',x,y,z)dx'dy' \qquad \text{Pencil Kernels} \qquad \text{Equation 21a}$$

$$D(x,y,z) = \iiint T(x',y',z') \cdot K(x',y',z',x,y,z)dx'dy'dz' \qquad \text{Point Kernels} \qquad \text{Equation 21b}$$

Where:

$D(x,y,z)$ is the dose at point (x,y,z) [Gy]
Φ_{2D} is the photon fluence in a given 2D plane [m^{-2}]
T is the TERMA total energy released per unit mass by primary photon interactions at point (x',y',z') [$J \cdot kg^{-1}$]
K is the scatter dose point kernel describing the fraction of energy deposited at point (x,y,z) by interactions originating at (x',y') or (x',y',z')

2.3.3 Monte Carlo Simulation

Monte Carlo (MC) simulation is a completely different model-based method of dose calculation, one using fundamental interaction probabilities to model the transport of radiation in matter. MC simulation can achieve superior accuracy compared to most other dose calculation methods due to its explicit modeling of radiation transport, particularly for complex geometries. However, it is generally quite slow compared to other calculation methods for the desired level of uncertainty. For this reason MC simulation has not been used in the majority of commercial clinical dose calculation algorithms. However, advancements in computer technology such as a parallel computing, and increasingly powerful computer and graphics processing units (CPU/GPU) continue to reduce the time required to perform MC calculations (54).

MC calculation is a statistical solution to complex problems, such as those with many coupled degrees of freedom. The basic general process involves: defining a domain for the inputs to the calculation; randomly sampling the probability distribution function (PDF) for input values and using them in a deterministic calculation; and summing the results of the calculation over a large number of samples (68). By sampling a known PDF for a stochastic process, MC calculation is able predict the expected outcome with increasing accuracy as the number of samples increases. This is described by the 'law of large numbers', a probability theorem that states "as the number of trials of a random process increases, the percentage difference between the expected and actual values goes to zero" (69). In radiotherapy, MC methods are applied to solve the Linear Boltzmann equation governing radiation transport in matter, which is difficult to solve analytically. Using known PDFs which characterize the interactions of radiation with matter, MC calculation can simulate the random paths of a large number of particles while keeping track of relevant quantities such as energy transferred to regions of interest.

There are several MC software packages used for simulation of radiation transport, of which EGSnrc is one of the most popular in medical physics (70, 71). Two components of EGSnrc are: BEAMnrc, used to simulate radiation transport through linac head components; and DOSXYZnrc, used to simulate radiation transport in patients or phantoms. BEAMnrc can be used to generate a file called a phase space, which defines particle types, energies, positions, and directions exiting the linac head in a chosen plane perpendicular to the beam direction. The phase space can subsequently be used as the particle source for a DOSXYZnrc simulation. DOSXYZnrc also requires a density matrix in order to perform an MC simulation (named a *.egsphant file (70)). For simulation in a patient, this density matrix file is generated using the CT data set on which the treatment was planned in the TPS. The file contains all of the geometric and radiological information needed for the simulation: the number of dose grid voxels in x, y, and z; the coordinates of the intersecting planes of these voxels; the number and names of materials present; and the material and physical density for each voxel (slice-by-slice). Typically, the density matrix used in DOSXYZnrc is created by the program CTcreate, another part of the EGSnrc package. User input to CTcreate is used to define the function for converting the CT data into material types and densities, and to select the sub-volume of the CT data and the voxel resolution for the generated density matrix. CTcreate however has several limitations not mentioned in the associated documentation (70). As described in Appendix A, these limitations result in geometric inaccuracies in the intersecting planes of generated density matrices, and errors generating density matrices for patient orientations other than Head First Supine (HFS) (see Appendix A).

MC codes have several basic components, including: information that characterizes the physics of radiation transport; a random number generator (RNG); techniques for sampling

PDFs; geometry and scoring routines. The physical information for the simulation is related to the particle interactions described in Section 2.1. This includes the total and differential cross sections (probabilities) for photon interactions, as well as the stopping powers and collision types for electrons. This information is the basis for the PDFs needed for the MC simulation. RNGs are algorithms that produce pseudo-random seeded sequences with very large periods, which are necessary to ensure (effectively) random sampling of the PDFs in the simulation. The default random number generator used by EGSnrc produces a sequence with a period of greater than 10^{165} (72).

Photons and electrons are used for the majority of MC simulations in radiotherapy, and they are each simulated differently. This originates from the fact that the mean free path of electrons is much shorter than for photons in the same medium. Photons generally use analog simulations, meaning every interaction is simulated individually. For each photon, first the photon transport algorithm determines the distance to the next interaction (using a PDF based on the linear interaction coefficient). It then transports the photon to the interaction point taking the geometry of the medium into account to make sure that it doesn't cross a boundary (which would change the attenuation coefficient). The algorithm then generates a pseudo-random number determining the type of interaction the photon undergoes, based on the relative probabilities of the different interactions for the given photon energy and the medium. Finally the differential cross sections for the chosen interaction process are sampled to calculate the energies and directions of all particles generated by the interaction. This process is repeated until the photon energy reaches the user-defined lower cutoff energy below which it is no longer tracked.

Electrons interact much more frequently, and most interactions result in very small changes in energy and direction. It is therefore useful to condense large numbers of these

interactions into a small number of steps through the use of condensed history (CH) algorithms, which were first developed by Martin Berger in the 1960s (73). In typical modern CH implementations, interactions are divided into low energy soft interactions that are subject to grouping, and hard interactions that are simulated individually. Hard interactions are those resulting in a large loss of energy by the incident electron, which include: hard bremsstrahlung emission; positron annihilation; and large energy loss Møller or Bhahbba scattering. Soft collisions corresponding to small changes in energy, and that are grouped by the CH algorithm include: elastic scattering; soft bremsstrahlung emission; and low energy loss Møller or Bhahbba scattering. The two main components of CH algorithms that influence the simulation speed and accuracy are: the electron step algorithm dealing with the physics of electron transport; and the boundary crossing algorithm that determines how the simulation handles boundaries between different material types. CH techniques have a dependence on the size of each step, which the user can set to a maximum value. As in photon simulations, the electron step algorithm also starts by sampling the distance to the next discrete interaction (i.e. hard collision). It then transports the particle to the interaction site, but differs from the photon algorithm in that it accounts for changes in direction of the electron due to the condensed multiple low energy scatter events that occur during this one step. This requires sampling from a probability distribution describing this multiple scattering. The algorithm then determines which hard interaction takes place (by sampling relevant PDFs), and alters the energy and direction of the particles accordingly. Boundaries between different materials complicate MC simulations, since they change the physical environment of the transported particle. The Parameter Reduced Electron Step Algorithm (PRESTA) in EGSnrc imposes step size restrictions for electrons to deal with this challenge. On modern implementations of PRESTA (II), when an electron is less

than the minimum step size t_{min} from a boundary, the simulation then invokes single scattering to track each interaction of the electron separately until it moves away from the boundary. This makes the simulation much slower in the presence of boundaries.

$$\epsilon = \frac{1}{\sigma^2 T} \quad \text{Efficiency} \qquad \text{Equation 22}$$

Where: T is the computing time to obtain a variance of σ^2

σ^2 is the variance on the quantity of interest

The efficiency of a MC simulation is defined by Equation 22. Efficiency is improved by reducing the computing time it takes to reach the desired level of variance. There are two classes of techniques that facilitate this goal: approximate efficiency improving techniques (AEITs) make some approximation with respect to the physics of the simulation in order to improve the efficiency; true variance reduction techniques (VRTs) do not alter the fundamental physics of the simulation, but alter the sampling methods so more time is spent on selected parts of the simulation (like certain particles or regions of interest). The CH technique is an AEIT which is almost always used for MC simulations in radiotherapy. Two other common AEITs are range rejection, and transport cutoffs. Range rejection terminates an electron history and deposits its energy locally if its range is less than the distance to the nearest region, or if it is far from a specified region of interest. This reduces the time spent on simulating particles which do not contribute useful information. Transport cutoffs are defined by the parameters ECUT and PCUT in EGSnrc, which are the electron and photon cutoff energies respectively. Below these energies the particles are no longer tracked, and do not generate any new particles.

True VRTs increase the variance of certain quantities in order to reduce the variance in other selected quantities of interest. VRTs used in radiotherapy MC codes include interaction

forcing, Russian roulette, and bremsstrahlung splitting. Interaction forcing is used when the chosen quantity of interest occurs very infrequently (i.e. is based on very low interaction probabilities). This technique artificially increases the interaction cross-sections for the desired process, and reduces the weighting of the generated particles accordingly. For example you could increase the likelihood of a particular interaction by a factor of 100, and reduce the weight of the resulting particle(s) by the same factor. Russian roulette eliminates a fraction of chosen low interest particles, with a probability p that they will be thrown out. It then increases the weight of the surviving particles by a factor of $\frac{1}{1-p}$. This technique is useful when there is a type of particle that does not significantly contribute to the dosimetric quantity of interest - for example, secondary electrons from the head of a linac, if increased uncertainty in the surface dose is not a concern. Another commonly used VRT is bremsstrahlung splitting. Instead of increasing the likelihood of a particular interaction, the technique increases the number of photons generated from a bremsstrahlung interaction by a splitting factor (S). Similar to some other VRTs, the weight of each of these photons is then decreased accordingly by a factor of 1/S. There are different implementations of bremsstrahlung splitting: uniform bremsstrahlung splitting (UBS) uses a constant value of S; selective bremsstrahlung splitting (SBS) has a variable S value that depends on the probability the photon is directed towards a region of interest; directional bremsstrahlung splitting, also uses a variable *S*, but employs a more efficient implementation that further increases the efficiency, as compared to SBS. All of these techniques use Russian roulette on the charged particles generated by split bremsstrahlung photons in order to preserve the variance reduction benefit.

2.3.4 Discrete Superposition of MC Simulated Beamlets

MC simulation can be used to generate patient specific dose kernels for use in forward- and inverse-planning. A two-dimensional radiation field can be split up into equally sized subfields, which will be called *bixels* (beam-pixels) from this point forward. EGSnrc can be modified to generate a MC simulated pencil beam dose kernel called a *beamlet* for each bixel. (67). These beamlets are spatially-variant dose kernels that account for heterogeneities, magnetic fields, and changes in electron energy fluence in all three dimensions due to interactions with the patient/phantom. Thus, the beamlets map the photon fluence through a given bixel to the dose it contributes to every voxel of the calculation volume. These beamlets can be used for dose calculation by discrete superposition, i.e. by looping over all bixels, summing the contribution from each beamlet weighted by its bixel fluence.

$$D(x,y,z) = \sum_{bixel} \Phi_b D_b(x,y,z) \qquad \text{Bixel Summation} \qquad \text{Equation 23}$$

Where:

$D(x,y,z)$ is the dose at each point in a 3D volume [Gy]

Φ_b is the photon fluence for a particular bixel [m^{-2}]

$D_b(x,y,z)$ is the dose at each point in the 3D volume from that beamlet [Gy]

The MC beamlets can be used during the inverse-planning process to optimize the fluence weighting of each bixel. This enables the optimization to operate quickly with the accuracy provided by MC methods (incorporating patient heterogeneities and magnetic field effects), without having to re-simulate in order to calculate dose (since the dose from each bixel is simply scaled by its weight). The output of the optimization is the bixel fluence.

2.3.5 Dose Metrics: Isodose Curves, Dose Profiles, and Dose Volume Histograms

Dose metrics are used to evaluate and compare treatment plans. The main metrics include max/min/mean doses, isodose distributions, dose profiles, and dose volume histograms. Isodose curves are lines which join points of equal absorbed dose in a chosen 2D plane. These dose values can either be expressed as percentages of a chosen dose value, or as absolute dose values. Isodose distributions are groups of isodose curves chosen at user-defined intervals (which can be labeled or colour coded), and are one of the primary methods of visualizing radiotherapy treatment plans for evaluation. Dose distributions from two different plans are often subtracted from one another to compare and visualize differences between the plans.

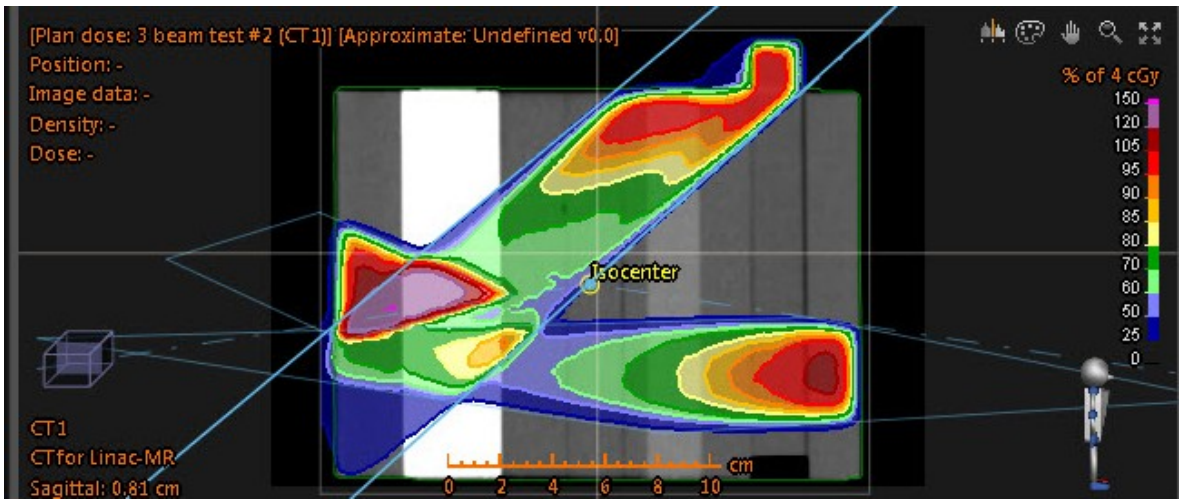

Figure 2.5 Isodose distribution for three coplanar beams in a sagittal plane. The isodose lines are percentages of a 4 cGy reference value. Dose is hottest (red) at the surface of the phantom and decreases as the beams are attenuated.

In three dimensions these curves become isodose surfaces, although they are most commonly viewed in various 2D planes of an imaging set for a patient. In one dimension, dose is represented by a dose profile that expresses the absorbed dose values along a particular line in a patient. Relative dose profiles are normalized to a reference value, commonly the maximum

dose value (100%) along the central axis. The most common dose profiles are: the percent depth dose (PDD), which is the dose profile along a beam's central axis in the depth direction; and dose profiles perpendicular to the beams central axis (Figure 2.6). Primary photon fluence decreases exponentially with depth according to Equation 1. Electron fluence in the medium increases rapidly to a maximum, and then falls of exponentially along with the attenuated photon fluence. Since dose is deposited in the medium by this secondary electron fluence (Equation 10), the PDD for a photon beam increases rapidly to a maximum before falling off as the photon and electron fluences decrease.

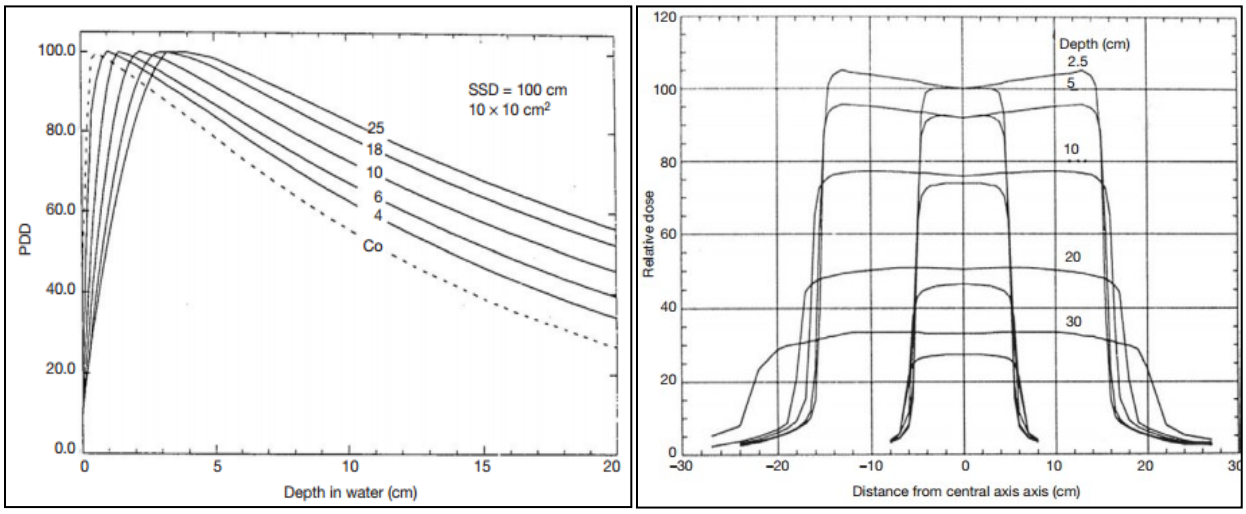

Figure 2.6 Dose profiles in water. (Left) Percent depth dose curves for a variety of linac photon energies [MV] and a Cobalt-60 beam. (Right) Beam dose profiles perpendicular to the central axis for a 10MV photon beam with 10x10cm^2 and 30x30cm^2 field sizes at various depths. (74)

Another quantitative tool for treatment plan evaluation and comparison is the dose volume histogram (DVH), which graphically summarizes the volumetric dose information from 3D dose distributions for regions of interest (ROIs) in a patient. Common ROIs can include the whole body, organs at risk (OARs), and tumour target volumes such as the PTV and ITV. There are two types of DVHs, cumulative and differential (Figure 2.8). Differential DVHs show the

fractional volume of an ROI with dose within chosen ranges (bins) as a function of dose. This allows the volume of the ROI receiving a specific dose value to be visualized. Cumulative DVHs on the other hand, show the percentage of ROI voxels that receive a given dose or greater as a function of dose. An example would be the use of a cumulative DVH to verify that the PTV receives the prescribed dose of 4800cGy to 95% (or more) of its volume.

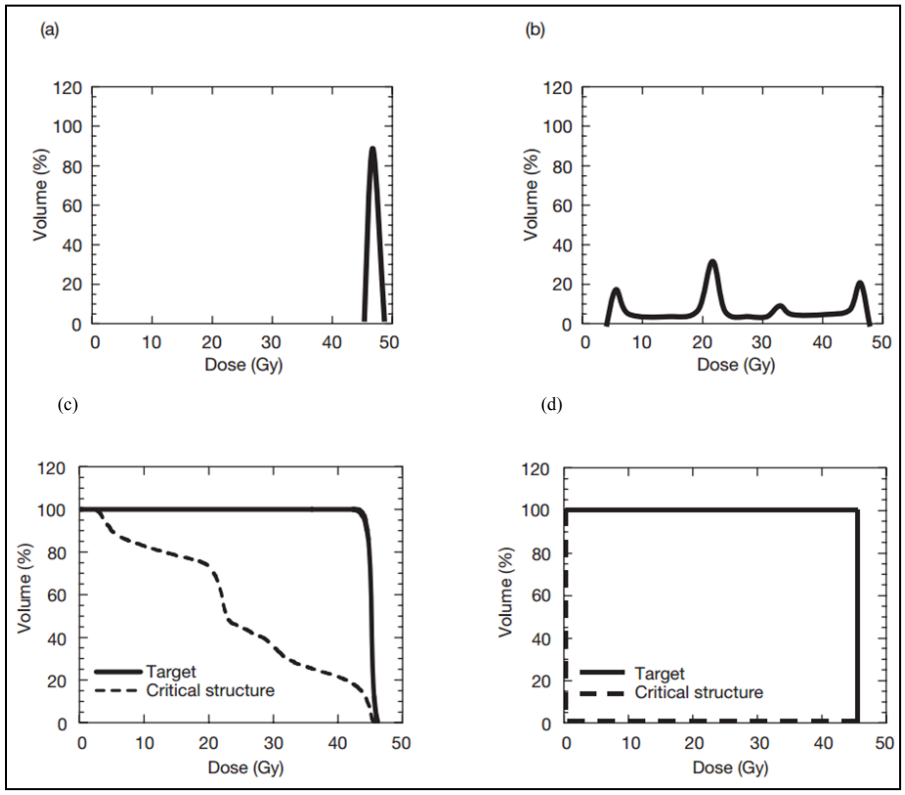

Figure 2.7 Dose Volume Histograms. (Top) Differential DVH for a four field prostate treatment plan for the (a) target and (b) the rectum. (Bottom) (c) Cumulative DVH for the same prostate plan. (d) An ideal cumulative DVH where 100% of the target receives the same uniform dose and the rectum receives no dose. (75)

Figure 2.7 d) shows the theoretical ideal cumulative DVH for a treatment plan where the target receives a completely uniform dose and the critical structure receives no dose. This is not achievable in practice, but common goals are to reduce the dose to critical structures as much as

possible and to deliver the most uniform dose possible to the target. On a cumulative DVH, this pushes the curve for the critical structure down and to the left, and the curve for the target would ideally be flat at 100% until the minimum desired dose value, where it would then fall off as steeply as possible.

2.3.6 Coordinate Systems

There are several coordinate systems which are needed to define the patient and treatment geometry in the TPS, generate a density matrix, simulate the treatment in EGSnrc, and import the results of that simulation back into the TPS for beamlet based optimization (further details on coordinate systems and transformation can be found in Appendix A) :

- ***DICOM patient coordinate system***: This is the coordinate system used by the CT scanner when a patient is scanned. When a CT series is imported into a TPS, it is automatically registered with the coordinate system used by the linac, allowing for the treatment to be planned.
- ***IEC 61217*:** The International Electrotechnical Commission 61217 document provides an international standard for coordinates, movements and scales for radiotherapy equipment. It includes a description of a collection of parent-daughter coordinate systems used to define the linac geometry for radiotherapy treatments on most TPSs, including gantry/table/collimator angles and jaw/MLC positions. The goal of this document is to avoid "ambiguity, confusion, and errors which could be caused when using different types of equipment" (40).

- ***EGSnrc coordinate systems***: BEAMnrc utilizes its own coordinate system that describes the linac components, as well as the position and momentum of particles (71). DOSXYZnrc uses a related coordinate system, which implements three parameters (θ, ϕ, ϕ_{col}) in coordinate transformations mapping the particles from the BEAMnrc simulation onto a patient or phantom geometry (70). When running MC simulations for a patient in DOSXYZnrc, the CT series is used to generate a density matrix file. Thus, the coordinate system used for the simulation is in fact the DICOM patient coordinate system. However coordinate transformations for obtaining the appropriate (θ, ϕ, ϕ_{col}) to relate the coordinates from the BEAMnrc simulation to the patient coordinate system are required to reproduce the treatment geometry in the DOSXYZnrc simulation (Appendix A).
- ***Beam coordinate system RS***: The RayStation (RS) TPS (Raysearch Laboratories Stockholm, Sweden) uses this coordinate system to define the collimator jaws and MLC positions. It is a 2D coordinate system defined in the isocenter plane, with jaw and MLC positions defined in terms of their projections onto this plane.

Chapter 3: Methods

This chapter presents the methodology used for this research, which can be divided into two main parts. The first part consisted of establishing and validating a calculation framework for the project, and is described in Section 3.1. The second part used this calculation framework to evaluate the impact of magnetic fields on the calculation of dose distributions for a lung patient in a variety of scenarios, which is covered in Sections 3.2 - 3.4.

3.1 Establishing and Validating the Calculation Framework

The calculation framework for this project included two systems: 1) a research version of the RayStation (RS) TPS, and 2) the WestGrid High Performance Computing Cluster (HPCC). The research RS system included an experimental dose calculation algorithm that implemented a discrete superposition of MC beamlets. This allowed user-supplied beamlets (*e.g.* that incorporate magnetic field effects) to be used in the forward calculation and optimization of dose distributions. MC beamlet calculations were performed on the Westgrid HPCC using a version of EGSnrc that was modified to generate beamlet dose distributions, and to incorporate the magnetic fields (0T, 0.56T, 1.5T) relevant to this study (67). The details of the benchmarking and validation of this modified EGSnrc code can be found in Appendix B. The process of establishing and validating the calculation framework for this study, depicted in Figure 3.1, included: importing a patient CT study and definition of plan parameters in RS; writing an IronPython script to export the information from RS needed by EGSnrc for MC simulation; generating MC beamlets on Westgrid; importing and validating the MC beamlets in RS.

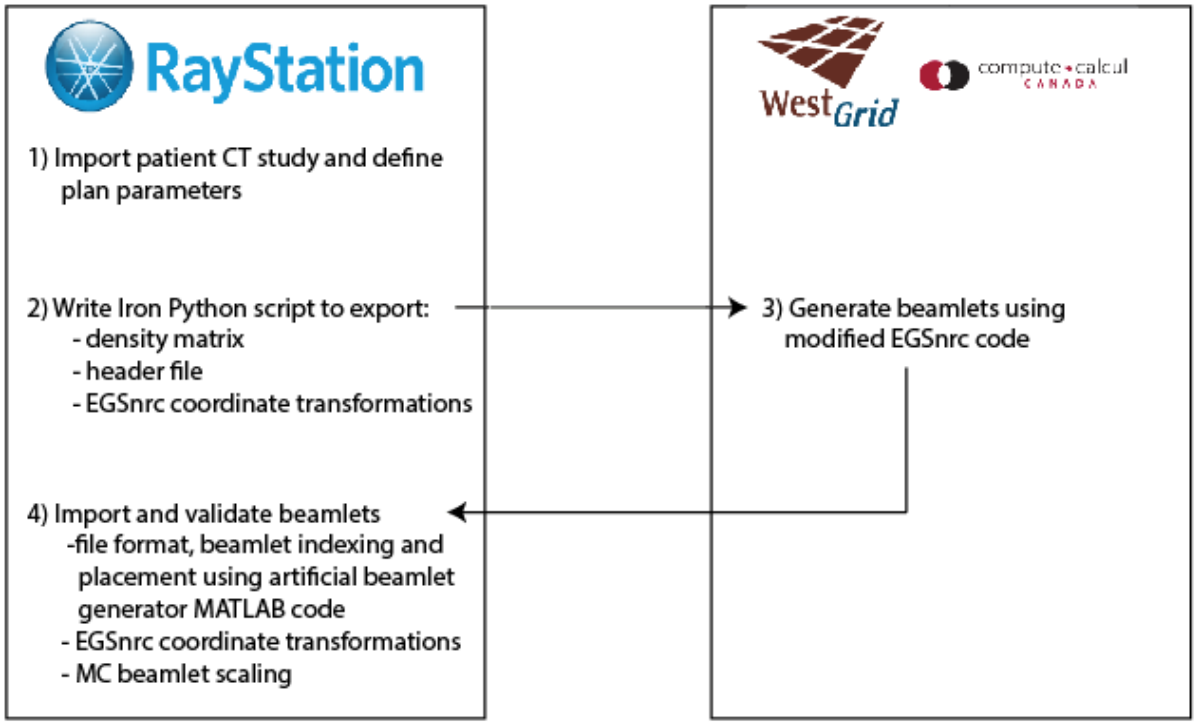

Figure 3.1 Establishing and validating the calculation framework.

3.1.1 Transferring Information between RS and EGSnrc: Density Matrix and Header Files

After importing a CT study into RS, treatment plan parameters were defined. Two files were needed to pass necessary information between RS and EGSnrc. The first file was the density matrix which was described in Chapter 2. An IronPython script was written for generating and exporting the density matrix, which resolved the issues with CTcreate described in Appendix A. This script produced density matrices that were geometrically accurate for all four commonly used patient orientations in radiotherapy: Head First Supine (HFS), Feet First Supine (FFS), Head First Prone (HFP), and Feet First Prone (FFP). The second file is called the header file, and was used to define the simulation parameters in DOSXYZnrc, and by RS during import of the beamlets. Figure 3.2 contains an example header for a single beam. The header information used by DOSXYZnrc to setup and run the simulation includes: dose scoring grid size, resolution, and location in the DICOM patient coordinate system; treatment beam geometry

(collimator positions, gantry, table, collimator angles); bixel field size and location; the format of the beamlet file; and the source axis and source phase-space distances (SAD, SPD). The header also contained the transformed plan parameters $(\theta, \varphi, \varphi_{col})_{DOSXYZ}$ needed by DOSXYZnrc to place the phase space relative to the patient for the simulation, as well as parameters needed by RS to orient the bixel fields correctly with respect to the patient anatomy.

```
# File Version 0.3, RS Version 3.99.09
# export linacMR data Feb52014.py  header generated on 9/10/2014 1:57:01 PM  with 1cm margin

# Patient Info
PatientName               := Daniel MRTP Lung1
PatientID                 := Daniel 1
Comments                  := Testing for MC bixel generation and input of bixels

# CT
CTStudy                   := CT 1
CTPixelDimensions         :=   512,   512,   161                    #(x,y,z)
CTPixelSize               :=     0.10,     0.10,     0.30           #(x,y,z: cm)

# Dose Calculation Grid
DoseGridDimensions        :=   133,   100,    77                    #(DICOM x,y,z)
DoseGridVoxelSize         :=     0.30,     0.30,     0.30           #(DICOM x,y,z: cm)
DoseGridCornerOfCorner    :=   -19.28,    -6.36,   -36.65           #(DICOM x,y,z: cm)
DensityMatrixFileName     :=
E:\Bixel Optimization Project\RS MC Bixels\Daniel MRTP Lung1\F9 Bixel .56T hetero\\density.dat

# Plan Info
PlanName                  := F9 Bixel .56T hetero
NumberOfBeams             := 1

# Beam 3 Info
BeamNumber                :=     9.00
Modality                  := Photons
BeamName                  := 9
FieldSize                 :=    -2.80,     2.96,    -2.40,     2.30   #(x1, x2, y1, y2 cm)
Energy                    :=     6.00                                 #(MV)
GantryAngle               :=   332.00                                 #(Degrees IEC c.s.)
CollimatorAngle           :=   270.00                                 #(Degrees IEC c.s.)
CouchAngle                :=     0.00                                 #(Degrees IEC c.s.)
Isocenter                 :=   -3.47,   18.84,  -28.1                 #(DICOM x,y,z: cm)
EGSPhi                    :=   242.00                                 #(Degrees DOSXYZ c.s.)
EGSTheta                  :=    90.00                                 #(Degrees DOSXYZ c.s.)
EGSPhiCol                 :=     0.00                                 #(Degrees DOSXYZ c.s.)
BixelHeaderFilename       := header.txt
BixelDataFilename         := beam3hetero56T.dat
BixelErrorFilename        := beam3hetero56T.err
BixelSize                 :=     0.50,     0.50                       #(height,width: cm, beam coordinate system)
BixelFieldCornerOfCorner  :=    -3.80,    -3.50                       #(x,y): cm, beam coordinate system)
BixelFieldDimensions      :=    16,    14                             #(x,y)

# Binary Data Info
BytesInHeader             := 0
ValuesInRecord            := 250
FormatOfData              := float
OffsetAtBeginningOfFile   := 1000 #28 # bytes
#ReverseBeamletDirection  := P-A          # R-L, P-A or I-S
LastRecordFilled          := true

# Monte Carlo Info
PhaseSpaceFile            :=
PhaseSpaceDistance        := 100.8                                    #(cm)
PhaseSpaceFieldSize       := 10, 10                                   #(cm)
LinacMR_SAD               := 126.0                                    #(cm) this is the parallel magnet configuration
LinacMR_SPD               := 100.8                                    #(cm) source-phaseSpace distance
BeamletScaleFactor        := 1.0
```

Figure 3.2 Example of a header file used to pass important parameters between RS and EGSnrc such as isocenter location, beam angles, collimator positions etc…

3.1.2 MC Simulation of Beamlet Dose Kernels

Once the header files and density matrix were generated, they were imported and used to define the geometry of the simulations in EGSnrc. The geometry of the prototype 2 Linac-MR system at the CCI was simulated in BEAMnrc. This prototype was built using a modified 600C linac, with a longer SAD to accommodate the magnet and yoke of the MRI (SAD of 126 cm and 146 cm for the parallel and perpendicular configurations, respectively). A Varian Millenium 120 MLC was used in BEAMnrc, which has two leaf sizes projected to 5mm (inner 80 leaves) and 10mm (outer 40 leaves) at isocenter. A description of the magnetic fringe field of the 0.56T Linac-MR prototype was provided in previous research of the CCI Linac-MR team (55). The BEAMnrc code used for phase space generation was modified in order to model this magnetic field map data, enabling accurate simulation of radiation transport through the linac components for our 0.56T prototype. This fringe field data was not available for a 1.5T system, and thus changes to the phase space (*i.e.* fluence exiting the linac head) at this magnetic field strength were not incorporated. The only significant consequence of not modeling the magnetic fringe field for the 1.5T system would be an underestimate of surface dose (55), which was not a focus of this study. Therefore, in total 4 phase spaces were generated, one for each combination of Linac-MR geometry (parallel and perpendicular) and magnetic field strength (0T and 0.56T). The 0T phase spaces were used for both 0T and 1.5T DOSXYZnrc simulations in the patient geometry. The phase space was scored below the secondary collimators and MLC at 100.8cm from isocenter for the parallel configuration, and 116.8cm for the perpendicular configuration. Projected to the isocenter plane, the phase spaces were generated for a $10x10cm^2$ field (collimated by the jaws with the MLC open) in both cases, for one billion histories with one thousand times directional bremsstrahlung splitting (DBS).

The phase spaces were used as the sources of particles for simulation of radiation transport through the patient anatomy using a version of DOSXYZnrc that was modified to generate beamlet dose kernels in a bixelated geometry for each field (67). These beamlets included the effects of the magnetic field and patient anatomy, and were subsequently used by the TPS for both forward and inverse planning with MC accuracy. The MC bixels for this project were chosen to be 5 x 5 mm^2 projected to the isocenter plane, to match the projected MLC central leaf width of 5mm. This choice of bixel size allowed the MLC to effectively modulate the fluence delivered to each subfield. Particles for each beam were simulated within a 1 cm (2 bixel) border around the collimated field edges to properly calculate transmission and scatter through the collimators and MLC leaves, as recommended by RaySearch staff. The bixels were indexed according to the 2D RS beam coordinate system (Figure 3.3), which is defined in the isocenter plane. The "BixelFieldCornerofCorner" coordinate from the header file is used to place to bixel field on the patient, and defines the lowest value in x and y of the first bixel. Bixels are indexed from lowest to highest x and y moving fastest in x, i.e. from the bottom left corner of the field row by row until the top right corner.

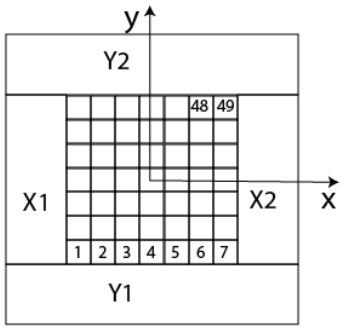

Figure 3.3 A beam's eye view of the collimator jaws projected to the isocenter plane, where the RS beam coordinate system is used to define the positions of the jaws and the MLC (not shown). The MLC is used to modulate the fluence delivered to each bixel; the bixels are indexed from lowest to highest (x,y), moving fastest in x.

One billion histories were simulated with thirty times splitting for both photons and electrons. The electron and photon cutoff energies (ECUT/PCUT) below which particles are no longer tracked were 0.521 keV and 10 keV, respectively. The step size for electrons was set using the ESTEPE parameter which limited the fractional energy lost by an electron in a single step to 0.25. PRESTA-II was used for the electron step algorithm, which invoked single scattering near interfaces. After simulation of each beam, the modified version of DOSXYZnrc output the beamlet dose kernels for all bixels into a single beamlet file for each beam.

3.1.3 Validation of Beamlet Files

To validate the import and interpretation of the beamlet files in RS, a MATLAB script was written to generate artificial beamlets in the same format as the MC simulated beamlets. The artificial beamlet code generated a file containing 100 beamlets, whose associated bixels were projected to 0.6 x 0.6 cm^2 at the isocenter plane. This produced a 6 x 6 cm^2 field, with each beamlet spanning a 2 x 2 column of the $(0.3cm)^3$ dose grid voxels. The code assigned an integer dose value from 1-100 (corresponding to each bixel's number) to the column of voxels under the bixel, and 0 to all other voxels in the calculation volume. This made identifying the location of bixels straightforward, since their associated beamlets contributed dose only to the column of voxels below them in the depth direction. The artificially generated beamlet file was used to verify that RS correctly interpreted the position of the bixel field as a whole, and the placement of each bixel within that field.

Next the placement of MC simulated beamlets in RS was validated. Coordinate transformations were derived for converting the TPS plan parameters defined in the IEC 61217 machine coordinate system to those used in DOSXYZnrc for the MC simulation in the patient

geometry. The details of deriving and validating these coordinate transformations for HFS/HFP/FFS/FFP can be found in Appendix A.

Proper scaling in RS of the dose values in the beamlet files was also required to obtain a reasonable estimate of MUs. This scaling was done using the parameter "Beamlet Scale Factor" in the header file. The applied scaling factor was obtained by comparing the PDDs for the default collapsed cone convolution algorithm in RS to those of the discrete superposition of our MC beamlets, and calculating the factor required to match them at d_{max} using the same number of MUs. The collapsed cone calculation in RS was based on the commissioning of the Varian 2100 linac with a non-standard SAD. Calculation of the scaling factor for the MC beamlets provided a reasonable estimate of the number of MUs required to deliver a given dose distribution. This was done for all three magnetic field strengths (0T, 0.56T, 1.5T), and then averaged to obtain a single scaling factor for each of the parallel and perpendicular configurations. It should be noted that all comparisons in this study were done based on the MC simulated data only. Even though the absolute MU calculation depended on the RS collapsed cone calculation, all MU comparisons are relative and the scaling factor would cancel out (and would therefore not impact the results).

3.2. Impact of Magnetic Fields and Tissue Heterogeneities on Unmodulated Dose Distributions

Once the calculation framework was validated, it was used to generate beamlets for both homogeneous and heterogeneous patient geometries at three magnetic field strengths (0T, 0.56T, 1.5T). Previous studies by our group have shown that the dosimetric effects of the magnetic field on a Linac-MR system are most significant in low density regions such as lung (56, 57). Therefore, a ten field stereotactic body radiotherapy (SBRT) treatment plan for a lung patient was chosen for this study. The SBRT plan was simplified to three of the original ten coplanar

beams, which were selected based on their passing through varying amounts of lung. The PTV for this patient was located against the posterior wall of the right lung, which can be seen in a transverse view in Figure 3.4 below. Beam 1 passes through almost no lung before reaching the target, with beams 2 and 3 traversing moderate and high amounts of lung, respectively.

To study the impact of tissue heterogeneity on dose distributions in the presence of magnetic fields, a MATLAB script was written to generate homogeneous density matrices. These density matrices assigned all values inside the patient to water equivalent physical and electron densities.

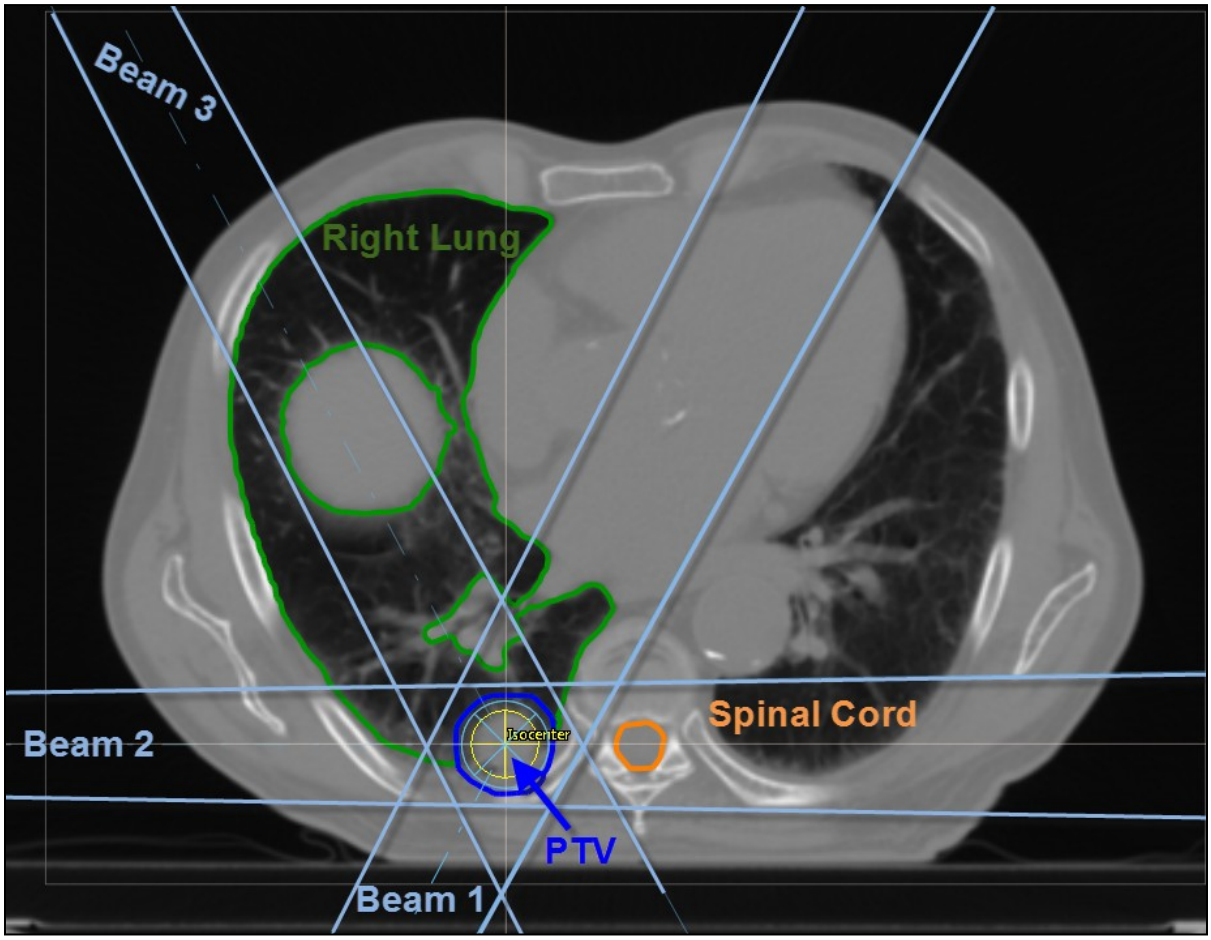

Figure 3.4 Simplified lung patient treatment plan. Transverse view showing projected beam edges, planning target volume, right lung, and spinal cord.

After the beamlets for the lung patient were generated, they were imported into RS and used in a forward calculation to evaluate the effects of magnetic fields and tissue heterogeneity on unmodulated dose distributions (basic forward planning). This was done for all three magnetic field strengths and both heterogeneous and homogeneous patient anatomies. The 0T plans (homo and hetero) were used as a baseline with which to compare the other plans. The collimators and MLC leaves were conformed to the PTV with a 1mm margin in the X direction, and a 4mm margin in the Y direction. These margins were recommended by dosimetrists at our center to account for the asymmetric nature of breathing motion in lung. MC simulated beamlets were read into RS with the calculated scaling factor from Section 3.1.4. Analysis was first performed for each individual beam, then as a composite plan. The single beam plans were normalized such that each field delivered 1600cGy to isocenter. The beams in the composite plan were weighted so that all three beams contributed the same dose to isocenter, and the plan was subsequently normalized to deliver 4800cGy to 95% of the PTV. The resulting treatment plans were compared relative to the 0T baseline using: cumulative dose volume histograms (DVHs) for the target and critical structures; dose difference maps; monitor unit values; and the mean dose to the right lung metric. This analysis of unmodulated plans provided an indication of the potential importance of modeling the magnetic field for inverse planning, which was studied next.

3.3 Impact of Magnetic Fields on Optimization of Modulated Fluences

The beamlets for the lung patient were used to produce optimized fluences for all three magnetic field strengths (0T/0.56T/1.5T), which were compared using a MATLAB script.

3.3.1 Optimization Objectives

RaySearch's proprietary algorithm based on sequential quadratic programming was used to optimize fluence patterns for all three beams. The algorithm was first tested to verify if it was deterministic, by running optimizations multiple times with the same parameters. These optimizations yielded the same results each time, implying that the algorithm was deterministic. A deterministic optimization algorithm was important to ensure that any differences in optimized fluences and dose distributions were a result of the magnetic field (and not the algorithm itself). The optimization objectives were selected to prioritize target coverage and uniformity through use of maximum and minimum DVH dose constraints to the planning and internal target volumes (PTV & ITV). A lower weighting was assigned to the maximum dose constraints on the PTV and ITV, since hotspots are not as much of a concern for SBRT treatments. Constraints were also placed on two normal structure volumes. A maximum DVH dose of 1360cGy (to 3% volume) was used for the spinal cord, the most important critical structure in proximity to the tumour that received significant dose. It was anticipated that the parallel magnetic field would provide some lung sparing in the IMRT plan due to the confinement of scattered electrons. We therefore gradually decreased our maximum dose constraint on the right lung to determine the minimum mean dose to lung we could achieve without compromising our target coverage. This was done on the 0T plan, and then identical constraints were used for all other treatment plans in this optimization study. The final objective constraint for the lung was a maximum equivalent uniform dose (EUD) of 360cGy, with the 'a' parameter in the EUD formula set to 1 (which makes the EUD dose in Equation 20 equivalent to the mean dose, as appropriate for a parallel structure). The optimization objectives used for our study are listed in Table 3.1 below.

Region of Interest	Objective	Weight
PTV	Min DVH 4800cGy to 99% volume	3
PTV	Max DVH 4800cGy to 1% volume	2
ITV	Min DVH 4800cGy to 99% volume	2
ITV	Max DVH 4800cGy to 1% volume	1
Right Lung	Max EUD 360cGy A=1	1
Spinal Cord	Max DVH 1360cGy to 3% volume	3

Table 3.1 Optimization Parameters.

3.3.2 Fluence Comparison

After optimizing the fluences for all beams, magnetic field strengths, and both parallel and perpendicular configurations, the optimized fluences were exported for analysis. A MATLAB (version R2012a, Mathworks Inc, Massachusetts USA) tool was written to display and compare the optimized fluences. This tool computed the global percent difference relative to the 0T optimized fluence for each bixel, and generated a histogram. The formula for the global percent difference calculation is given in Equation 24, where (*x,y*) refer to a specific bixel location:

$$Global\ \%\ difference\ (x,y)_{\overline{B}} = 100 \times \frac{FluenceElement(x,y)_{\overline{B}} - FluenceElement(x,y)_{0T}}{GlobalMax_{0T}} \quad \text{Equation 24}$$

Comparing each bixel of the 0.56T or 1.5T optimized fluence to the global maximum of the 0T fluence provided a measure of the importance of modeling the magnetic field at 0.56T and 1.5T during treatment plan optimization. The greater the fluence differences, the more significant the magnetic field effects, and hence, the less optimal the plan if the magnetic field was ignored during optimization.

3.4 Impact of Magnetic Fields on Optimized Dose Distributions

Finally, the optimized fluences were used in forward calculations to evaluate the importance of modeling the magnetic field of the Linac-MR at each stage of the inverse planning process. The 0T fluence was used to forward calculate with the 0T beamlets and normalized to deliver 4800cGy to 95% of the PTV. This served as the baseline for comparison, and represented the plan quality achievable in the absence of the magnetic field (with the same linac geometry). This baseline was then compared to the following three cases:

Case #1: The 0T fluence was used in forward calculations with either the 0.56T or 1.5T beamlets. The resulting dose distributions were not renormalized after the calculation. The distributions thus represented what would actually be delivered to the patient if the magnetic field was completely ignored during the treatment planning process.

Case #2: The dose distributions from case #1 were renormalized to deliver 4800cGy to 95% of the PTV. This corresponded to the distribution delivered to the patient if the magnetic field was ignored during the optimization but modeled during the forward calculation. Renormalizing the dose distribution changed the number of MUs, but not the fluence pattern.

Case #3: The optimized 0.56T/1.5T fluences were used with their associated beamlets in a forward calculation, and the resulting dose distributions were normalized to deliver 4800cGy to 95% of the PTV. These distributions are representative of the plan quality achievable with the magnetic field modeled during both the optimization and forward calculation stages.

These three cases were compared to quantify and evaluate the importance of modeling the magnetic field at both stages (optimization and forward calculation) of the inverse-planning

process. The treatment plans were compared using the same metrics as the conformal analysis: dose difference maps relative to the 0T plan; DVHs; and mean lung dose.

Chapter 4: Results & Discussion

This chapter is structured to parallel that of chapter 3, with section 4.1 covering the validation of the calculation framework, and sections 4.2 - 4.4 presenting the impact of magnetic fields on un-modulated dose distributions, optimized fluences, and optimized dose distributions, respectively.

4.1 Validation of Calculation Framework

The results of reading in the artificial beamlet file into RS are shown in Figures 4.1 and 4.2 below. Figure 4.1 shows the dose on a coronal slice perpendicular to the beam direction calculated using the artificial beamlets. The beamlet values were created to increase (from 1 to 100) going from -X to +X, and then row by row from -Y to +Y, in the beam coordinate system. For the dose image, ten isodose levels were chosen such that each isodose should span one row of ten beamlets (*e.g.* row 1 = isodose values 1 - 10, row 2 = 11 - 20, *etc.*) and increase from bottom to top, which is consistent with what is seen. Since the increase in dose from –X to +X is not apparent with this choice of isodose levels (using 100 separate isodose levels was not practical), the dose values in rows 2 - 4 (*i.e.* beamlet numbers 11 - 40) were tabulated, and are graphed in Figure 4.2 below. The beamlets adjacent to the collimator edges were omitted from this graph since RS applies a penumbral factor to account for the collimator jaws, which affects the linear correspondence between beamlet number and dose. With the beamlets on all field edges removed, there is a perfectly linear correspondence between beamlet number (x-axis) and dose (y-axis). This confirms that the placement and indexing of the beamlets was interpreted correctly by the RS TPS.

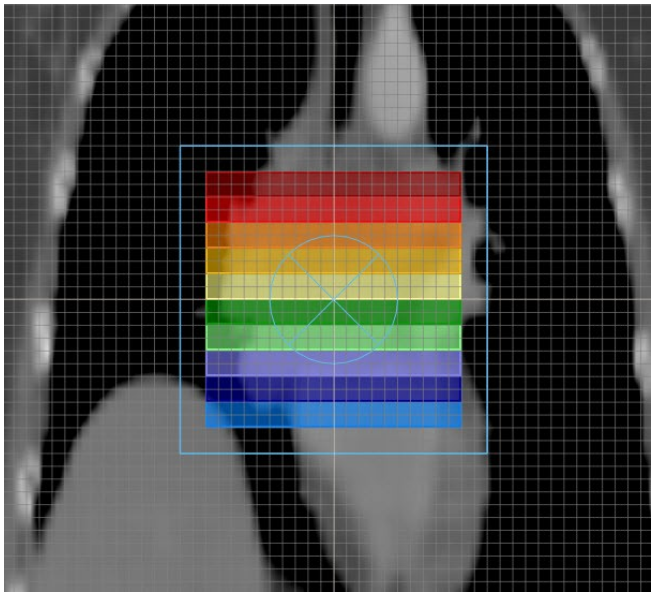

Figure 4.1 Artificially indexed beamlet field read into the RS TPS. This is a coronal slice intersecting isocenter and perpendicular to the depth direction of the beam.

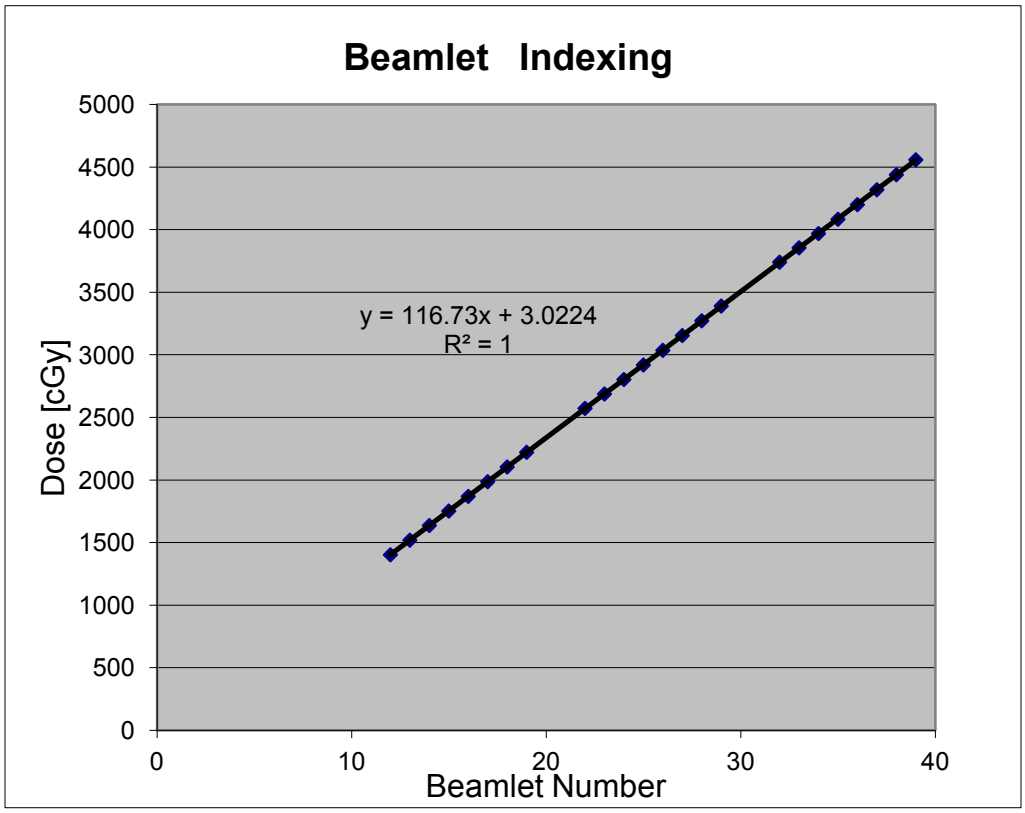

Figure 4.2 Beamlet dose values corresponding to three rows of the artificial beamlet file.

Tests were performed to verify that the coordinate transformations used by the IronPython script to generate the header file and set up the simulation geometry in DOSXYZnrc were accurate. These tests verified the consistency of the geometries of the MC simulated beamlets and the RS treatment plan. The complete details of the derivation and validation of the coordinate transformations is detailed in Appendix A. First, consistency of single beam orientations of increasing complexity, and for all four standard patient orientations, was confirmed. One such validation is shown in Figure 4.3 below, corresponding to a single field from an arbitrary (gantry angle, table angle, collimator angle) combination on a feet-first prone (FFP) patient. The dose distribution lines up with the collimated beam edges in all three orthogonal viewing planes. Finally, a combination of three arbitrary beam directions was simulated, and as shown in Figure 4.4, the dose distributions again line up exactly with the projected collimated beam edges.

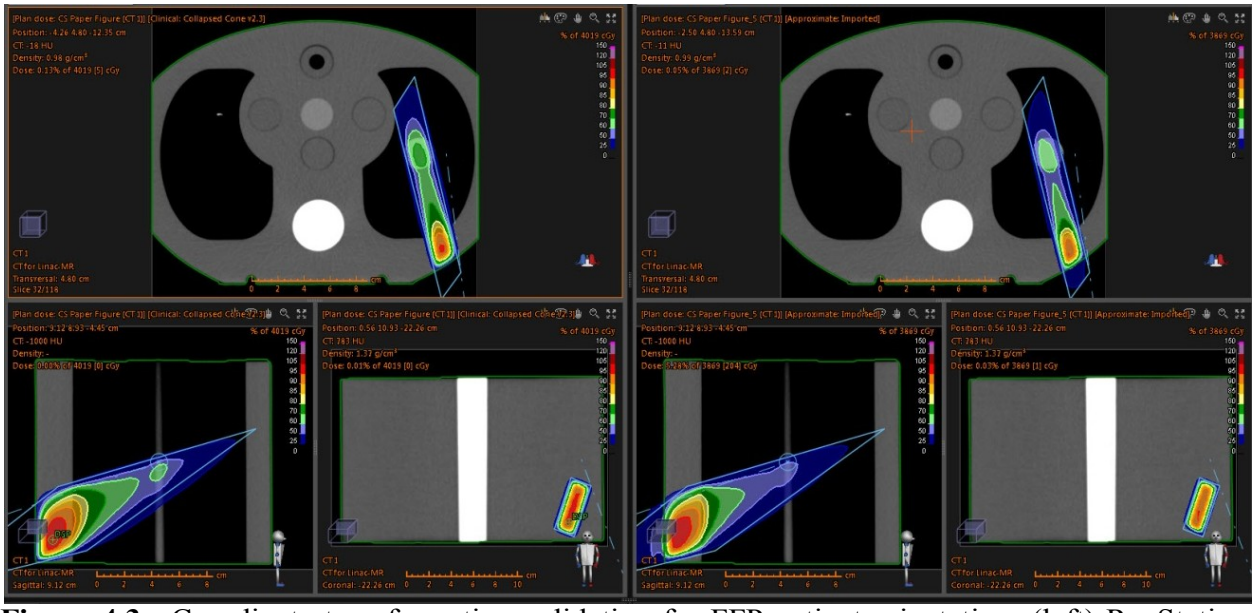

Figure 4.3. Coordinate transformation validation for FFP patient orientation: (left) RayStation TPS default (*i.e.* without MC beamlets) calculation; (right) TPS calculation using imported MC simulated beamlets.

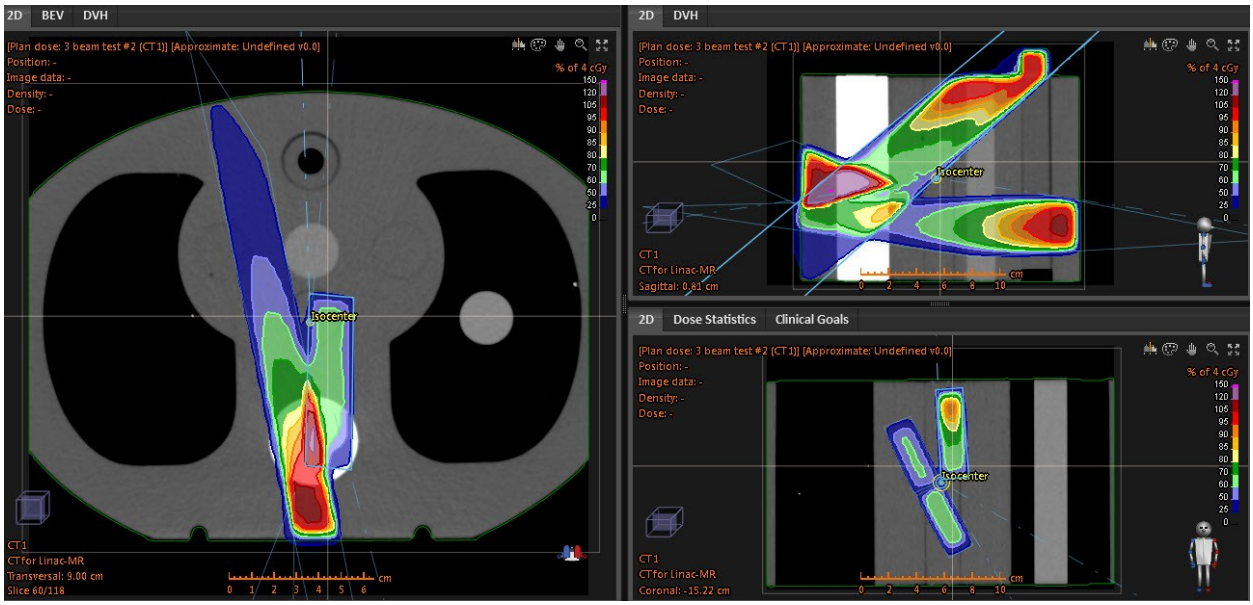

Figure 4.4 Coordinate transformation test using three fields on a head-first supine (HFS) patient. MC simulated beamlets were read into the RS TPS, and the resulting dose distributions line up with the projected collimated field edges (blue lines), confirming the geometric consistency of the beamlet generation with the TPS's treatment plan.

In addition to geometric validation, the appropriate scaling of the MC beamlets when they are read into RS was also verified. Figure 4.5 below shows PDDs for the RS collapsed cone calculation (dashed line) and the MC beamlet-based calculation (solid line) for the parallel configuration after scaling the latter to match the curves at d_{max}. The scaling factors at all magnetic field strengths were calculated and averaged to obtain 0.250±0.002 and 0.328±0.003, for the parallel and perpendicular configurations respectively. We chose to average the scaling factors within each configuration since they differed by ~1%, rather than use a different factor for each field strength. The scaling factors for the parallel and perpendicular configurations were most likely different due to the difference in SAD between these configurations (126 cm for parallel, 146 cm for perpendicular), although this was not investigated rigorously. The purpose of this scaling was to obtain a reasonable measure of MUs for subsequent analysis. However as described previously, since all comparisons were based on the MC beamlet data (not the RS

collapsed cone), the relative accuracy of the dose distributions, DVHs, *etc*. are independent of the absolute number of MUs.

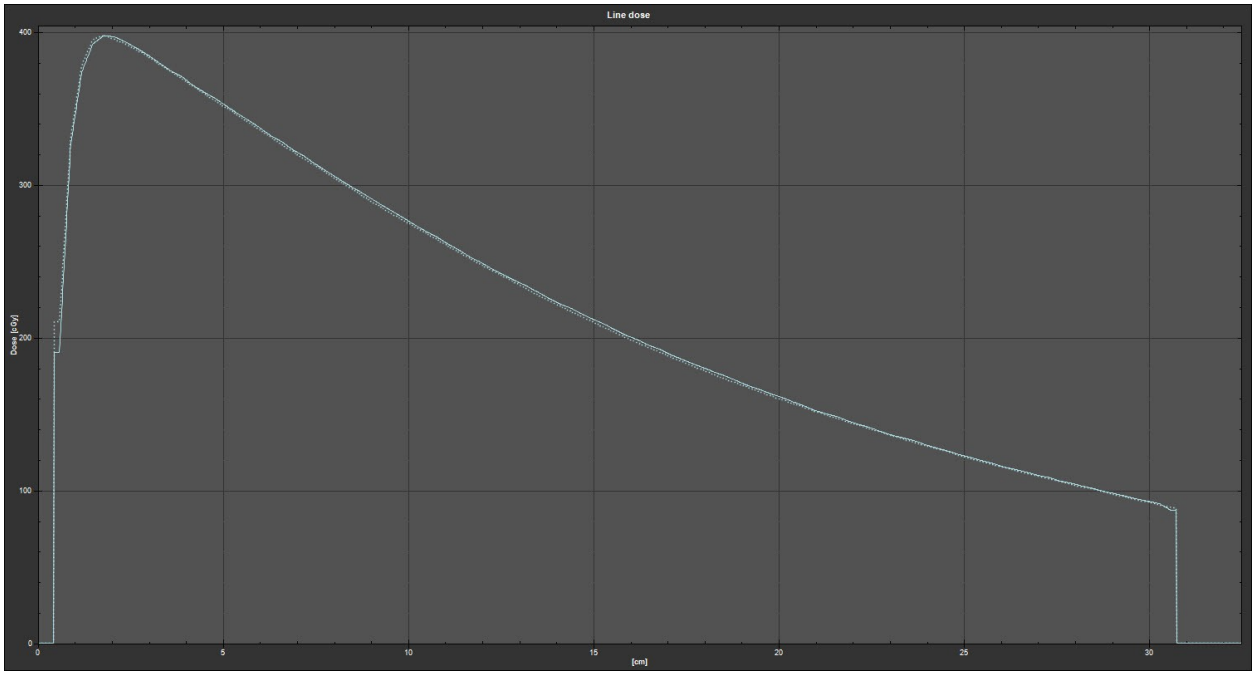

Figure 4.5 Parallel configuration 0T PDD's for RS collapsed cone (dashed line) and MC beamlet-based (solid line) calculations after the beamlet-based dose is scaled to match at d_{max}

4.2 Impact of Magnetic Fields and Tissue Heterogeneities on unmodulated dose distributions

This section presents the impact of magnetic fields and tissue heterogeneities on unmodulated dose distributions. The results are split into two sub-sections, one for the parallel Linac-MR configuration, and one for the perpendicular. Each subsection shows results from a single beam first, and then for the plan. Studying the effects of the magnetic field on unmodulated dose distributions will provide an indication of the potential impact modeling the magnetic field may have on the optimized IMRT fluence and dose distributions in sections 4.3/4.4.

4.2.1 Parallel Linac-MR Configuration with Unmodulated Beams

The two density matrices used to study the impact of the tissue heterogeneities are displayed side by side in three orthogonal viewing planes in Figure 4.6.

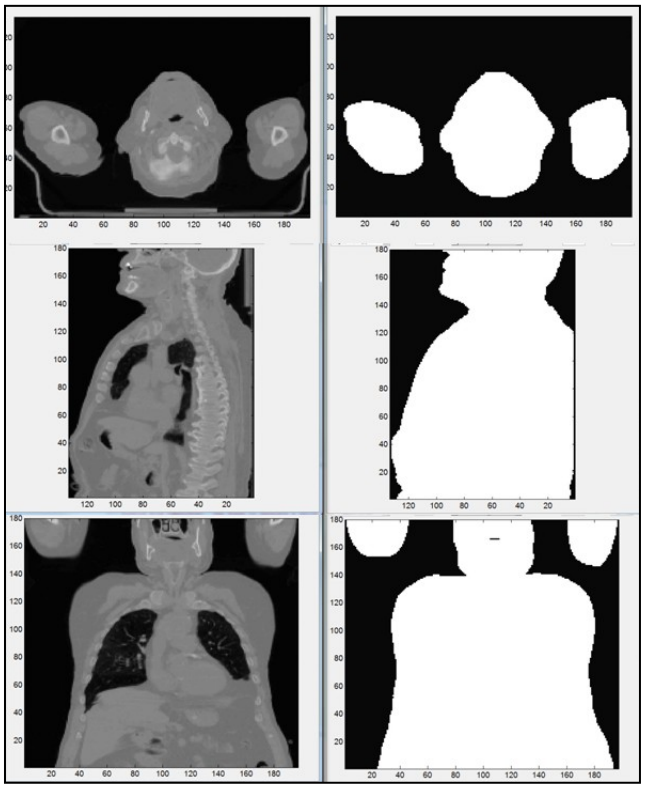

Figure 4.6 Density Matrices: Transverse, sagittal, and coronal views of the original heterogeneous (left) and MATLAB generated homogeneous (right) density matrices.

4.2.1.1 Single Beam Analysis

The dose difference maps for unmodulated fields of the $0T_{par}$ plan relative to the $0.56T_{par}$ plan and $1.5T_{par}$ plan for beam 3 on a homogeneous geometry are depicted in Figure 4.7 below. There is less than 1% difference for almost all dose voxels within the patient for both magnetic field strengths (where the % difference is with respect to 16Gy for single field comparisons). This is consistent with previous literature showing that low magnetic fields have minimal effects within homogeneous regions of a patient (56). It is worthwhile to note that the dose differences

outside the patient in this chapter should not be considered relevant, since the statistical uncertainty in these voxels is very high. This is because there are few electrons outside the patient (~0.2% of the particles in the phase spaces), and that the air outside the patient is low enough density that there are relatively few interactions compared to inside the patient.

Figure 4.8 shows the same difference maps for the heterogeneous geometry. The low density regions within the lung exhibit significant dosimetric differences even at $0.56T_{par}$. These effects are even more pronounced at $1.5T_{par}$, and in general demonstrate the confinement of scattered electrons to helical paths with constant gyroradii by the parallel magnetic field, effectively preventing them from scattering out of the beam edges within the lung. This results in a hotter (colder) dose distribution inside (outside) the projected beam edges relative to the $0T_{par}$ case.

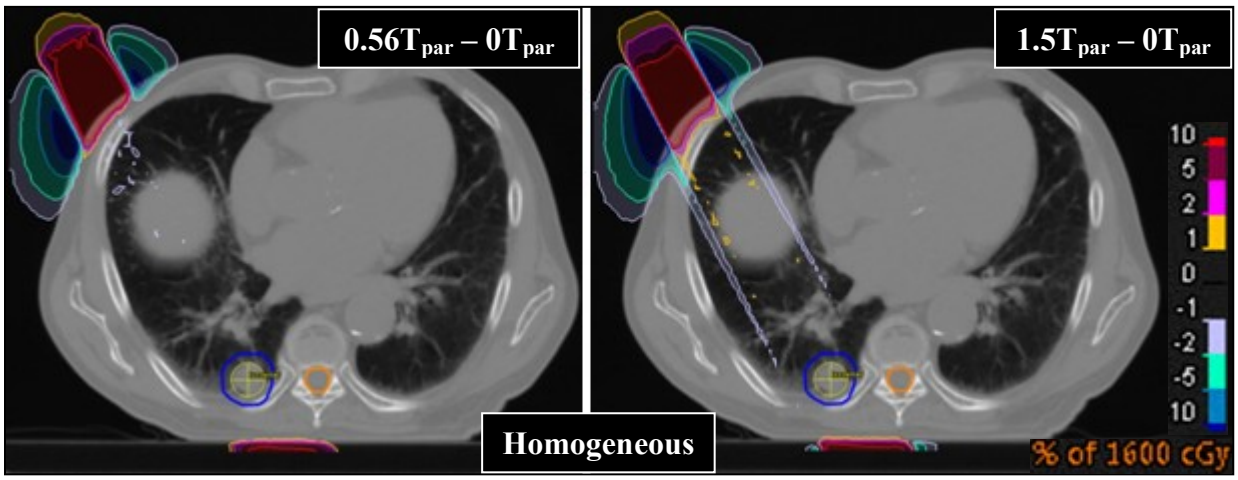

Figure 4.7 Homogeneous* patient density: Single beam (#3) difference maps for 0.56T (left) and 1.5T (right) relative to 0T. Colour bar indicates the percent difference relative to the prescription point dose of 1600cGy. *The homogeneous plan is displayed on the same CT series as the heterogeneous plan.

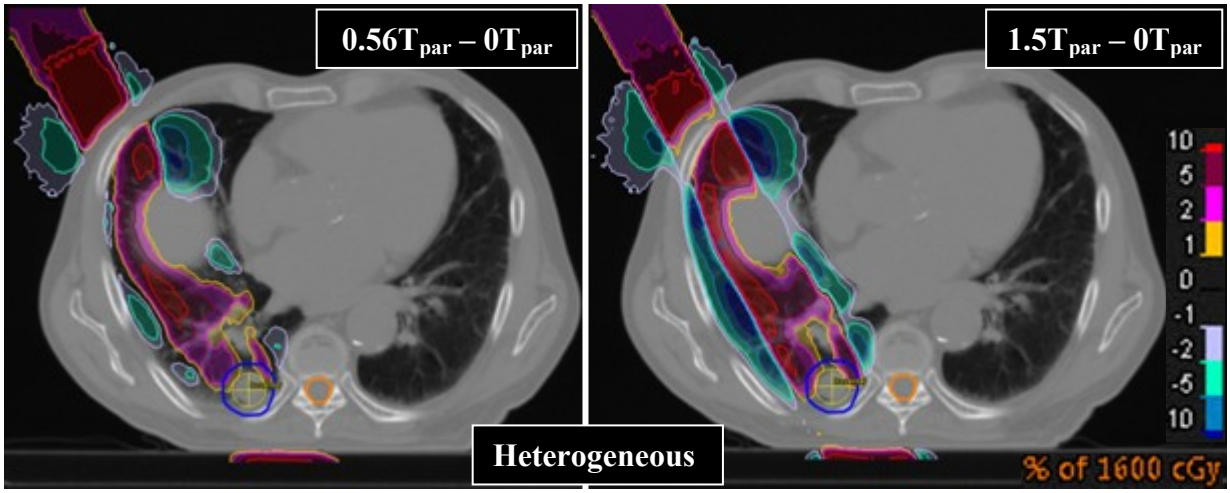

Figure 4.8 Heterogeneous patient density: Single beam (#3) difference maps for $0.56T_{par}$ (left) and $1.5T_{par}$ (right) relative to $0T_{par}$. Colour bar indicates the percent difference relative to the prescription point dose of 1600cGy.

In agreement with the dose difference maps seen above, the DVHs for beam 3 (Figure 4.9) indicate that the magnetic field effects for the homogeneous patient are negligible. The DVH curves for this patient at all magnetic field strengths overlap, indicating virtually identical dose to both the PTV and the right lung. For the heterogeneous patient, there is a small, but noticeable difference in the PTV coverage for the different magnetic field strengths. The curves for the PTV are almost parallel however, with the DVH being hotter (to the right) with increasing magnetic field strength. However, if these plans had been normalized to the same dose-volume point (*e.g.* PTV D95) there would be little difference in the PTV coverage. With increasing magnetic field strength, the right lung DVHs show some additional sparing in the lower dose region of the DVH, and increases in dose in the higher dose region. This is consistent with the dose difference maps in Figure 4.8 that show regions of hotter dose within the beam edges, and colder dose outside the beam edges as the magnetic field strength is increased.

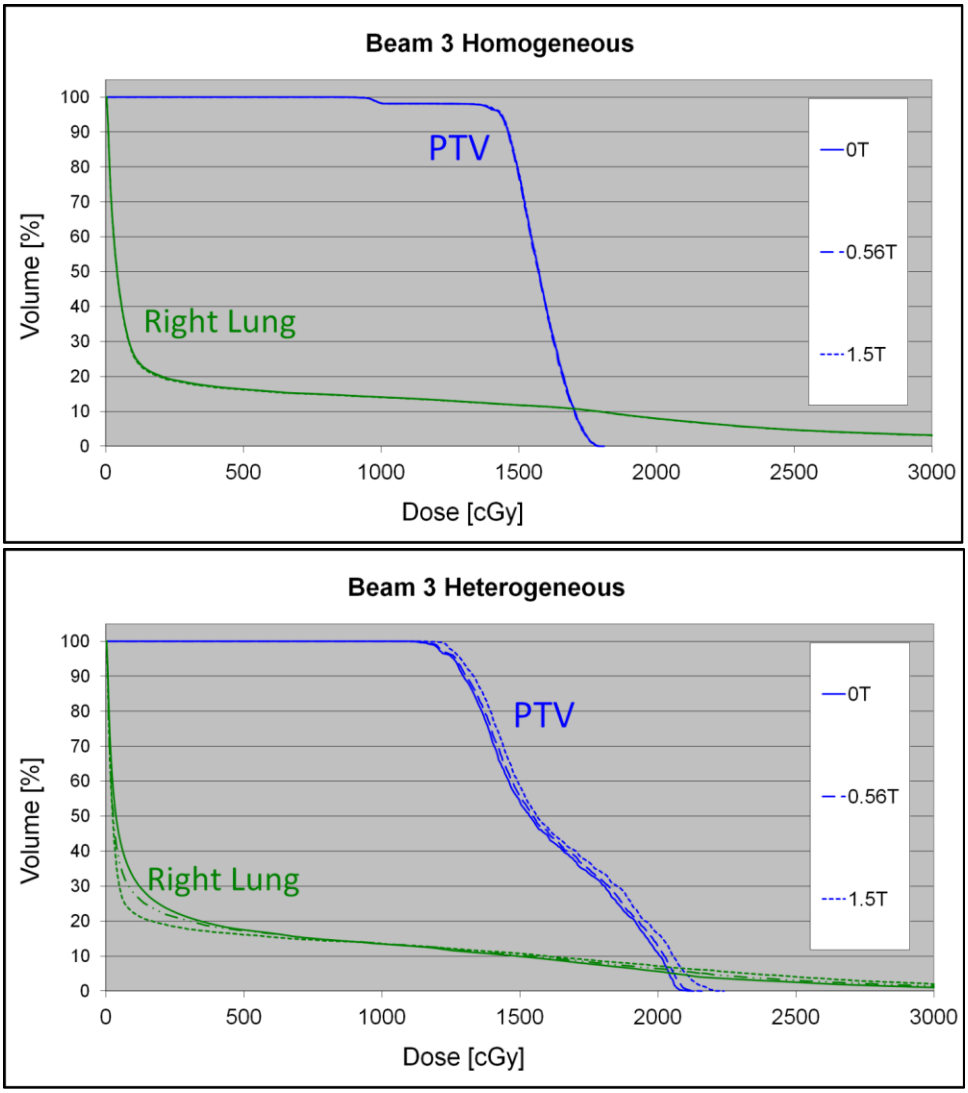

Figure 4.9 DVHs for a plan with a single unmodulated field delivered with the parallel Linac-MR configuration using homogeneous (top) and heterogeneous (bottom) patient densities. All dose distributions were normalized to deliver 1600cGy point dose to isocenter.

4.2.1.2 Plan Analysis

Results for the composite unmodulated plans are similar to the single beam plans, as evident in the dose difference maps and DVHs which were normalized to deliver 4800cGy to 95% of the PTV (Figure 4.10 homogenous / 4.11 heterogeneous). For the $0.56T_{par}/1.5T_{par}$ homogenous patient, other than a small increase in surface dose, all voxels within the patient are

less than 1% different from the $0T_{par}$ case (% difference is with respect to 4800cGy). The increase in surface dose for each beam is due to the confinement of contaminant electrons scattered in the head of the linac, which reach the surface of the patient within the beam edges rather than scattering out of the beam. Again the homogeneous DVHs for both the PTV and the right lung are practically identical for all three magnetic field strengths.

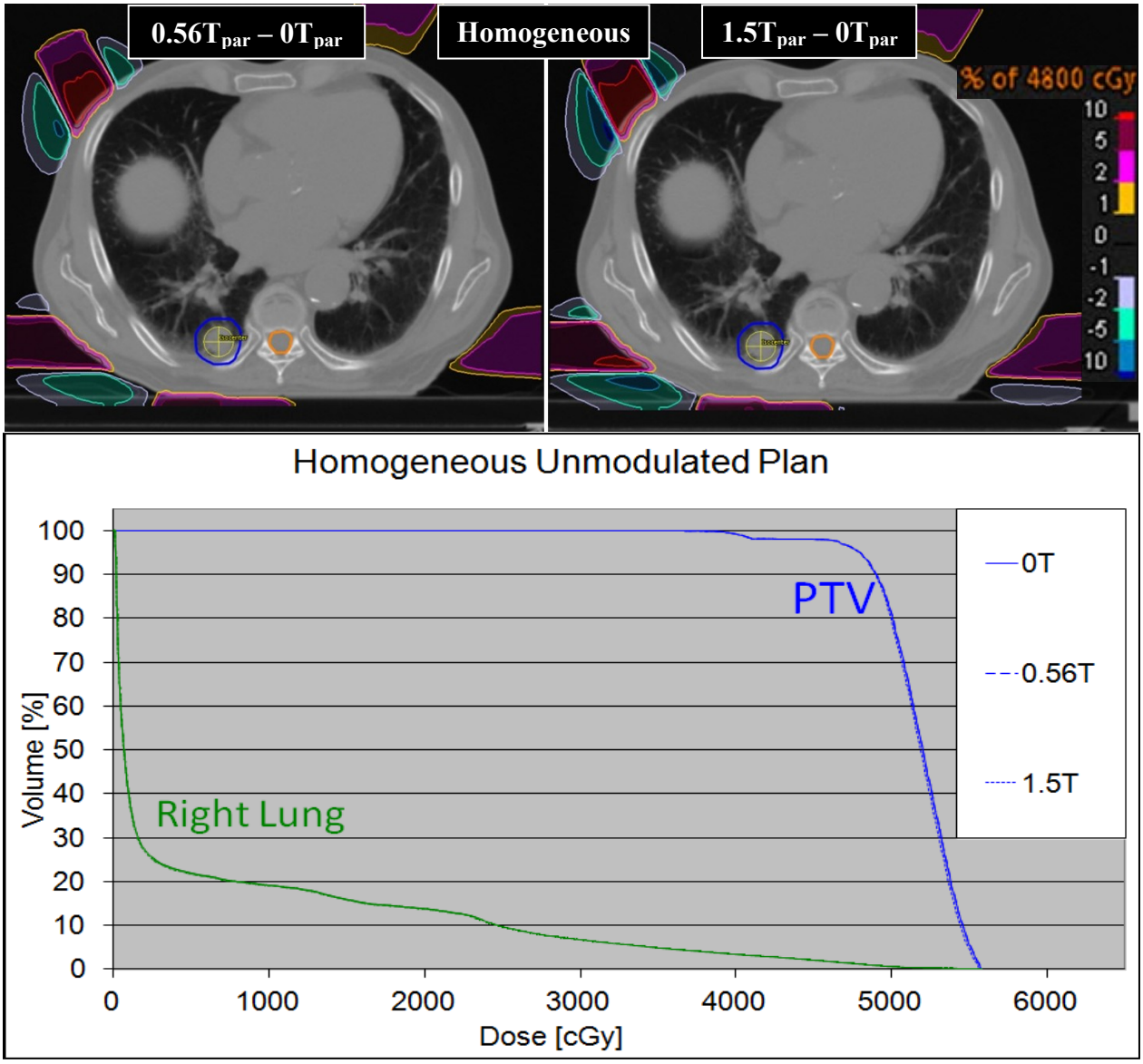

Figure 4.10 Homogeneous patient density: Composite conformal plan difference maps of $0.56T_{par}$ (left) and $1.5T_{par}$ (right) relative to $0T_{par}$. Other than a small increase in surface dose, all voxels within the patient exhibit less than a 1% difference relative to the $0T_{par}$ case. Plans were normalized to deliver 4800cGy to 95% of PTV.

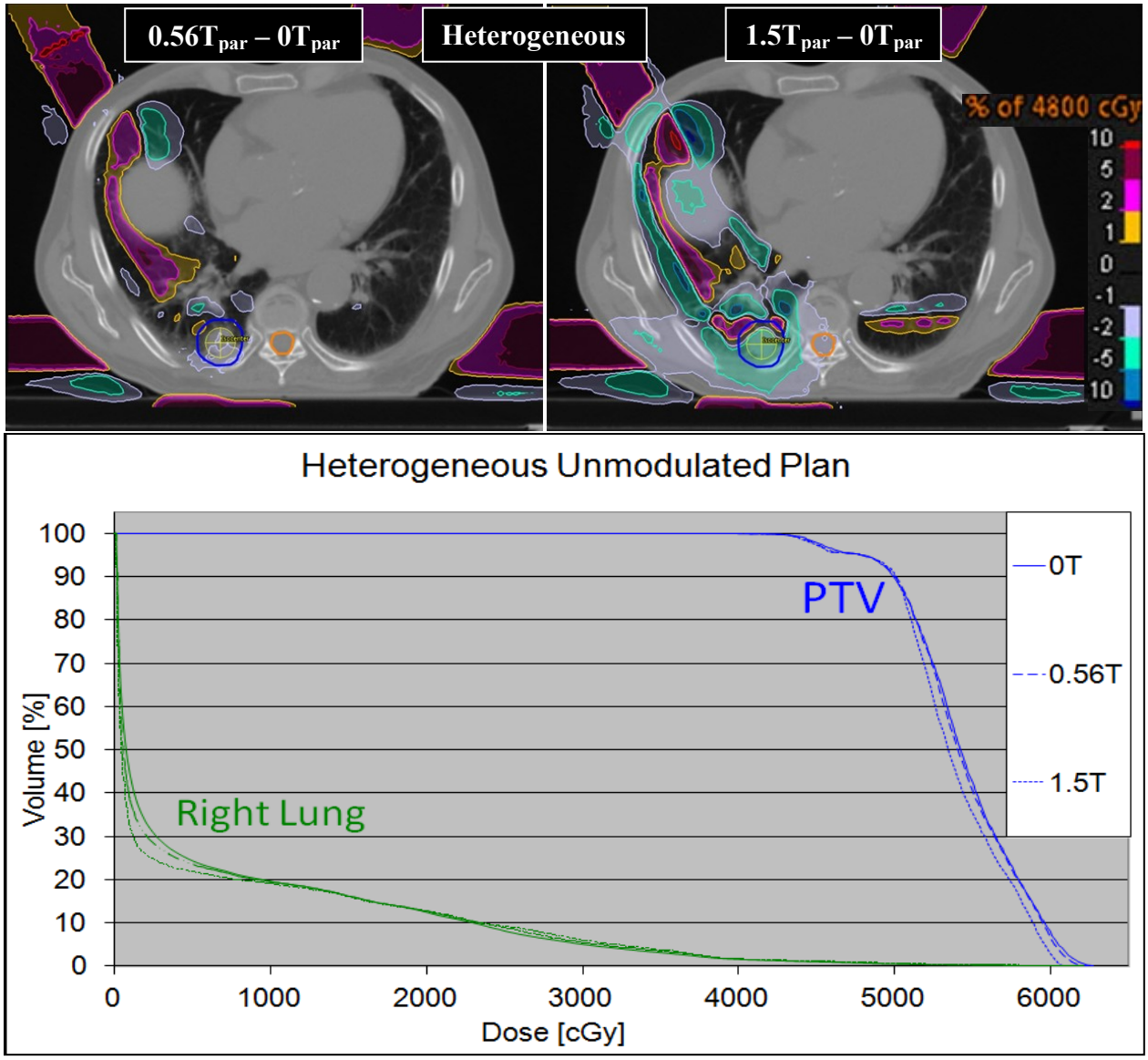

Figure 4.11 Heterogeneous patient density: Composite conformal plan difference maps of $0.56T_{par}$ (left) and $1.5T_{par}$ (right) relative to $0T_{par}$. The low density regions in the lung exhibit the largest differences, with hotter (colder) dose distributions inside (outside) the beam edges. Plans were normalized to deliver 4800cGy to 95% of PTV.

The heterogeneous patient shows the expected dosimetric effects of the parallel magnetic field, particularly in regions traversing low density lung. The PTV dose shows very little different for the $0.56T_{par}$ plan relative to $0T_{par}$; the $1.5T_{par}$ plan, however, is more than 2% colder for a large percentage of its volume. This is reflected in Figure 4.11, where the PTV DVH curve

for $1.5T_{par}$ is steeper and to the left of the other two cases. This indicates that the target coverage is more uniform, and that less dose is required for the majority of the PTV in order to achieve the prescription of 4800cGy to 95% of its volume. The PTV curve for the heterogeneous patient shows nearly identical coverage at $0T_{par}$ and $0.56T_{par}$. The DVH curves for the heterogeneous patients' right lung shows regions of hotter and colder dose to the lung, consistent with our understanding of the confinement of electrons in lung by the parallel magnetic field. The mean dose delivered to the lung is 1.2% less and 4.3% less for $0.56T_{par}$ and $1.5T_{par}$, respectively, relative to the $0T_{par}$ case (Table 4.1). This indicates that with identical unmodulated field shapes and the same target coverage, some lung sparing can be achieved as a function of increasing magnetic field strength.

B field	Heterogeneous		Homogeneous	
	Mean Lung Dose [cGy]	**Percent Difference**	**Mean Lung Dose [cGy]**	**Percent Difference**
0T par	581	N/A	600	N/A
0.56T par	574	-1.2%	600	+0.0%
1.5T par	556	-4.3%	597	-0.5%

Table 4.1 Mean lung dose for three field unmodulated plans. Percent differences are calculated relative to the $0T_{par}$ plan for the parallel Linac-MR configuration.

Another consequence of the electron confinement with the parallel magnetic field is that less MUs are required to deliver the same PTV prescription dose as magnetic field strength increases. This reduction of MUs is negligible for the homogeneous plans (<1%), but is more significant at $1.5T_{par}$ for the heterogeneous plan which requires on average greater than 3% less MUs (Table 4.2).

		$0T_{par}$	$0.56T_{par}$		$1.5T_{par}$	
Parallel	**Beam #**	**MUs**	**MUs**	**Percent Difference**	**MUS**	**Percent Difference**
Homogeneous						
	1	506.2	506.2	0.0	503.4	-0.5
	2	662.9	663.8	+0.1	659.9	-0.4
	3	991.5	992.0	0.0	985.6	-0.6
Heterogeneous						
	1	529.0	524.8	-0.8	511.6	-3.3
	2	677.3	669.8	-1.1	654.1	-3.4
	3	796.6	789.9	-0.8	769.3	-3.4

Table 4.2 MUs and percent differences relative to $0T_{par}$ for three field unmodulated plans (parallel Linac-MR configuration).

4.2.2 Perpendicular Linac-MR Configuration with Unmodulated Beams

4.2.2.1 Single Beam Analysis

A similar analysis of unmodulated plans was also done for the perpendicular Linac-MR configuration (146cm SAD): the beam 2 difference maps and the associated DVHs for homogeneous and heterogeneous patients are shown in Figures 4.12 and 4.13. For the perpendicular configuration, a transverse view is inadequate to visualize the effects of the magnetic field: according to the right hand rule, the Lorentz force sweeps electrons in the superior to inferior direction, which would be in and out of the page for a transverse view. Therefore coronal and transverse views of the patient are illustrated to properly visualize the magnetic field effects for the perpendicular configuration. Figure 4.13 shows the lateral shift in dose (towards the patient's inferior) for a homogeneous patient density, as well as an increase in exit dose at a tissue-air interface resulting from the electron return effect (ERE). The magnitude of these effects increase with increasing magnetic field strength, with streaks ranging between ±5% difference at either beam edge for the ($0.56T_{perp} - 0T_{perp}$) difference map, and streaks with differences as large as ±10% for the ($1.5T_{perp} - 0T_{perp}$) case. Nevertheless, inside the field edges, the vast majority of the right lung and PTV voxels in these sagittal (left) and coronal (right) slices exhibit less than 1% difference. Overall, target coverage and lung dose for all three magnetic field strengths is nearly identical for the homogeneous patient, as indicated by the DVH curves in Figure 4.12, which overlap nearly everywhere for all three field strengths.

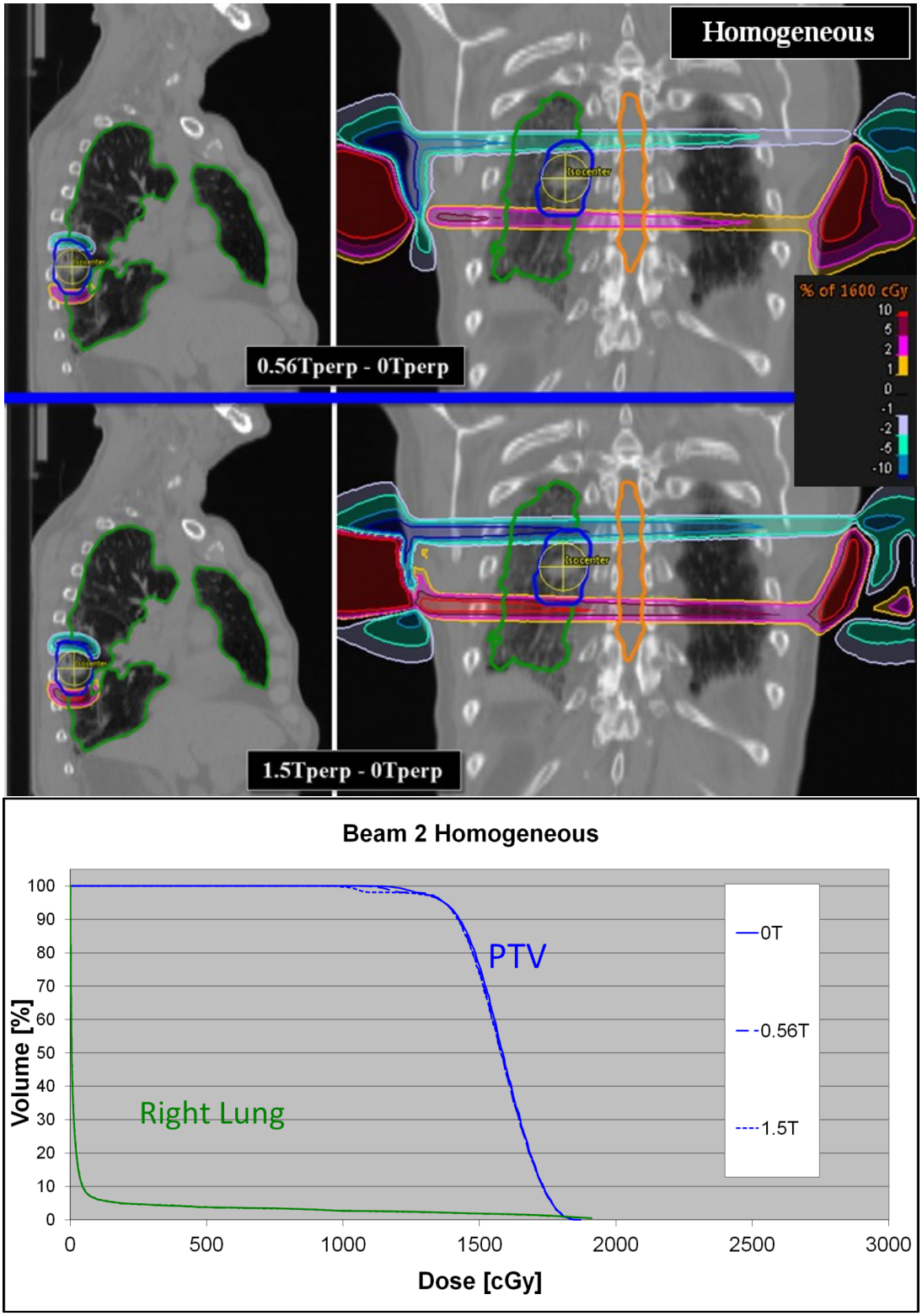

Figure 4.12 Homogeneous patient density: Beam 2 conformal plan difference maps of $0.56T_{perp}$ (top) and $1.5T_{perp}$ (middle) relative to $0T_{perp}$. DVHs for all three magnetic field strengths (bottom). Plans were normalized to deliver 1600cGy point dose to isocenter.

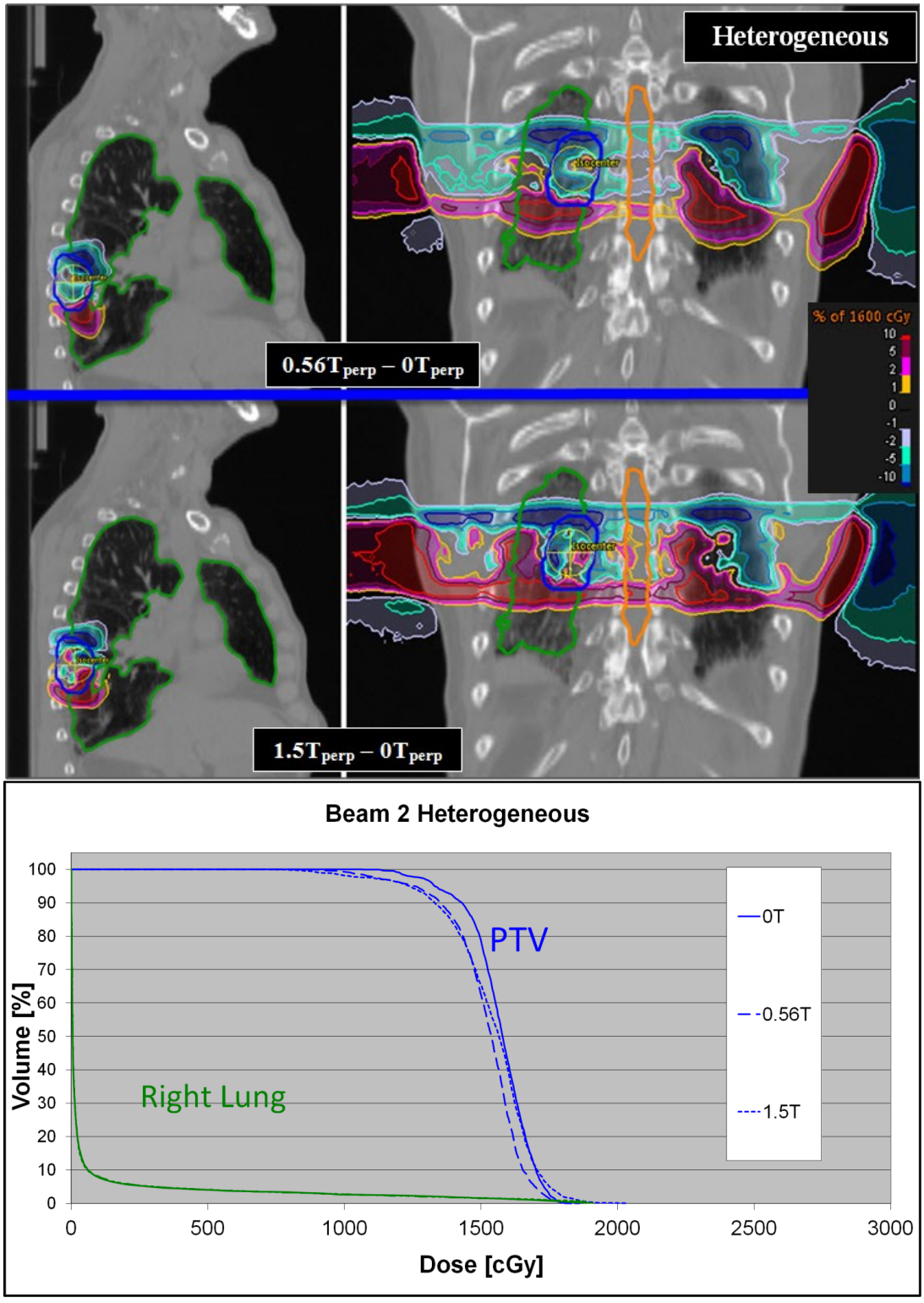

Figure 4.13 Heterogeneous patient density: Beam 2 conformal plan difference maps of $0.56T_{perp}$ (top) and $1.5T_{perp}$ (middle) relative to $0T_{perp}$. DVHs for all three magnetic field strengths (bottom). Plans were normalized to deliver 1600cGy point dose to isocenter.

The heterogeneous patient again exhibits much larger dosimetric differences than the homogenous patient, particularly in the lung, where the density is significantly different than water. The perpendicular magnetic field causes scattered electrons to be swept off target towards the patient's inferior. This is seen in Figure 4.13 which shows much larger hot and cold spots than the homogeneous case in all low density areas traversed by, or adjacent to the beam path. These differences exceed ±10% in many places inside the lung, and also affect the PTV coverage much more significantly than in the homogeneous case. For both magnetic field strengths there is a large portion of the PTV that is underdosed, with a smaller region receiving more dose than the $0T_{perp}$ case after being normalized to the same isocenter point dose (Figure 4.13). Consistent with this, the heterogeneous patient's DVH curves for the PTV in Figure 4.13 show that the majority of the PTV receives less dose relative to the $0T_{perp}$ case as magnetic field strength increases, with a very small volume receiving increased dose. Somewhat surprising is that the DVH curves for the right lung overlap at all three magnetic field strengths for each of the homogeneous and heterogeneous cases, despite the large visual differences in the dose distributions. However, since the shift in dose is symmetric both geometrically and in magnitude, effectively, dose is generally being shifted from one part of lung to another; this results in an insignificant change from a dose volume perspective. It is worth noting that if the plans had been normalized to the PTV D95 point (like the subsequent composite plans are), that the $0.56T_{perp}$/$1.5T_{perp}$ DVH curves for the heterogeneous PTV would lie to the right of the $0T_{perp}$ case, indicating that more dose would be delivered to the majority of the PTV. This is because with identical beam shapes, more MUs would be required to make up for the particles lost on the superior side of the beam due to Lorentz forces.

4.2.2.2 Plan Analysis

The analysis for the perpendicular configuration composite plans is depicted in the dose difference maps and DVHs shown in Figures 4.14 (homogeneous patient density) and 4.15 (heterogeneous). For the homogeneous patient at $0.56T_{perp,}$ the majority of voxels within the PTV exhibit differences of less than 1% relative to the $0T_{perp}$ case. Similar to the single beam case, the hot and cold streaks on the inferior and superior sides of the patient have very little effect on the DVH for the PTV at $0.56T_{perp}$, which overlaps with the $0T_{perp}$ curve. The magnetic field effects are more significant at $1.5T_{perp}$, where other than the small cold spot on the superior side of the target volume, the majority of the PTV is receiving at least 2% more dose than the $0T_{perp}$ case. This is reflected in Figure 4.18 where the $1.5T_{perp}$ PTV curve lies consistently to the right of the $0T_{perp}$ curve, with a D50 difference of +2.7%. To achieve this increase in dose, more MUs were required (Table 4.3): the $1.5T_{perp}$ plan required an average of about 3.2% more MU's for each beam after being normalized to the same dose of 4800cGy to 95% of the PTV.

		$0T_{perp}$	$0.56T_{perp}$		$1.5T_{perp}$	
Perpendicular	**Beam #**	**MUs**	**MUs**	**Percent Difference**	**MUS**	**Percent Difference**
Homogeneous						
	1	512.54	513.76	+0.2	528.75	+3.2
	2	673.44	674.61	+0.2	695.07	+3.2
	3	1006.86	1010.88	+0.4	1039.82	+3.3
Heterogeneous						
	1	529.98	540.68	+2.0	545.67	+3.0
	2	678.49	690.66	+1.8	714.26	+5.3
	3	800.14	802.09	+0.2	820.6	+2.6

Table 4.3 Perpendicular Linac-MR configuration MUs and percent differences relative to $0T_{perp}$ for unmodulated plans after normalizing dose distributions to deliver 4800cGy to 95% of PTV.

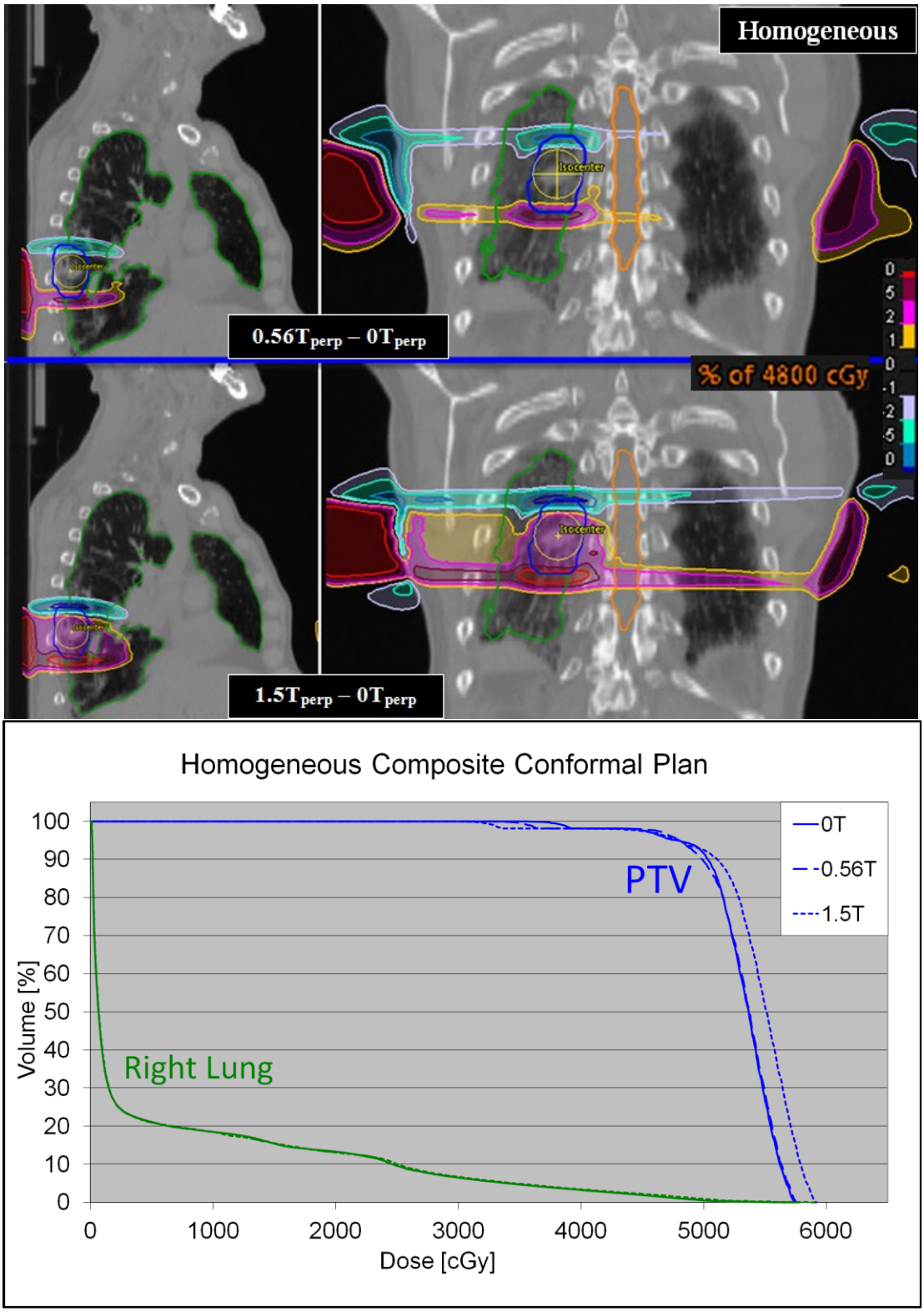

Figure 4.14 Homogeneous patient density: Three field unmodulated plan difference maps relative to $0T_{perp}$ (top and middle). DVHs for all three magnetic field strengths (bottom). Plans were normalized to deliver 4800cGy to 95% of PTV.

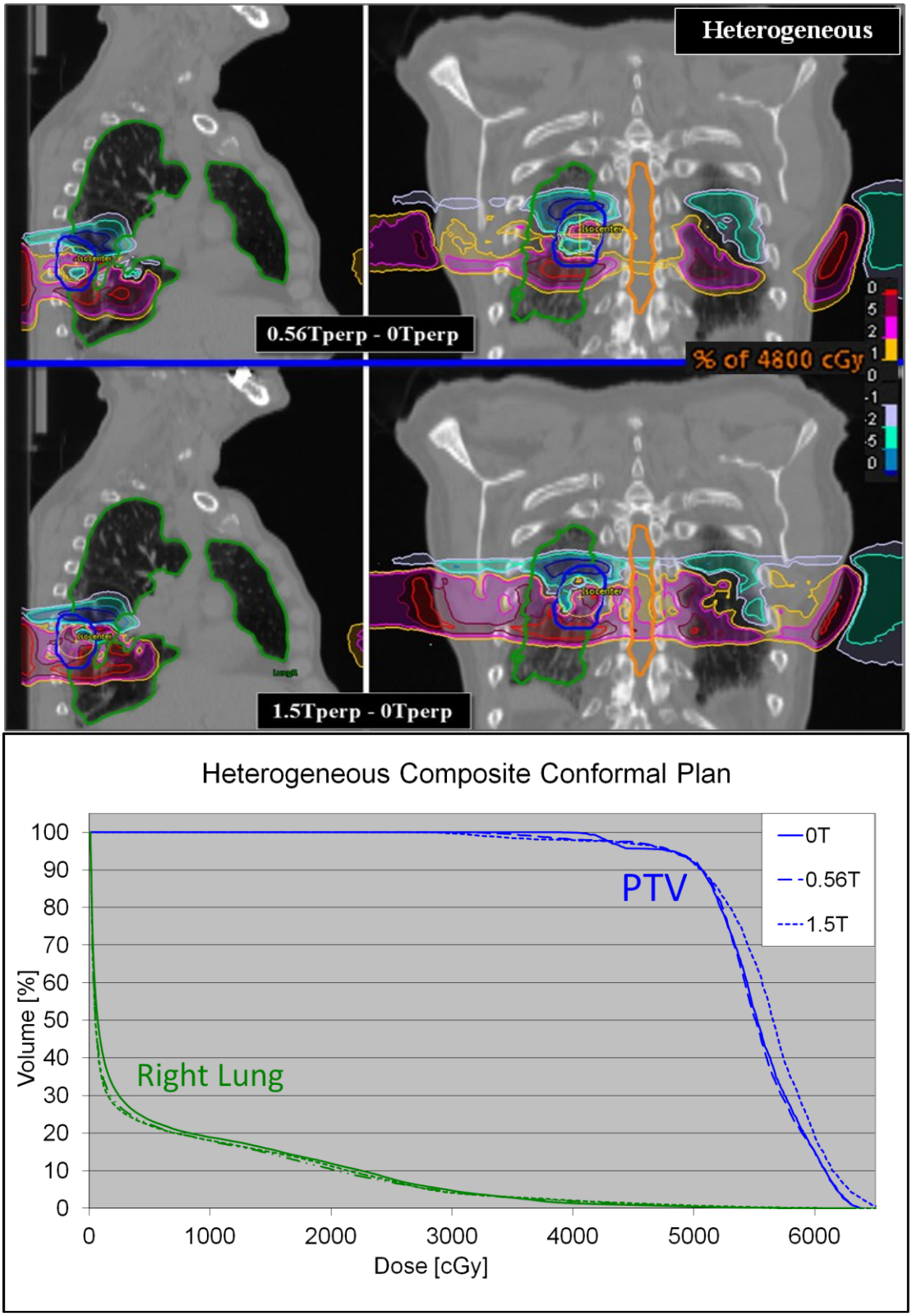

Figure 4.15 Heterogeneous patient density: Three field unmodulated plan difference maps relative to $0T_{perp}$ (top and middle). DVHs for all three magnetic field strengths (bottom). Plans were normalized to deliver 4800cGy to 95% of PTV.

Dosimetric differences are much more significant for the heterogeneous patient. The dose difference maps in Figure 4.15 show many more voxels with differences greater than ±10% than the homogeneous case, particularly the low density voxels inside the lungs. There are significant differences throughout the PTV even at $0.56T_{perp}$, as opposed to just on the superior and inferior beam edges for the homogeneous case. At $0.56T_{perp}$ the DVH in Figure 4.15 suggests that the hot and cold spots balance each other out from a dose volume perspective for the PTV, as the DVH curve overlaps with the $0T_{perp}$ case. At $1.5T_{perp}$, there is a net increase in PTV dose, whose DVH curve lies to the right of the $0T_{perp}$ case. The difference between the $0T_{perp}$ and $1.5T_{perp}$ curves is fairly consistent, and at D50 is +2.4%. The DVH curve for the right lung shows some small lung sparing due to the perpendicular magnetic fields, which is also reflected in the mean lung dose metric (Table 4.4 below). However, unlike the parallel configuration, this lung sparing comes at the cost of worse PTV coverage relative to the 0T case. In the parallel case, the confinement of contaminant electrons results in some lung sparing and an improvement in PTV uniformity. The lateral Lorentz force on electrons in the perpendicular case actually decreases the target uniformity. This phenomenon also affects the number of MUs required to deliver the same prescription dose to the PTV, as shown in Table 4.3. Unlike the parallel configuration, where fewer MUs were required as magnetic field strength increases (for the same target coverage), the trend for the perpendicular configuration is to require more MUs after normalization to achieve the prescription of 4800cGy to 95% of the PTV. This is because the lateral shift of electrons causes dose deposition to miss the target in some places, underdosing one side, which manifests as a colder spot in the DVH.

B field	Heterogeneous		Homogeneous	
	Mean Lung Dose [cGy]	**Percent Difference**	**Mean Lung Dose [cGy]**	**Percent Difference**
0T perp	561	N/A	587	N/A
0.56T perp	521	-7.1%	582	-0.9%
1.5T perp	531	-5.3%	591	+0.7%

Table 4.4 Mean lung dose for three field unmodulated plans for the perpendicular Linac-MR configuration. Percent differences are calculated relative to the 0T plan.

Overall our unmodulated plan analysis suggests that the tissue heterogeneities of the lung could impact treatment plan optimization for Linac-MR systems. This was the basis of our choice of patient and tumour location. Since differences caused by the magnetic field for the homogeneous patient were generally small, only the heterogeneous patient is considered in the remaining analysis (Sections 4.3 and 4.4). The unmodulated plan results further suggest that incorporating magnetic field modeling during optimization may be more important at higher field strengths and for the perpendicular configuration. For the parallel configuration, ignoring the magnetic field during optimization would result in a slight over- (under-) estimate of the dose outside (inside) the field edges, but the dose deposition would remain aligned with the target. For the perpendicular case, however, ignoring the magnetic field could result in missing part of the target. In radiotherapy underdosing any part the target is generally much less desirable than delivering slightly more than prescribed dose (especially for SBRT treatments).

4.3 Impact of Magnetic Fields on Optimized Fluences

The analysis of optimized fluences will give a good indication of the importance of modeling the magnetic field at 0.56T and 1.5T. The larger the fluence differences compared to 0T, the greater the effect of not modeling the magnetic field during optimization on the resulting dose distributions at 0.56T/1.5T. The beam edges traversing the most low density lung tissue should be most affected by the magnetic field. Figure 4.16 below shows the transverse anatomy of the patient relative to each beam's path in a view looking down from the head of the patient. The spinal cord is shown as an orange 3-dimensional object coming out of the page, and the PTV is in blue. Beam 1 passes through almost no lung tissue before it hits the target, other than a small amount on the Y2 jaw side of the field. Beam 2 passes through more lung before it hits the target than beam 1, especially on the Y2 side. All beams traverse more low density lung tissue on the X1 jaw side, towards the patient superior (not visible in the Figure since superior = out of page). Therefore we will likely see the most drastic magnetic field effects on the Y2/X1 sides of the fluence distributions for beams 1&2. Beam 3 traverses more *high density* tissue on the Y2 side of the beam as it travels through the lung, suggesting that the Y1 side will be the most affected by the magnetic field. For easy reference, Table 4.5 below tabulates the sides of each beam that pass through the most lung tissue, and thus are expected to be most affected by the magnetic field. Keeping these relations between the collimators, patient anatomy, and optimization objectives in mind will be important in the subsequent analysis of the optimized fluences.

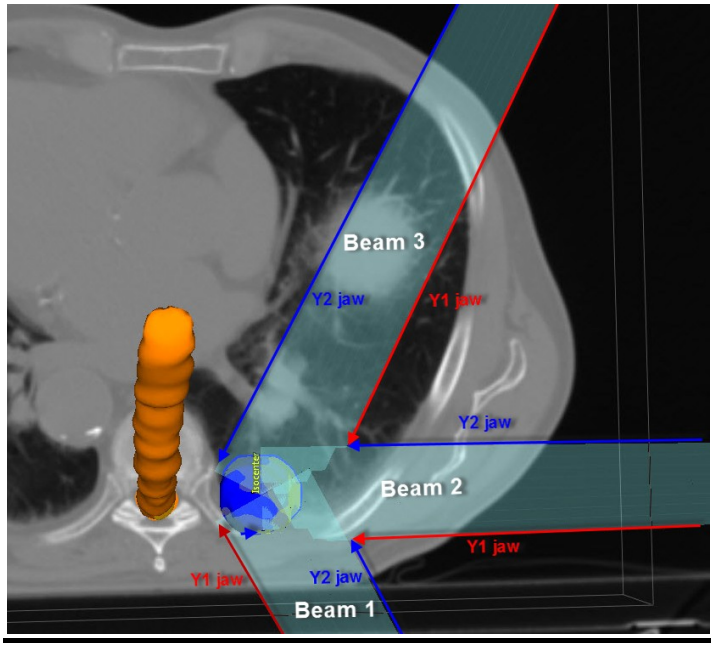

Figure 4.16 Collimator jaws relative to patient anatomy in a transverse view. PTV is in blue, the spinal cord is in orange. (Note that there is a 270 degree collimator angle on this plan, and that this is a view looking down from the head of the patient, whereas all other transverse slices in this document look from the feet of the patient).

	Sides of beam traversing most lung tissue	
Beam #	**Collimators**	**Fluence Map**
1	Y2/X1	Top/Left
2	Y2/X1	Top/Left
3	Y1/X1	Bottom/Left

Table 4.5 Portions of beams traversing the most low density tissue, and hence most affected by the magnetic field. All beams pass through more lung tissue on the superior (X1) side of the field.

4.3.1 Parallel Configuration Optimized Fluences

For the parallel Linac-MR configuration, Figure 4.17 shows the percent difference histograms for all three beams for $0.56T_{par}$ (top) and $1.5T_{par}$ (bottom). The optimization shifts fluence out of beam 1 and into beam 3, whose histogram distributions are skewed towards negative and positive values respectively. It seems the optimizer may have found a dosimetric

advantage to delivering fluence through the beam which benefited the most from the electron confinement (beam 3 benefits the most since it passes through the most lung). The average percent differences at [0.56T $_{par}$, 1.5T $_{par}$] relative to 0T$_{par}$ are [-1.0% , -4.9%] for beam 1, and [+1.3% , +4.9%] for beam 3.

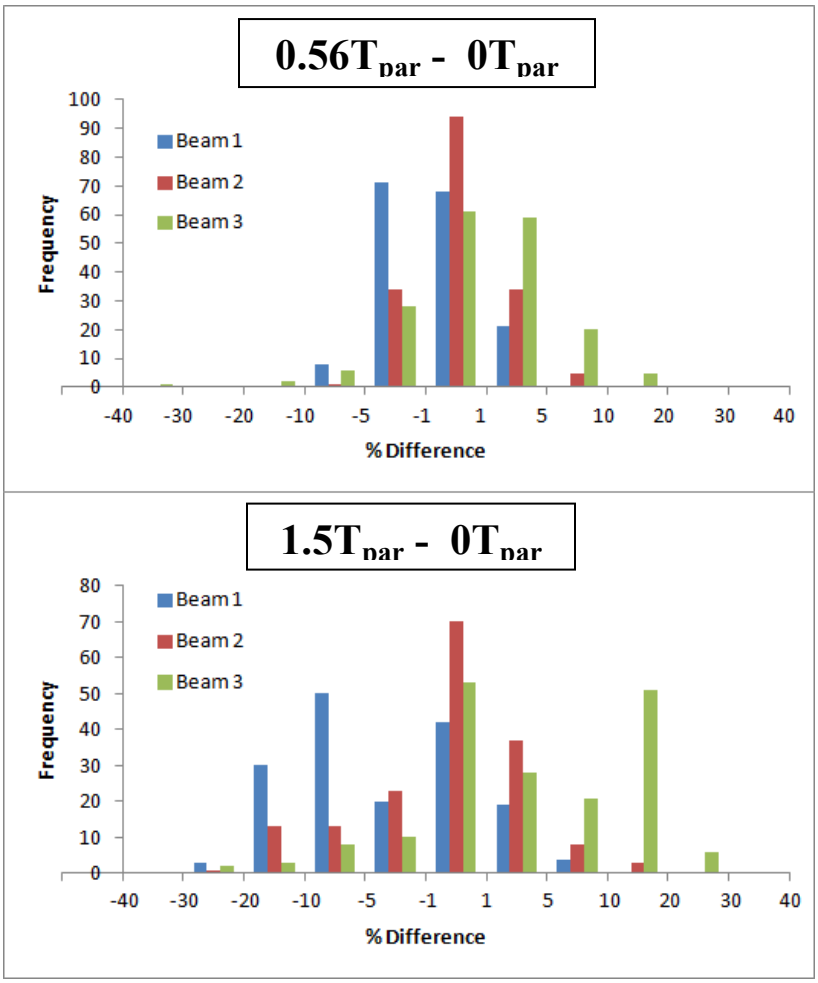

Figure 4.17 Fluence global percent difference histograms (parallel configuration)

Figures 4.18-4.20 show the optimized fluences for each beam at all three magnetic field strengths on top, with the global percent difference maps relative to 0T$_{par}$ on the bottom. In general the differences between the 0.56T$_{par}$ and 0T$_{par}$ optimized fluences are relatively small, with the majority of elements between ±5% for all three beams. The difference in the optimized

fluences also increases as a function of the amount of lung traversed, with beams 1/2/3 passing through low/medium/high amounts of lung respectively. This makes intuitive sense, as the longer the mean free path of ionized/scattered electrons, the more influence the magnetic field will have, and hence the greater the effect on the optimized fluence for that beam. The differences at $1.5T_{par}$ are much more pronounced than at $0.56T_{par}$, with percent differences as large as ±30% at the extremes. Looking at the changes in fluence for each beam (and their relation to the patient's anatomy), Figure 4.18 for beam 1 shows a reduction in fluence within the central portion of the beam, with a small increase in fluence around the edges. This effect is much more significant at $1.5T_{par}$, particularly on the Y2 (top) and X1 (left) sides of the field, the sides passing through lung near the PTV (Table 4.4).

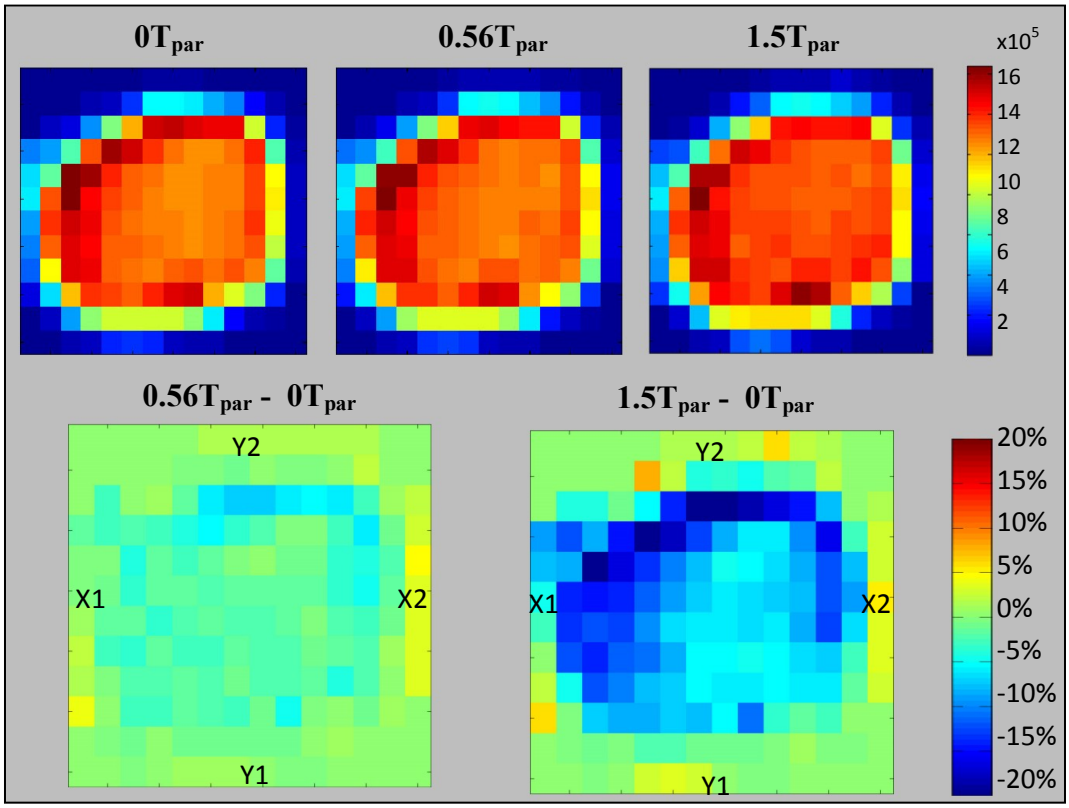

Figure 4.18 Beam 1 (parallel configuration): Fluences (top) and global percent difference (bottom)

Beam 2 in Figure 4.19 is colder on the Y2 (top) side of the field, and hotter on the Y1 (bottom) side. Since the Y2 side is the one passing through the most low density tissue, less fluence is required here than in the $0T_{par}$ plan to deliver the same target coverage because electrons are prevented from scattering out of the beam edges. The increase in fluence on the opposite (Y1) side is most likely to maintain target uniformity, which was one of our optimization objectives (in the form of Max/Min DVH doses to the PTV and ITV).

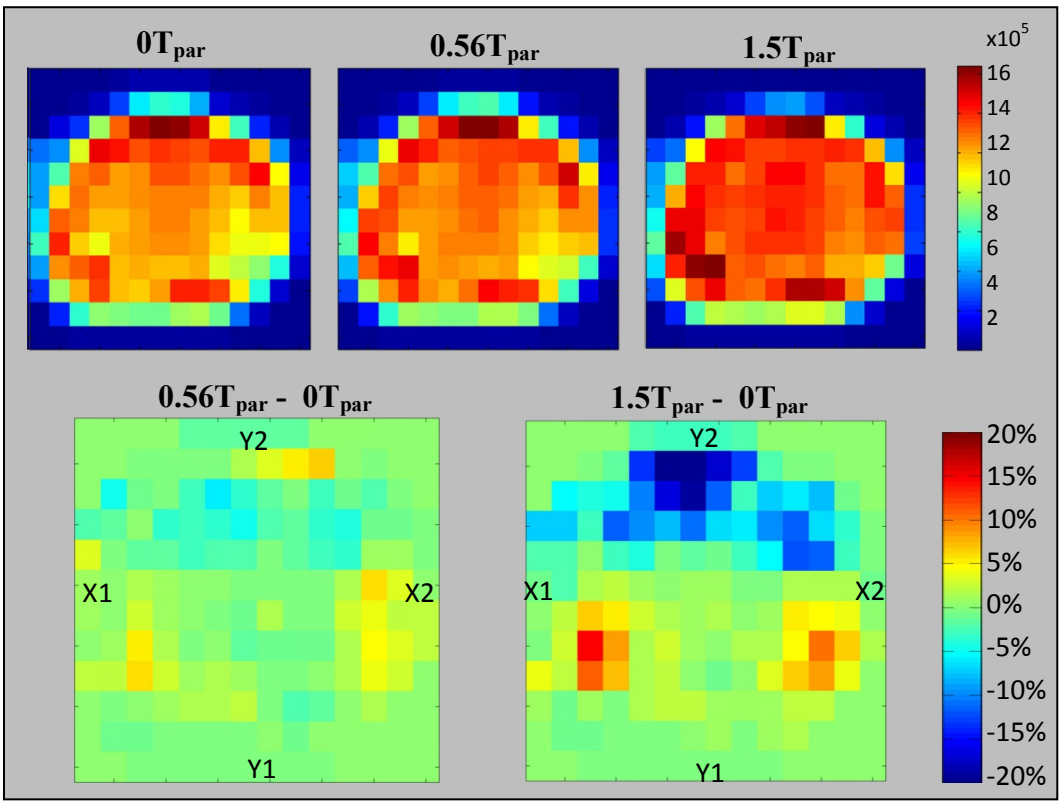

Figure 4.19 Beam 2 (parallel configuration): Fluences (top) and global percent difference (bottom)

Beam 3 traverses the most lung, and hence exhibits the largest differences of the three beams relative to the $0T_{par}$ case (Figure 4.20). As already mentioned, the fluence through beam 3 increases in conjunction with a reduction in fluence from beam 1, and is the most significant at $1.5T_{par}$ where some bixel fluences are more than 20% hotter. This increase is skewed towards the

X1/Y1 (bottom/left) side of the field, which again are the sides which travel the furthest in lung. This is another indication that the optimizer found a dosimetric advantage to sending fluence through regions which benefited the most from the electron confinement.

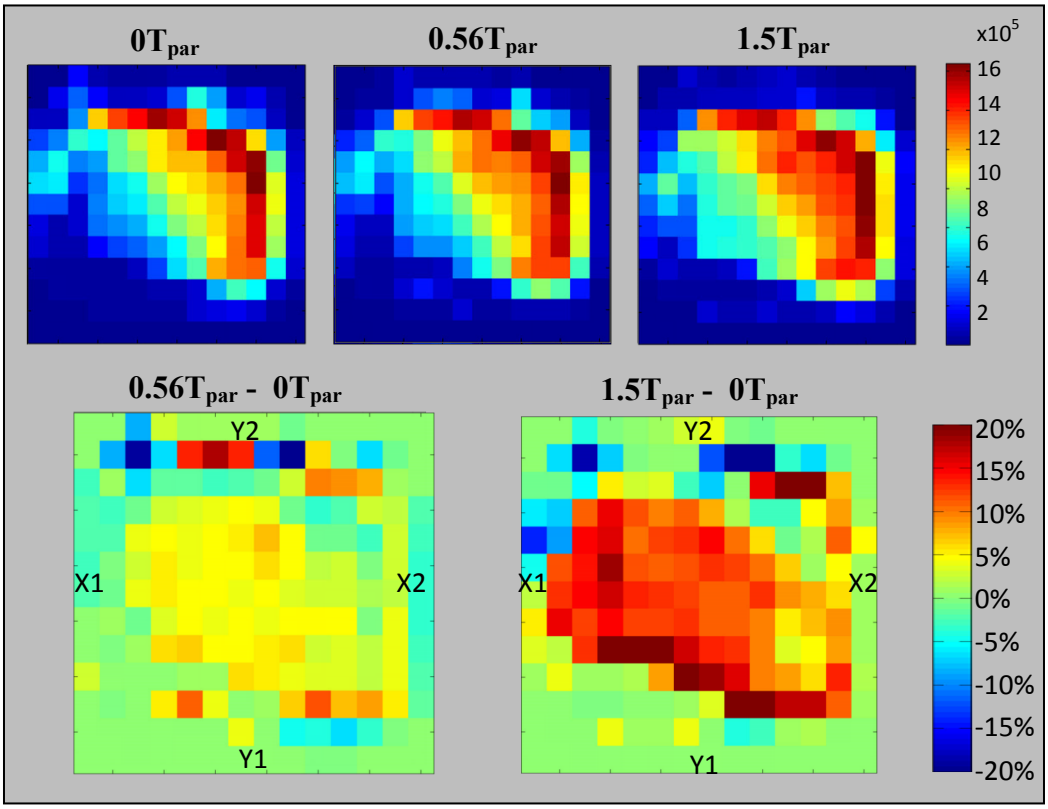

Figure 4.20 Beam 3 (parallel configuration): Fluences (top) and global percent difference (bottom)

The results indicate that modeling the magnetic field during the optimization is much more important at 1.5T than at 0.56T. Further, if the magnetic field were not modeled during optimization, the associated error would be most significant for beam 3 which traverses the most lung, which is consistent with our prediction from the unmodulated plan analysis in Section 4.2.

4.3.2 Perpendicular Configuration Optimized Fluences

The magnetic field in the perpendicular configuration is oriented towards the Y1 collimator for all 3 beams. This means for electrons travelling along the beams' central axis, the Lorentz force will curve particles towards the X2 collimator (patient inferior), which is the right side of the fluence distributions in Figures 4.21, 4.22, and 4.23. From an optimization perspective, we would predict that the optimizer would increase the fluence on the opposite (X1/left) side of the field in order to make up for the particles being swept in the X2 direction. This prediction holds true for all three beams, which generally show hotter fluence on the X1/left side of the fluence distributions relative to the 0T case. This increase in fluence is also the most pronounced in parts of the beam that travel through the most low density lung tissue, which is the Y2/X1 (top/left) side for beams 1 and 2, and the Y1/X1 (bottom/left) side for beam 3 (Table 4.4). Where there are large increases in fluence on one side of any given beam, there is a matching decrease in fluence on the opposite side of the beam in general. This is the optimizer's attempt at reestablishing dose uniformity on the target, since there are electrons being swept towards that side of the beam by the perpendicular magnetic field. As in the parallel configuration, the fluence differences are much larger at 1.5T then at 0.56T.

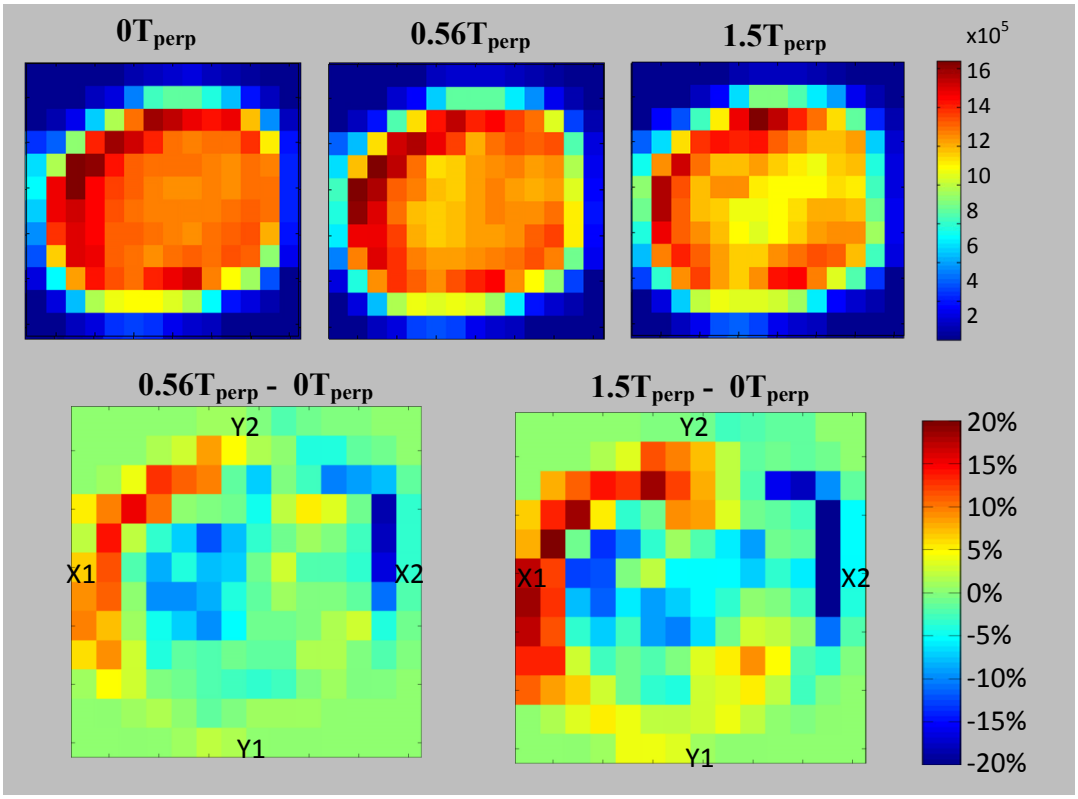

Figure 4.21 Beam 1 Fluence and global percent difference (perpendicular configuration)

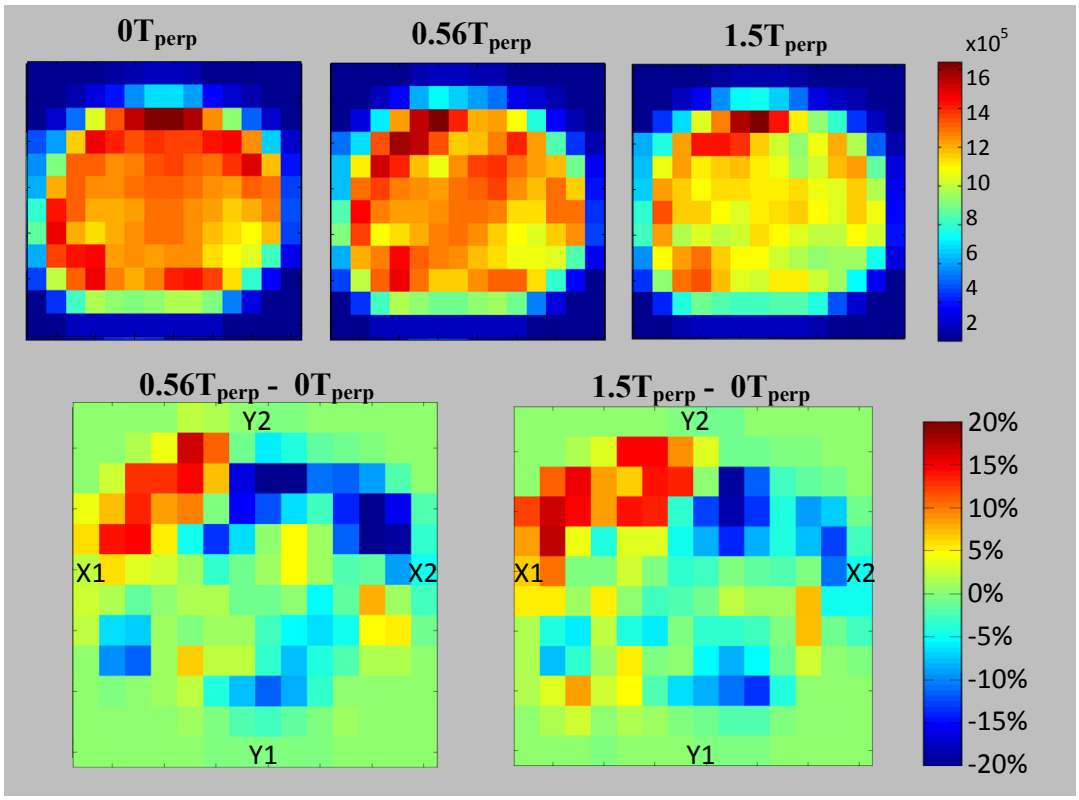

Figure 4.22 Beam 2 Fluence and global percent difference (perpendicular configuration)

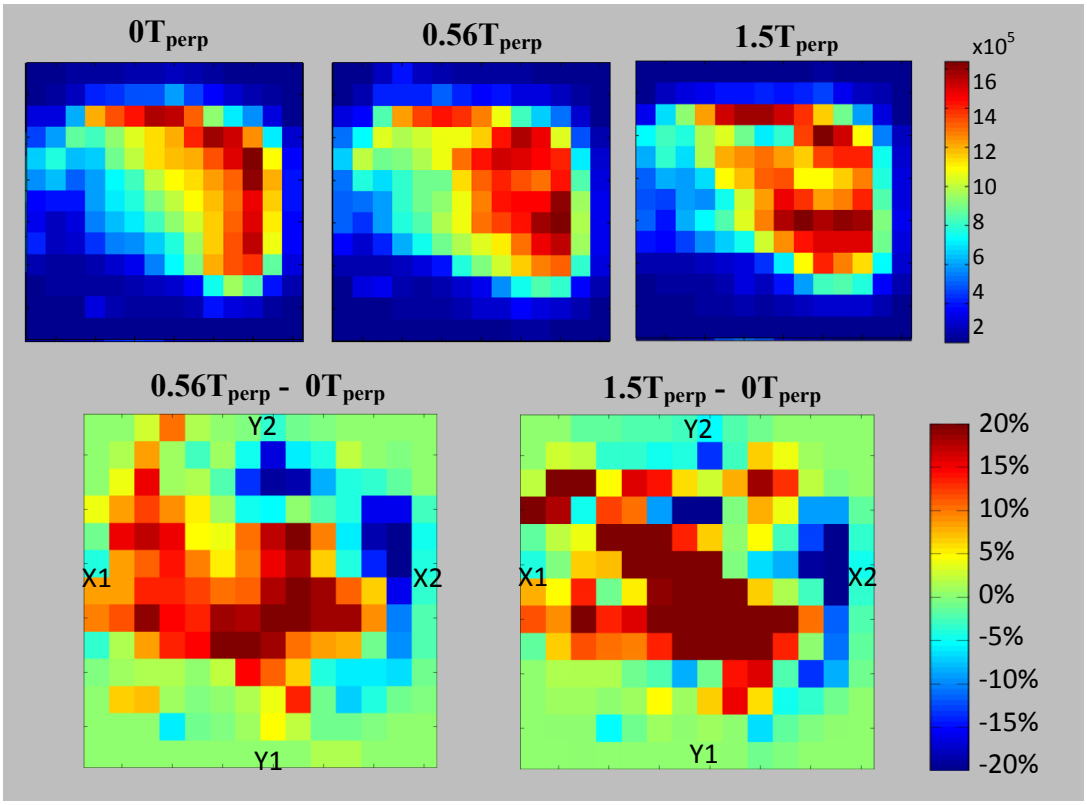

Figure 4.23 Beam 3 Fluence and global percent difference (perpendicular configuration)

These conclusions can be seen more quantitatively for each beam in the histograms in Figure 4.24. Beam 3 exhibits the largest fluence differences at both magnetic field strengths, and is skewed towards positive values, with average percent differences of +2.8% and +4.1% at 0.56T and 1.5T respectively. This increase compensates for the loss of particles being swept off course by the perpendicular magnetic field. In general the magnitude of the fluence differences for the perpendicular configuration are larger than for the parallel case. Percent differences range from ±30% at $0.56T_{perp}$, and increase to differences as high as 50% for beam 3 at $1.5T_{perp}$. We therefore predict that modeling the magnetic field is even more important for the perpendicular configuration than the parallel, and failure to do so may result in more severe plan degradation.

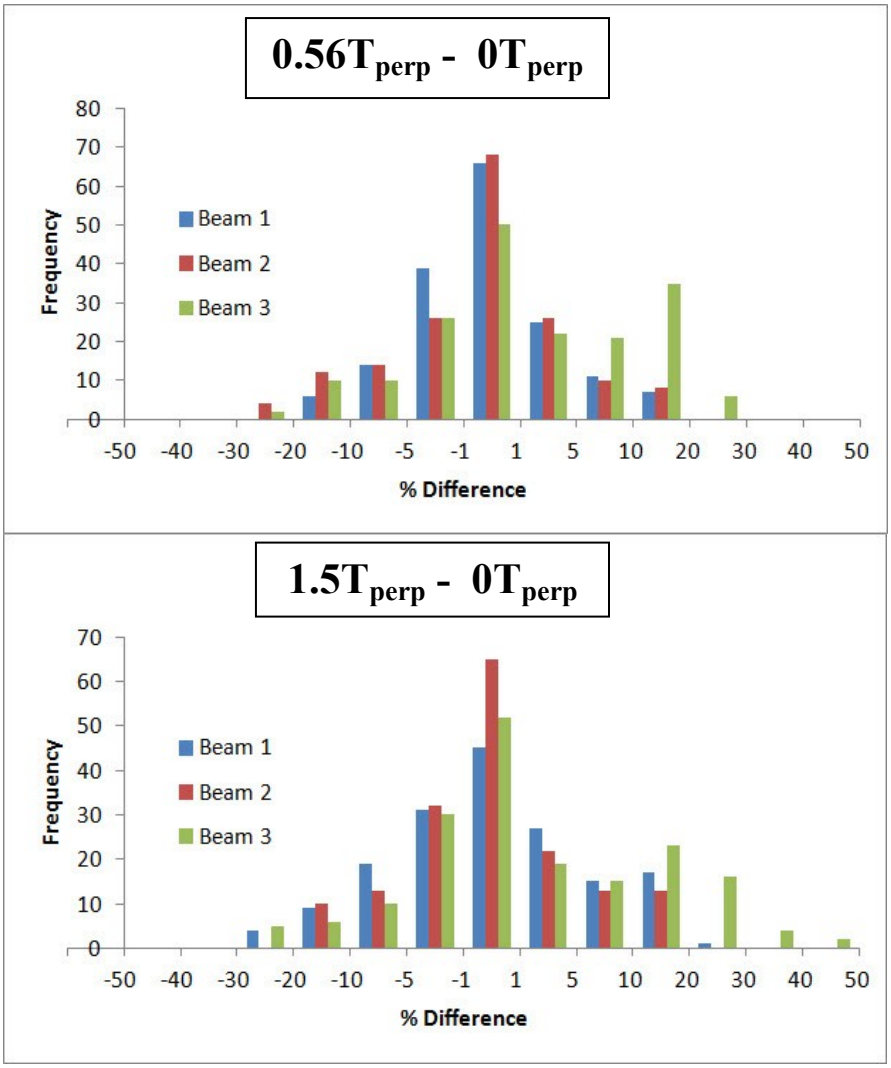

Figure 4.24 Fluence Global Percent Difference Histograms (Perpendicular Configuration)

4.4 Impact of Magnetic Fields on Optimized dose distributions

The optimized fluences from section 4.3 were used in forward dose calculations to quantify the importance of modeling the magnetic field at the fluence optimization and forward calculation stages of the inverse planning process. We consider the three cases described in Chapter 3:

Case #1: dose distributions representative of when the magnetic field is not modeled at any stage of the treatment planning process;

Case #2: dose distributions representative of when the magnetic field is not modeled during the fluence optimization, but is modeled during the during forward calculation;

Case #3: dose distributions representative of when the magnetic field is modeled during both the fluence optimization and forward calculation;

For Case #1, the dose that actually would be delivered at 0.56T and 1.5T when the magnetic field is completely ignored during the treatment planning process, will be determined by using the 0.56T and 1.5T beamlets in forward calculations with the 0T optimized fluence. By renormalizing these dose distributions from case #1 such that the prescription of 4800cGy to 95% of the PTV is met, we can evaluate the impact of only incorporating the magnetic field during the final forward dose calculation (Case #2). Essentially, the only difference between the dose distributions in cases #1 and #2 is the number of MUs, since they both use the 0T optimized fluence. Finally, by using the 0.56T and 1.5T optimized fluences in conjunction with the 0.56T and 1.5T beamlets, full incorporation of magnetic field modeling during both stages of the treatment planning process (Case #3) can be assessed.

4.4.1 Parallel Configuration Optimized Plans

For the parallel configurations, the dose difference maps for cases #1 and #2 (i.e. without & with normalization) are nearly identical since the MUs were only adjusted by -0.5% @ $0.56T_{par}$ and -1.1% @ $1.5T_{par}$. Since the dose difference maps of these cases relative to the 0T baseline are difficult to distinguish, only the difference maps for the two extreme cases will be shown (Figures 4.25 and 4.27), where the magnetic field was completely ignored (case #1) or modeled (case #3) throughout the treatment planning process. DVHs will be used to compare the plan qualities for all three cases (Figure 4.26).

For case #1 (representing dose delivered when magnetic field completely ignored), the dose difference maps relative to the $0T_{par}$ baseline (Figure 4.25) show differences that are largest in lung, with less than 1% difference everywhere else in the patient. The majority of the PTV shows less than 1% difference. The only significant differences are on the side facing beam 3, where the PTV is hotter than the $0T_{par}$ case due to the confinement of electrons scattered in the right lung. This is consistent with the fluence analysis in section 4.3; also this effect increases with magnetic field strength, with the hotspot being larger in size and magnitude for the $1.5T_{par}$ case. The hotspots correspond to longer tails in the PTV DVH (Figure 4.26): quantitatively, the PTV D5 value is +0.9% / +5.3% at $0.56T_{par}$ / $1.5T_{par}$ relative to $0T_{par}$. The DVH curve for the right lung nearly overlaps for all three magnetic field strengths, with the $1.5T_{par}$ case lying slightly below the other two curves in the [20-40]% volume range. The mean dose to the right lung changes by less than 1% for both magnetic field strengths in case #1 (Table 4.5). The renormalization done for case #2 reduces the size of the PTV DVH tails slightly, reducing the D5 value percent difference to +0.4% / +4.1% at $0.56T_{par}$ / $1.5T_{par}$, respectively. However it does not eliminate the hot spot on the beam 3 side of the PTV completely at either magnetic field

strength. Despite this, the dose distributions for parallel cases #1 and #2 are likely both acceptable for SBRT treatments, delivering adequate dose coverage to the PTV and sparing of critical structures.

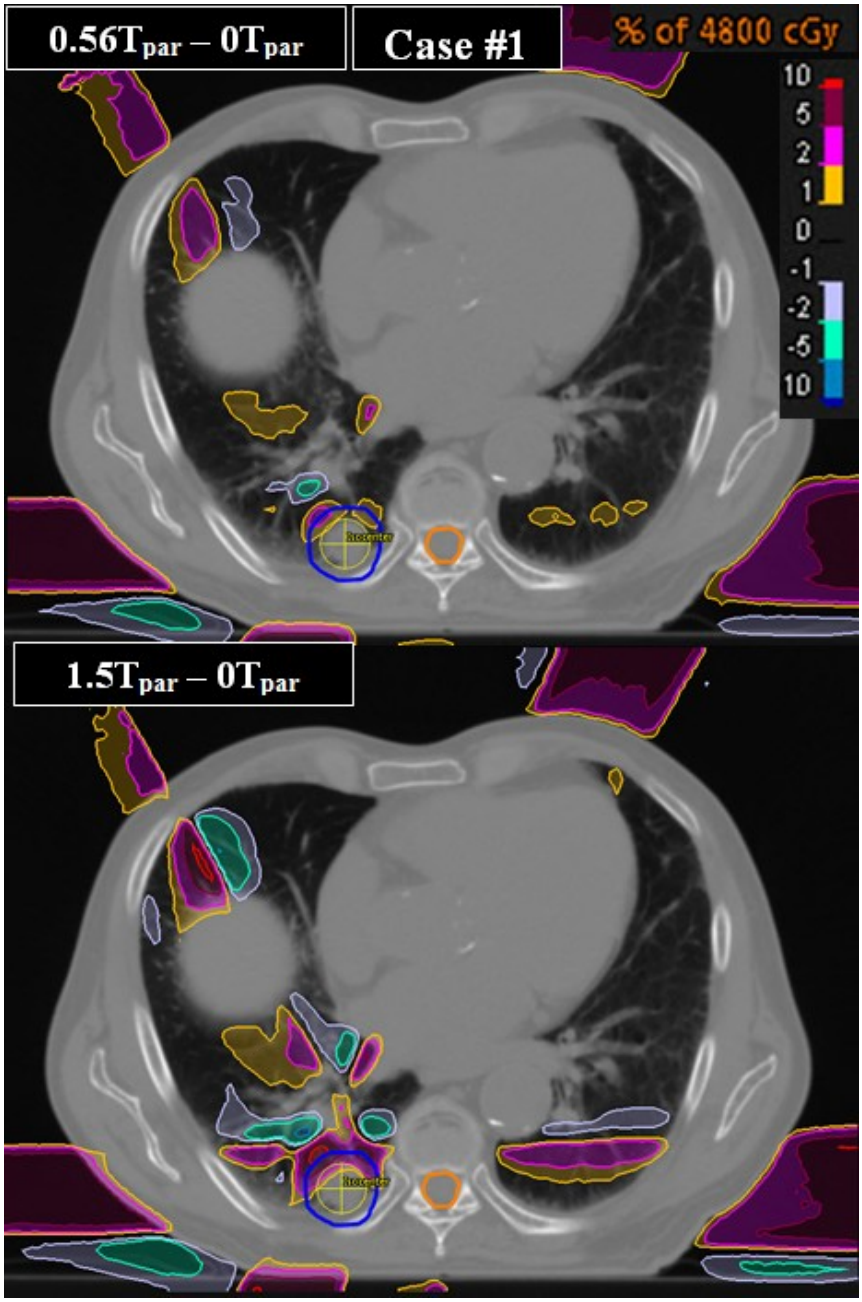

Figure 4.25 Dose difference maps for case #1 for a transverse slice at isocenter. Differences relative to the $0T_{par}$ baseline are expressed as a percentage of the normalization dose of 4800cGy.

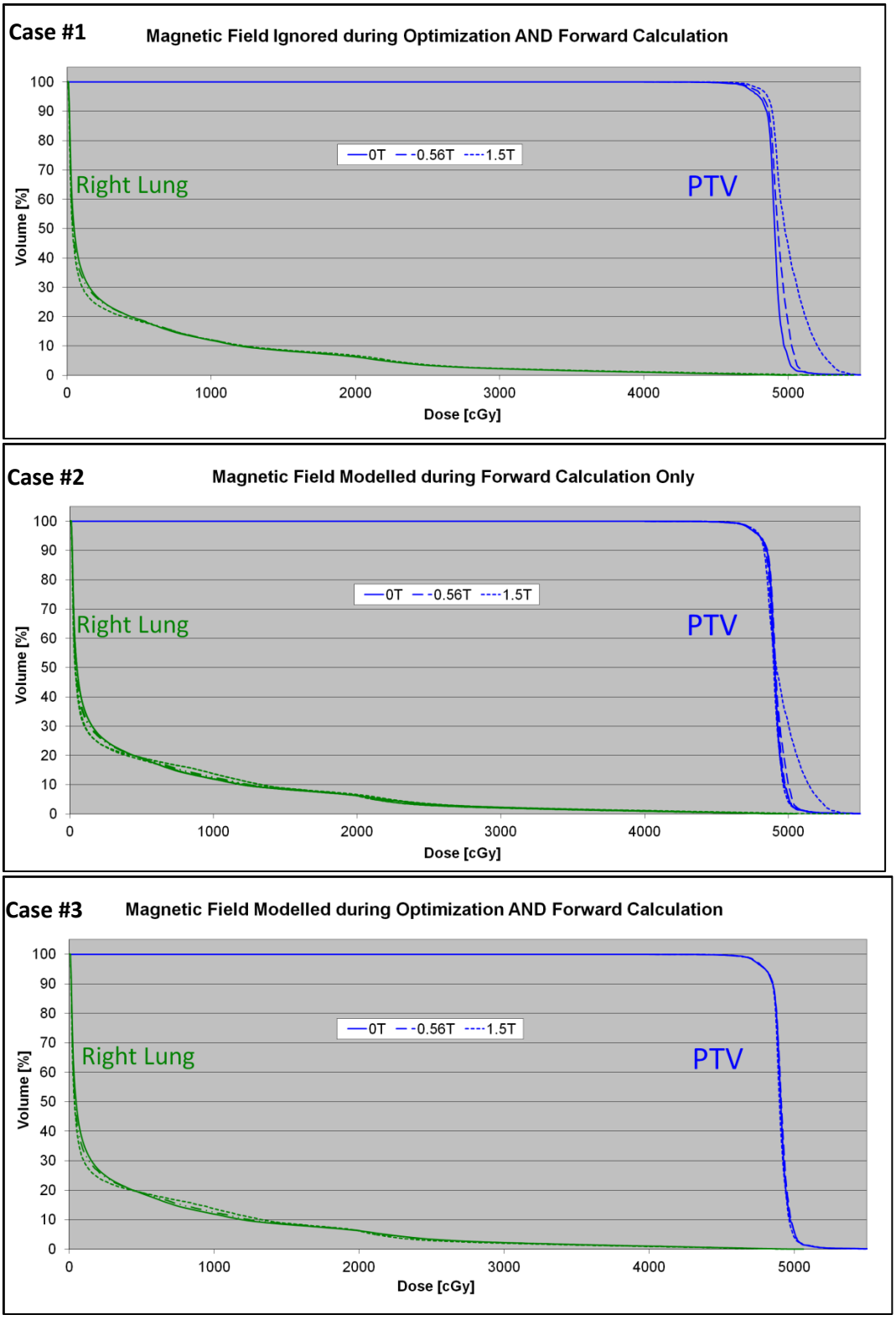

Figure 4.26 Parallel configuration DVHs for three cases. Cases 1 & 2 exhibit longer PTV tails corresponding to small regions of increased dose. Case # 3 delivers an effectively identical plan to the 0T baseline plan. Cases #2 and #3 were normalized to deliver 4800cGy to 95% of PTV.

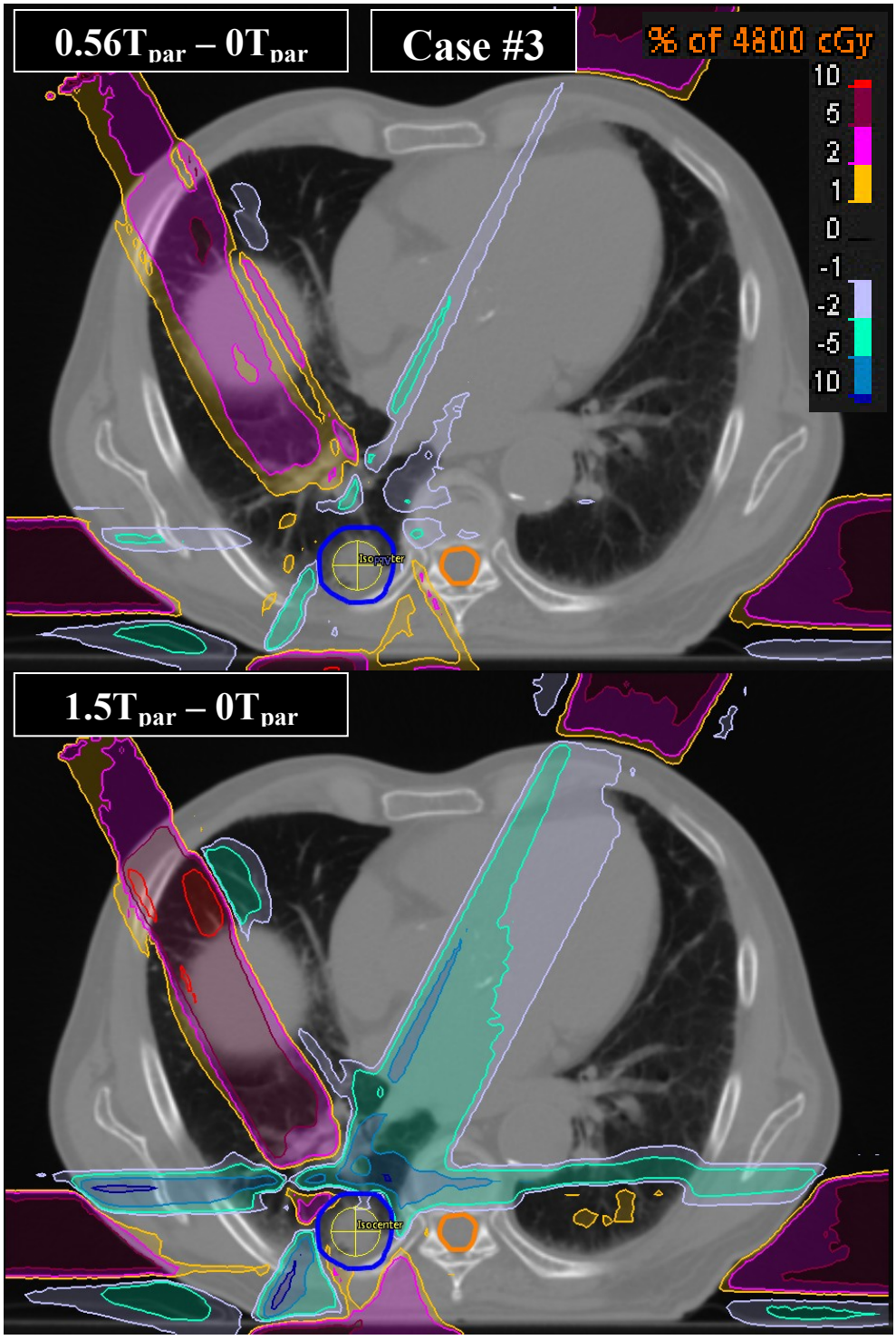

Figure 4.27 Dose difference maps for case #3 (magnetic field modeled during both optimization and forward calculation) for a transverse slice at isocenter. Differences are expressed as a percentage of the normalization dose of 4800cGy.

When the magnetic field is modeled during both the optimization and the forward calculation (case #3), the optimization produced higher quality treatment plans. The optimization is able to deliver effectively identical treatment plans for the parallel configuration at (0T, 0.56T, 1.5T)$_{par}$ in terms of PTV coverage and lung dose. Just like the 0T plan, the 0.56T$_{par}$ and 1.5T$_{par}$ plans deliver very uniform coverage to the entire target volume, and the PTV DVH curves overlap completely in Figure 4.26. The dose difference maps (Figure 4.27) show less than 1% difference in virtually all voxels within the PTV. The mean dose delivered to the right lung (Table 4.6) is the same at 0T$_{par}$ and 0.56T$_{par}$, and is reduced by a clinically insignificant 1.1% at 1.5T$_{par}$. Figure 4.27 also shows that for case #3 more dose is delivered through beam #3 than in cases #1 & #2, when the magnetic field was not modeled during the optimization. As discussed in section 4.3.1, the optimizer delivers more fluence through beam 3 with the parallel magnetic field modeled, since this beam benefits the most from the confinement of scattered electrons in lung.

	Mean Lung Dose [cGy]				
	0T$_{par}$	0.56T$_{par}$	% diff	1.5T$_{par}$	% diff
Case 1	373	374	0.3%	371	-0.5%
Case 2	373	373	0.0%	367	-1.6%
Case 3	373	373	0.0%	369	-1.1%

Table 4.6 Mean dose to lung for parallel Linac-MR configuration optimized plans.

	D95 % difference		D5 % difference	
Case	0.56T$_{par}$	1.5T$_{par}$	0.56T$_{par}$	1.5T$_{par}$
1	0.5%	1.2%	0.9%	5.3%
2	0.0%	0.0%	0.4%	4.1%
3	0.0%	0.0%	0.0%	-0.3%

Table 4.7 Parallel Linac-MR configuration optimized plan quality: **s**ummary of PTV D5 and D95 percent differences relative to 0T baseline plan for cases #1, #2 and #3. D95 % differences for cases 2 and 3 are zero because the dose distributions are normalized to this dose volume point.

4.4.2 Perpendicular Configuration Optimized Plans

The following results demonstrate that the optimization had more difficulty dealing with the perpendicular magnetic field's effect on dose deposition, as predicted in the previous sections (4.2 / 4.3). Figures 4.28 / 4.30 / 4.31 show the dose difference maps for the three different cases in both sagittal and coronal viewing planes at isocenter, with the corresponding DVHs in Figure 4.29. When the magnetic field is ignored entirely (case #1), there is no way to compensate for the lateral shift in dose due to the perpendicular magnetic field. As a result, for case #1, the superior edges of the $0.56T_{perp}$ and $1.5T_{perp}$ dose distributions were colder, and the inferior edges hotter, relative to the $0T_{perp}$ plan. Within the PTV, the perpendicular magnetic field produced both hot and cold spots where dose was lost or gained due to the Lorentz forces on scattered electrons. These differences increase as a function of magnetic field strength, ranging from ±5% within the PTV for the $0.56T_{perp}$ plan, and as much as ±10% for the $1.5T_{perp}$ plan. These hot and cold spots (*i.e.* dose inhomogeneity) are evident in the first DVH of Figure 4.29, where the shoulders of the PTV curves are much wider for the magnetic field cases, representing significant portions of the PTV receiving more or less than the prescribed dose. The dose to 95% of the volume (D95) is -3.5% / -5.2% less at $0.56T_{perp}$ / $1.5T_{perp}$ relative to the $0T_{perp}$ plan, and the dose to 5% of the volume (D5) is 4.8% / 8.3% higher for the same two plans. The cold spots in particular could be problematic, since malignant tissues in these regions would receive less dose than desired. The mean dose to the right lung is -1.3% / -2.9% less for the $0.56T_{perp}$ / $1.5T_{perp}$ plans (Table 4.8); however this sparing does not make up for the degradation of target coverage.

	Mean Lung Dose [cGy]				
	0T	0.56T	% diff	1.5T	% diff
Case 1	373	368	-1.3%	362	-2.9%
Case 2	373	379	1.6%	382	2.4%
Case 3	373	377	1.1%	382	2.4%

Table 4.8 Mean dose to lung for perpendicular Linac-MR configuration optimized plans.

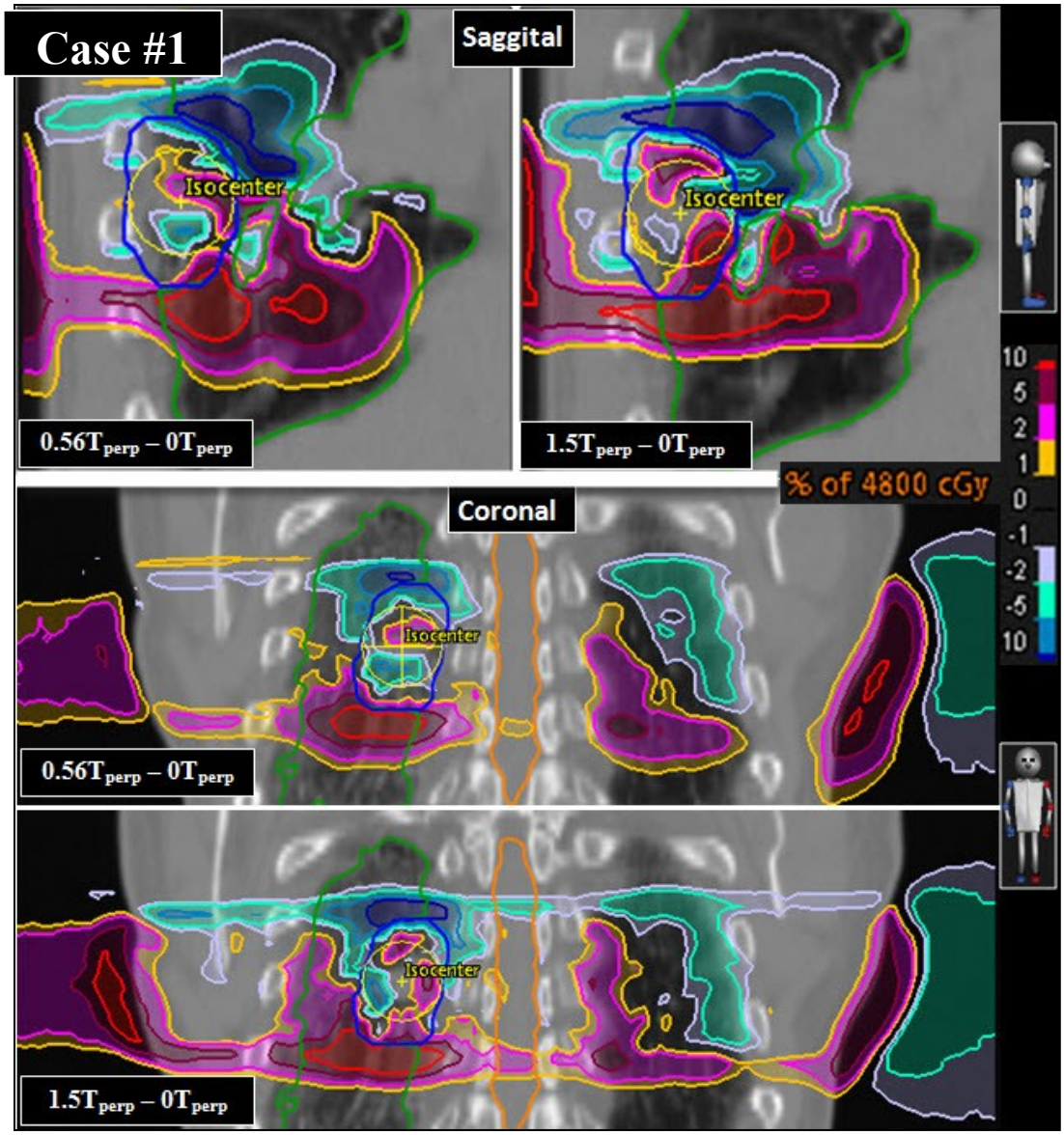

Figure 4.28 Dose difference maps for case #1 (magnetic field not modeled during optimization or forward calculation) on sagittal and coronal slices at isocenter. Differences relative to the 0T baseline are expressed as percentage of the normalization dose of 4800cGy. (PTV contour in dark blue, right lung in green).

	D95 % difference		D5 % difference	
Case	0.56T	1.5T	0.56T	1.5T
1	-3.1%	-5.2%	4.8%	8.3%
2	0.0%	0.0%	8.1%	14.1%
3	0.0%	0.0%	1.9%	4.9%

Table 4.9 Perpendicular Linac-MR configuration optimized plan quality: **s**ummary of PTV D5 and D95 percent differences relative to 0T baseline plan for cases 1, 2 and 3. D95 % differences for cases 2 and 3 are zero because the dose distributions are normalized to this dose volume point.

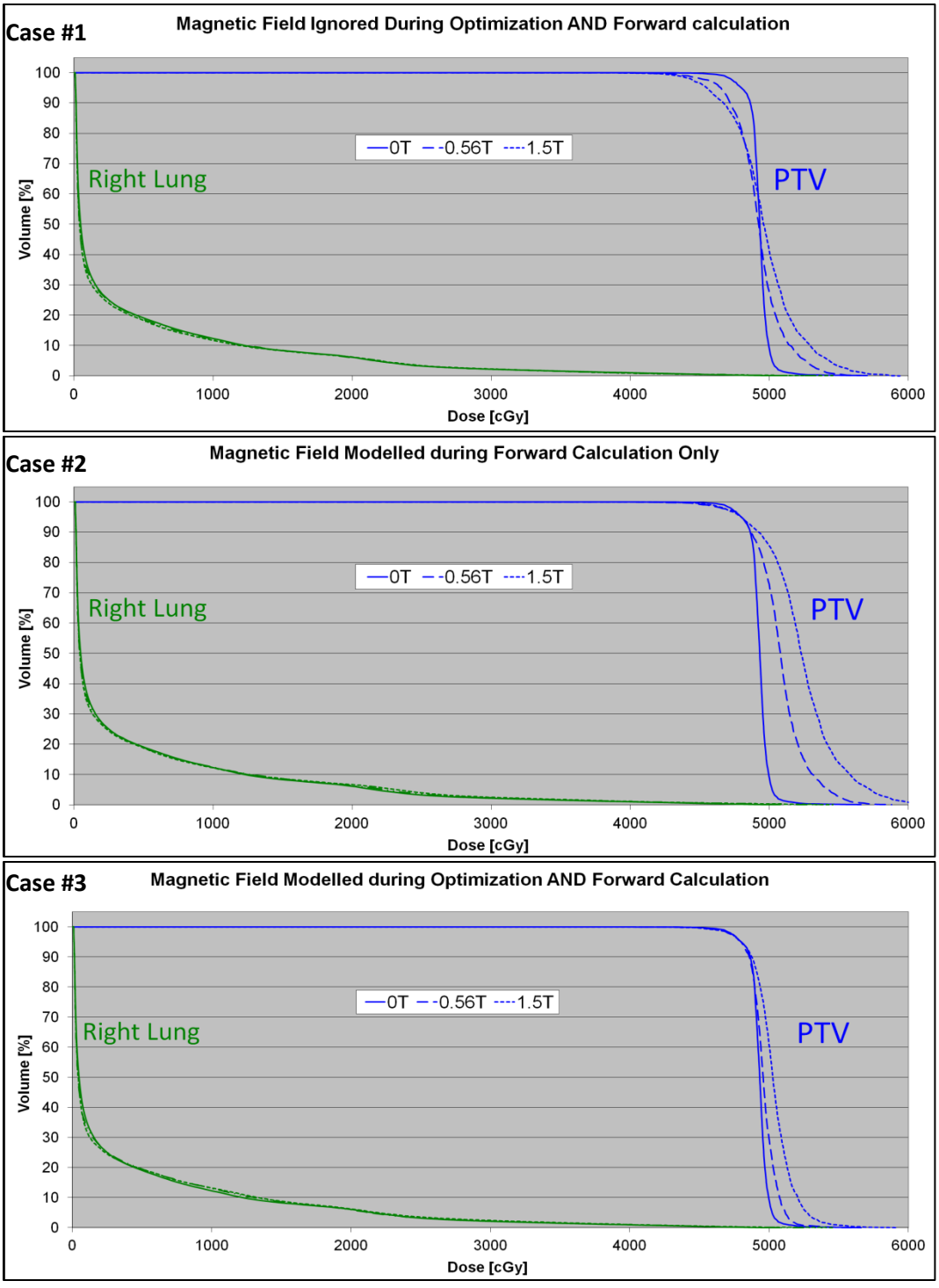

Figure 4.29 Perpendicular configuration optimized DVHs. Case 1 exhibits poor PTV dose uniformity with significant portions of receiving more/less than the prescribed dose. Case 2 increases the number of MUs to remove the cold spots, but further magnifies the hot spots since the fluence shape is unchanged. Case #3 produces the best treatment plan, but still exhibits regions of increased dose with increasing magnetic field strength. Cases #2 and #3 were normalized to deliver 4800cGy to 95% of PTV.

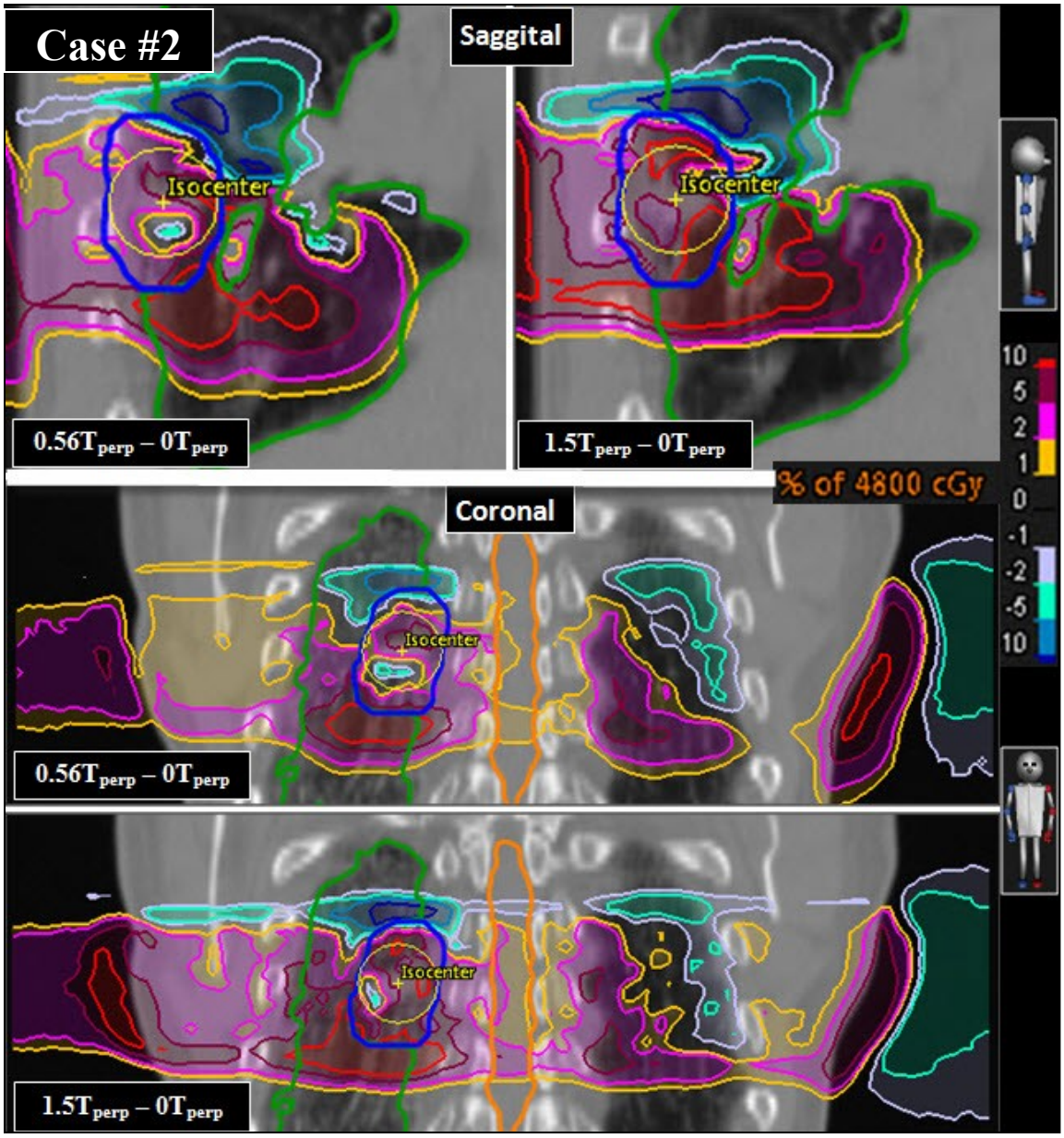

Figure 4.30 Dose difference maps for case #2 (magnetic field modeled during the forward calculation only) on sagittal and coronal slices at isocenter. Differences relative to 0T baseline are expressed as percentage of the normalization dose of 4800cGy. (PTV contour in dark blue, right lung in green)

For case #2 (magnetic field modeled only during the forward calculation), the renormalization of the case #1 plans to achieve 4800 cGy to 95% of the PTV resulted in an increase in MUs of 3.2%/5.4% for the $0.56T_{perp}/1.5T_{perp}$ plans. Although this removed the

majority of the cold spots within the PTV (Figure 4.30), it further magnified the hot spots: the D5 percent difference increased to +8.1% / +14.1% for the $0.56T_{perp}$ / $1.5T_{perp}$ plans, respectively. The mean dose difference relative to 0T for the right lung increased to +1.6% / +2.4% at $0.56T_{perp}$ / $1.5T_{perp}$ (Table 4.8).

The best quality treatment plans are produced when the magnetic field is also modeled during optimization (case #3). Figure 4.31 shows that there are no cold spots within the PTV at either magnetic field strength. However, the dose for the magnetic field plans is still not homogeneous, and is generally hotter than the $0T_{perp}$ plan. This shows that even with the magnetic field modeled throughout the inverse planning process, the optimization algorithm is not able to completely compensate for the effects of the perpendicular magnetic field. The lateral shift in dose caused by the Lorentz forces on scattered electrons makes it difficult to deliver uniform target coverage in lung, and in general seems to require increased dose to some regions of the target in order to achieve the prescription dose of 4800cGy to 95% of the PTV. The DVH in Figure 4.29 is consistent with this conclusion, showing a longer shoulder (dose inhomogeneity) to the right of the $0T_{perp}$ plan, representing higher dose to a larger portion of the target. Similar to previous analysis, the magnetic field effects (dose increase and inhomogeneity) are worse at the higher field strength of $1.5T_{perp}$. The D5 percent difference is still significantly less than cases #1 and #2, sitting at +1.9% / +4.9% at $0.56T_{perp}$ / $1.5T_{perp}$ respectively. The mean dose to the right lung is also increased for the $0.56T_{perp}$ / $1.5T_{perp}$ plans by +1.1% / +2.4% relative to the $0T_{perp}$ plan.

Overall the perpendicular case #3 produces significantly better treatment plans than the cases where the magnetic field was ignored at some stage (cases #1 & #2) , but is still not as good as the equivalent parallel configuration plan for case #3. The hot spots for the perpendicular

case #3 (full incorporation of the magnetic field) are similar in magnitude to the parallel case #1 (no incorporation of the magnetic field), but with an associated increase in the mean lung dose for the perpendicular case.

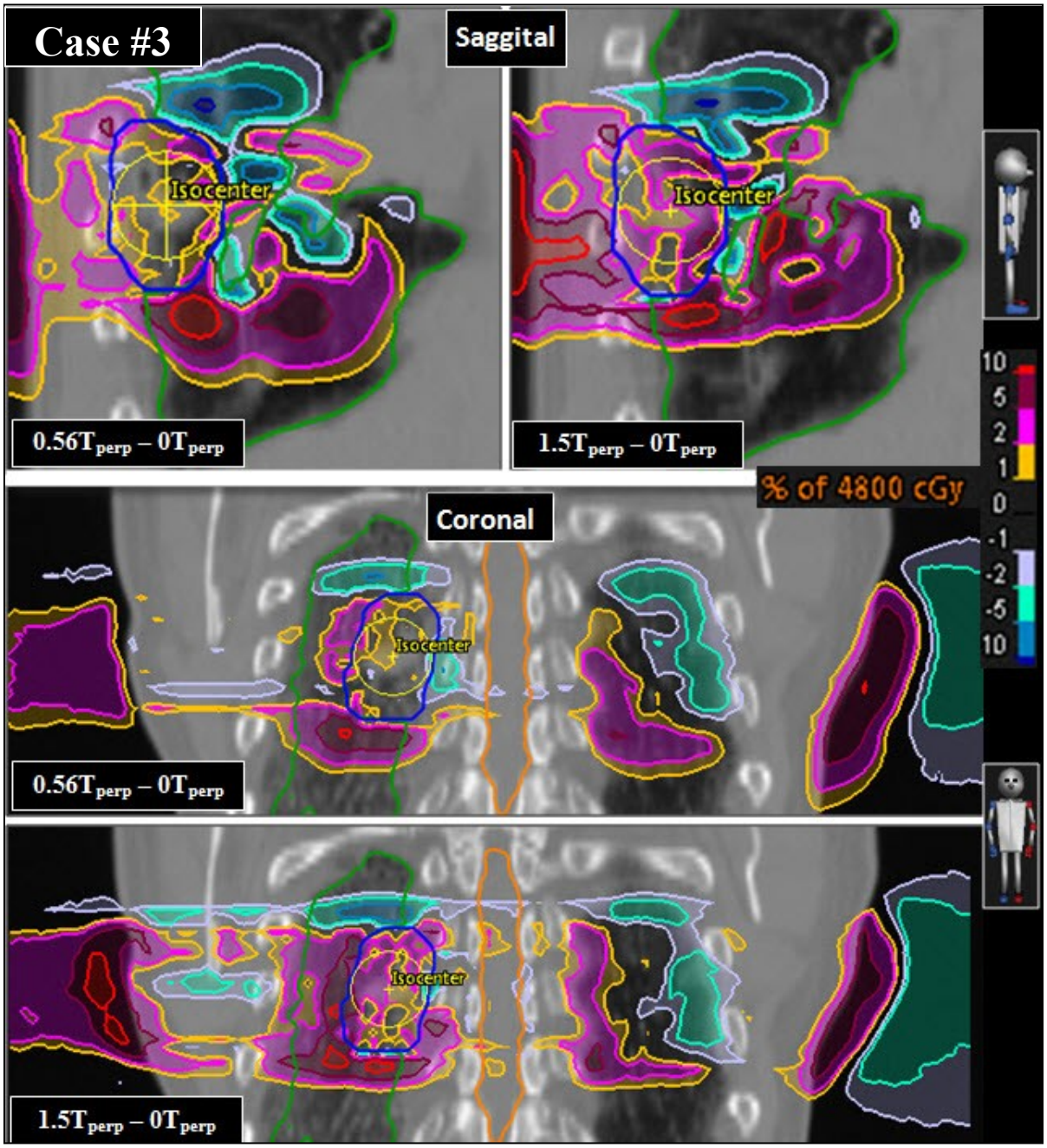

Figure 4.31 Dose difference maps for case #3 (magnetic field modeled during both optimization and forward calculation) on sagittal and coronal slices at isocenter. Differences relative to 0T baseline are expressed as percentage of the normalization dose of 4800cGy. (PTV contour in dark blue, right lung in green).

Chapter 5: Conclusion

Linac-MR systems are part of the next generation of IGRT technologies, enabling rapid acquisition of volumetric image sets with superior soft tissue contrast relative to other OBI technologies. These advanced new hybrid systems have the potential to significantly improve RT patient treatments and outcomes by reducing the size of the clinical ICRU margins used in treatment planning. Specifically, the reduction of the internal margin (IM) and setup margin (SM), which account for intrafractional and interfractional uncertainties respectively, should reduce the dose to healthy tissues and subsequent patient complications.

One complication with Linac-MR systems is the effect on dosimetry of the magnetic field of the MRI system. The magnetic field exerts a Lorentz force on any charged particles traversing it, thus affecting the paths of the secondary electrons depositing dose in a patient. This force acts perpendicular to both the direction of particle travel and the direction of the magnetic field, which can be oriented either parallel or perpendicular to the central beam axis. The effect of this Lorentz force on dose deposition for both magnetic field orientations has been studied extensively, and is most significant in low density regions such as lung where the mean free path of electrons is longer. The impact of this phenomenon on the inverse-planning process for a perpendicular configuration has been investigated by the Utrecht research group (64). However this study excluded the parallel configuration, and did not investigate a low density inhomogeneity such as lung where the Lorentz force exerted by the MRI would have the greatest influence. The aim of this Masters thesis was to address the gap in the current research regarding the dosimetric implications of inverse planning on a Linac-MR system in lung, for both the parallel and perpendicular configurations. The work investigated the importance of modeling the

magnetic field of the Linac-MR system during both the optimization and forward calculation stages of the inverse-planning process. For this purpose a calculation framework was established and validated, which implemented discrete superposition of MC simulated beamlet dose kernels for forward and inverse treatment planning. A simplified SBRT plan for a patient with a tumour seated against the posterior wall of the lung was used for this study. Then three cases were studied where (0T, 0.56T, 1.5T) magnetic fields were: (1) not modeled at all; (2) modeled during the forward calculation only; and (3) modeled for both the optimization and forward calculation stages.

For the parallel configuration, modeling the magnetic field did result in better treatment plans; however even without incorporating the magnetic field, dose differences were generally small, and acceptable plan quality was still achieved. For the case (#1) where the magnetic was ignored completely, the majority of voxels in the patient had less than 1% difference relative to the $0T_{par}$ case. The main differences were at the edges of the beams, especially in lung where the confinement of electrons by the magnetic field reduced the lateral spread of dose deposition. This increased the PTV dose, particularly on the side facing beam 3, which traversed the most lung. As a consequence, the length of the PTV DVH tail at $0.56T_{par}$/$1.5T_{par}$ was increased when the magnetic field was not modeled. When the optimization incorporated the magnetic field (case #3) MUs were shifted out of beams 1 and 2 and into beam 3, suggesting that there was a dosimetric benefit to delivering dose through the beam that traversed the most lung (and thus manifested the electron confinement most significantly). Overall, based on the results summarized in Figure 4.26 and Tables 4.6 and 4.7, the cumulative differences with and without the magnetic field modeled are clinically negligible at $0.56T_{par}$: the PTV and lung DVHs are very similar, and there is less than 1% difference in the dose metrics (mean lung dose, PTV D5

and D95). At $1.5T_{par}$, changes in the lung dose are subtle (*e.g.* < 2% in the mean lung dose), but there is a noticeable change in the tail of the PTV DVH. Compared to when the magnetic field is included in both optimization and forward calculation (case #3), the PTV D5 is 4.1% and 5.3% larger when the magnetic field is ignored during optimization only (case #2) and entirely (case #1), respectively. Nevertheless, hotspots in the target are common for SBRT lung treatments, and these would likely not be considered problematic. Specifically comparing the results from case #2 and case #1 for this SBRT scenario, the error introduced by not including the magnetic field at the final forward calculation stage (after optimizing without the magnetic field) were small: based on the scaling of MUs required in going from case #1 to case #2, the error in the D95 prescription would be -0.5% at 0.56T and -1.1% at $1.5T_{par}$. In general, this was also consistent with the finding from the unmodulated plan analysis that slightly less MUs are required for a parallel magnetic field configuration to deliver the same target coverage in lung.

For the perpendicular configuration, the magnetic field had a much more severe effect on both the optimization and forward dose calculation stages. The Lorentz force exerted by the magnetic field resulted in a significant lateral shift in dose deposition, and was larger for the higher magnetic field strength. Investigating case #1 suggested that the treatment plan quality of the delivered plan (with magnetic field) would be significantly different than the treatment plan calculated with the magnetic field completely ignored. The lateral shift caused by the magnetic field resulted in hot and colds spot in the PTV, and a comparatively large PTV DVH shoulder. Relative to the $0T_{perp}$ baseline, the [D95 ; D5] percent differences were [-3.5% ; +4.8%] at $0.56T_{perp}$, and [-5.2% ; +8.3%] at $1.5T_{perp}$. There was a small reduction in mean lung dose (-1.3% at 0.56T and -2.9% at 1.5T), but this came at the cost of significantly worse target coverage. The renormalization performed for case #2 to satisfy the PTV prescription dose

eliminated the cold spots, but also magnified the hot spots: PTV D5 percent differences became +8.1% and +14.1% at $0.56T_{perp}$ and $1.5T_{perp}$, respectively. The small amount of lung sparing was also lost after renormalization, as the mean dose increased to +1.6% at $0.56T_{perp}$ and +2.4% at $1.5T_{perp}$ (relative to the $0T_{perp}$ baseline). When the magnetic field was modeled at both the optimization and forward calculation stages (case #3), a significantly better treatment plan for the perpendicular configuration was produced. Nonetheless, PTV homogeneity remained inferior to the $0T_{perp}$ plan, and there was a slight increase in the mean lung dose (Figure 4.29, Tables 4.8 and 4.9). Generally, it seems that an increase in dose to some portions of the target is required in order to eliminate cold spots and meet the prescription dose for the perpendicular configuration.

In summary, this research suggests that modeling the magnetic field is much more important for a perpendicular Linac-MR configuration, and for higher magnetic field strengths. In the parallel configuration, the magnetic field could be ignored at both the optimization and forward calculation stages for our lung patient without a significant reduction in plan quality. The main consequence of ignoring the magnetic field would be a small increase in dose to the PTV from any beams traversing a significant amount of lung before reaching the target. Optimization with the magnetic field may also redistribute the relative weights of beams to take advantage of any potential dosimetric benefit of the magnetic confinement of electrons in the parallel configuration, *e.g.* by delivering more fluence through the beam(s) passing through the most lung. A perpendicular magnetic field was shown to have a more significant detrimental effect on lung treatment plans. A potentially significant reduction in PTV homogeneity was observed when the magnetic field was not modeled during optimization, and an additional degradation in target coverage (*e.g.* PTV D95) occurred when also not modeled during forward calculation. Incorporating the magnetic field information during optimization is important to

account for the lateral shift in dose deposition by the magnetic Lorentz force. With the perpendicular magnetic field modeled at both stages of treatment plan generation, an acceptable plan was achieved; however, this perpendicular plan was comparable to the plan quality achieved when the magnetic field was completely ignored for the parallel configuration. It also is noted that, based on our investigation of unmodulated plans for a homogeneous patient, the impact of ignoring the magnetic field entirely would be expected to be negligible for treatment sites having little heterogeneity in the target volume and surrounding tissue.

The results of this research have significant implications with respect to the design of Linac-MR systems, and their range of applicability. The results suggest that a parallel Linac-MR configuration is significantly better suited to treatment of lung patients, and that treatment with a perpendicular configuration would necessitate modeling of the magnetic field during inverse-planning for acceptable treatment plan quality. This study does however have several limitations, and more study of this subject is required. This research did not include any physical measurements to validate the results. It was also limited to a single patient with a simplified SBRT plan, and used a single set of optimization objectives. Further research should include multiple patients and tumour sites in low density regions such as lung, with full clinical treatment plans. Investigation of the dependence of results on optimization objectives should also be performed, as well as experimental verification of dosimetry on a physical Linac-MR system.

References

1. Cancer statistics at a glance [Internet].; 2016 []. Available from: http://www.cancer.ca/en/cancer-information/cancer-101/cancer-statistics-at-a-glance/?region=on.

2. Röntgen WC. On a New Kind of Rays. Science. 1896 Feb. 14, 1896;3(59):227-31.

3. Cierniak R. Some words about the history of computed tomography. In: X-Ray Computed Tomography in Biomedical Engineering. 1st ed. Springer-Verlag London; 2011. p. 7-19.

4. The Nobel Prize in Physics 1901 [Internet].: Nobel Media AB 2014; 5 Jan 2016 []. Available from: http://www.nobelprize.org/nobel_prizes/physics/laureates/1901/.

5. J.Bernier, E.J. Hall, A. Giaccia. Radiation Oncology: A Century of Achievements. Nature Reviews. 2004;4:737-747.

6. Blaufox MD. Becquerel and the discovery of radioactivity: early concepts. Semin Nucl Med. 1996 Jul;26(3):145-54.

7. Trombetta M. Madame Maria Sklodowska-Curie - brilliant scientist, humanitarian, humble hero: Poland's gift to the World. J Contemp Brachytherapy. 2014 Oct;6(3):297-9.

8. Gerward L. Paul Villard and his Discovery of Gamma Rays. Physics in Perspective. 2014;1(4):367-83.

9. Rutherford E. XV. The magnetic and electric deviation of the easily absorbed rays from radium. Philosophical Magazine Series 6. 1903 02/01;5(26):177-87.

10. Clarke RH, Valentin J. The History of ICRP and the Evolution of its Policies. Ann ICRP. 2009 /2;39(1):75-110.

11. Spiegel PK. The first clinical X-ray made in America--100 years. Am J Roentgenol. 1995 01/01; 2016/01;164(1):241-3.

12. Grubbé EH. Priority in the Therapeutic Use of X-rays. Radiology. 1933 08/01; 2016/01;21(2):156-62.

13. Mould RF. Pierre curie, 1859-1906. Curr Oncol. 2007 Apr;14(2):74-82.

14. Robison RF. The race for megavoltage. X-rays versus telegamma. Acta Oncol. 1995;34(8):1055-74.

15. WAYTE AB. Treatment of some disorders of the pituitary by radiotherapy. Proc R Soc Med. 1951 Jun;44(6):450-2.

16. Failla G. - An Objective Method for the Administration of X-Rays. - Acta Radiologica. 1925(- 2):- 85.

17. Bernier J. Radiation Oncology: A Century of Progress and Achievement ; 1895-1995. Printal; 1995.

18. Coutard H. PRINCIPLES OF X RAY THERAPY OF MALIGNANT DISEASES. - The Lancet. 1934(- 5784):- 5.

19. James M. Slater. From X-Rays to Ion Beams: A Short History of Radiation Therapy. In: Linz U(), editor. Ion Beam Therapy Fundamentals, Technology, Clinical Applications. Springer; 2012. p. 3-13.

20. Coursey BM, Colle R, Coursey JS. Standards of radium-226: from Marie Curie to the International Committee for Radionuclide Metrology. Appl Radiat Isot. 2002 Jan-Feb;56(1-2):5-13.

21. JOHNS HE, BATES LM, EPP ER, CORMACK DV, FEDORUX SO, MORRISON A, et al. 1,000-Curie Cobalt 60 Units for Radiation Therapy. Nature. 1951 Dec 15;168(4285):1035-6.

22. FRY DW, R-SHERSBY-HARVIE RB. A traveling-wave linear accelerator for 4-MeV. electrons. Nature. 1948 Nov 27;162(4126):859-61.

23. A History of the Radiological Sciences
Chapter 15: Conventional Tomography [Internet].; 2012 []. Available from: http://www.arrs.org/publications/HRS/diagnosis/RCI_D_c15.pdf.

24. Radon J. On the Determination of Functions from Their Integral Values along Certain Manifolds. IEEE Trans Med Imaging. 1986;5(4):170-6.

25. KACZMARZ S. Approximate solution of systems of linear equations†. Int J Control. 1993 06/01;57(6):1269-71.

26. Turing AM. On Computable Numbers, with an Application to the Entscheidungsproblem. Proceedings of the London Mathematical Society. 1937 January 01;s2-42(1):230-65.

27. Cormack AM. Representation of a Function by Its Line Integrals, with Some Radiological Applications. J Appl Phys. 1963;34(9):2722-7.

28. CT scanning the early days. Br J Radiol. 2006 01;79(937):5.

29. Gordon R, Bender R, Herman GT. Algebraic reconstruction techniques (ART) for three-dimensional electron microscopy and x-ray photography. J Theor Biol. 1970 Dec;29(3):471-81.

30. The Nobel Prize in Physiology or Medicine 1979 [Internet].: Nobel Media AB 2014; 27 Jan 2016 []. Available from: http://www.nobelprize.org/nobel_prizes/medicine/laureates/1979/.

31. Van Dyk J. The Modern Technology of Radiation Oncology: A Compendium for Medical Physicists and Radiation Oncologists. Chapter 4. Van Dyk J, editor. Medical Physics Pub; 2005.

32. Takahashi S. Conformation radiotherapy. Rotation techniques as applied to radiography and radiotherapy of cancer. Acta Radiol Diagn (Stockh). 1965:242:1.

33. Kitabatake T, Takahashi S. Conformation radiotherapy by means of a 6 MeV linear accelerator. Tohoku J Exp Med. 1968 Jan;94(1):37-43.

34. Brahme A. Optimization of stationary and moving beam radiation therapy techniques. Radiother Oncol. 1988 Jun;12(2):129-40.

35. Yu CX, Amies CJ, Svatos M. Planning and delivery of intensity-modulated radiation therapy. Med Phys. 2008 Dec;35(12):5233-41.

36. Pagani E, Bizzi A, Di Salle F, De Stefano N, Filippi M. Basic concepts of advanced MRI techniques. Neurol Sci. 2008 Oct;29 Suppl 3:290-5.

37. ICRU Report 50: Prescribing, Recording and Reporting Photon Beam Therapy. Bethesda, Md. : International Commission on Radiation Units and Measurements, c1993; 1993.

38. ICRU Report 62: Prescribing, Recording and Reporting Photon Beam Therapy (Supplement to ICRU report 50). Bethesda, Md. : International Commission on Radiation Units and Measurements, c1999; 1999.

39. Shahrestanakay AK. Skin dose in longitudinal and transverse Linac-MRIs using Monte-Carlo and realistic 3D MRI field model. Edmonton, AB. : University of Alberta, 2013.

40. Radiotherapy equipment. Coordinates, movements and scales / Strahlentherapie-Einrichtungen. Koordinaten, Bewegungen und Skalen / Appareils utilisés en radiothérapie. Coordonnées, mouvements et échelles. BSI Standards Limited; 2012.

41. Rietzel E, Rosenthal SJ, Gierga DP, Willet CG, Chen GT. Moving targets: detection and tracking of internal organ motion for treatment planning and patient set-up. Radiother Oncol. 2004 Dec;73 Suppl 2:S68-72.

42. van Herk M. Errors and margins in radiotherapy. Semin Radiat Oncol 2016/01;14(1):52-64.

43. Langen KM, Jones DT. Organ motion and its management. Int J Radiat Oncol Biol Phys. 2001 May 1;50(1):265-78.

44. Kilby W, Dooley JR, Kuduvalli G, Sayeh S, Maurer CR,Jr. The CyberKnife Robotic Radiosurgery System in 2010. Technol Cancer Res Treat. 2010 Oct;9(5):433-52.

45. Shirato H, Shimizu S, Kitamura K, Nishioka T, Kagei K, Hashimoto S, et al. Four-dimensional treatment planning and fluoroscopic real-time tumor tracking radiotherapy for moving tumor. Int J Radiat Oncol Biol Phys. 2000 Sep 1;48(2):435-42.

46. P G Seiler and H Blattmann and S Kirsch and R K Muench and,Ch Schilling. A novel tracking technique for the continuous precise measurement of tumour positions in conformal radiotherapy. Phys Med Biol. 2000;45(9):N103.

47. Hoisak JD, Sixel KE, Tirona R, Cheung PC, Pignol JP. Correlation of lung tumor motion with external surrogate indicators of respiration. Int J Radiat Oncol Biol Phys. 2004 Nov 15;60(4):1298-306.

48. Schlosser J, Salisbury K, Hristov D. Telerobotic system concept for real-time soft-tissue imaging during radiotherapy beam delivery. Med Phys. 2010 Dec;37(12):6357-67.

49. Zhong Y, Stephans K, Qi P, Yu N, Wong J, Xia P. Assessing feasibility of real-time ultrasound monitoring in stereotactic body radiotherapy of liver tumors. Technol Cancer Res Treat. 2013 Jun;12(3):243-50.

50. Fallone BG. The rotating biplanar linac-magnetic resonance imaging system. Semin Radiat Oncol. 2014 Jul;24(3):200-2.

51. Jaffray DA, Carlone MC, Milosevic MF, Breen SL, Stanescu T, Rink A, et al. A Facility for Magnetic Resonance–Guided Radiation Therapy. Semin Radiat Oncol. 2014 7;24(3):193-5.

52. Keall PJ, Barton M, Crozier S, Australian MRI-Linac Program, including contributors from Ingham Institute, Illawarra Cancer Care Centre, Liverpool Hospital, Stanford University, Universities of Newcastle, Queensland, Sydney, Western Sydney, and Wollongong. The Australian magnetic resonance imaging-linac program. Semin Radiat Oncol. 2014 Jul;24(3):203-6.

53. Lagendijk JJW, Raaymakers BW, van Vulpen M. The Magnetic Resonance Imagingâ€“Linac System. Semin Radiat Oncol. 2014 /7;24(3):207-9.

54. Mutic S, Dempsey JF. The ViewRay system: magnetic resonance-guided and controlled radiotherapy. Semin Radiat Oncol. 2014 Jul;24(3):196-9.

55. Keyvanloo A, Burke B, Warkentin B, Tadic T, Rathee S, Kirkby C, et al. Skin dose in longitudinal and transverse Linac-MRIs using Monte Carlo and realistic 3D MRI field models. Med Phys. 2012 Oct;39(10):6509-21.

56. Kirkby C, Stanescu T, Rathee S, Carlone M, Murray B, Fallone BG. Patient dosimetry for hybrid MRI-radiotherapy systems. Med Phys. 2008;35(3):1019-27.

57. Kirkby C, Murray B, Rathee S, Fallone BG. Lung dosimetry in a Linac-MRI radiotherapy unit with a longitudinal magnetic field. Med Phys. 2010 Sep;37(9):4722-32.

58. Raaijmakers AJE, Raaymakers BW, Lagendijk JJW. Integrating a MRI scanner with a 6 MV radiotherapy accelerator: dose increase at tissue–air interfaces in a lateral magnetic field due to returning electrons. Phys Med Biol. 2005 7 April 2005;50(7):1363-76.

59. Bielajew AF. The effect of strong longitudinal magnetic fields on dose deposition from electron and photon beams. Med Phys. 1993 Jul-Aug;20(4):1171-9.

60. Raaijmakers AJE, Raaymakers BW, Meer Svd, Lagendijk JJW. Integrating a MRI scanner with a 6 MV radiotherapy accelerator: impact of the surface orientation on the entrance and exit dose due to the transverse magnetic field. Phys Med Biol. 2007 21 February 2007;52(4):929-39.

61. Raaijmakers AJE, Raaymakers BW, Lagendijk JJW. Magnetic-field-induced dose effects in MR-guided radiotherapy systems: dependence on the magnetic field strength. Phys Med Biol. 2008 21 February 2008;53(4):909-23.

62. Raaymakers BW, Raaijmakers AJE, Kotte ANTJ, Jette D, Lagendijk JJW. Integrating a MRI scanner with a 6 MV radiotherapy accelerator: dose deposition in a transverse magnetic field. Phys Med Biol. 2004 7 September 2004;49(17):4109-18.

63. Chen Y, Bielajew AF, Litzenberg DW, Moran JM, Becchetti FD. Magnetic confinement of electron and photon radiotherapy dose: a Monte Carlo simulation with a nonuniform longitudinal magnetic field. Med Phys. 2005 Dec;32(12):3810-8.

64. Bol GH, Hissoiny S, Lagendijk JJ, Raaymakers BW. Fast online Monte Carlo-based IMRT planning for the MRI linear accelerator. Phys Med Biol. 2012 Mar 7;57(5):1375-85.

65. Podgoršak EB. Interaction of Photons with Matter. 2014:387-514.

66. Podgoršak EB. Basic Radiation Physics. In: Radiation Oncology Physics: A Hondbook for Teachers and Students. Austria: International Atomic Energy Agency (IAEA); 2005. p. 1-43.

67. Keyvanloo A, Warkentin B, Fallone BG, Field GC. The Effects of Patient Anatomy and Parallel Magnetic Fields on Beamlet Dose Distributions. AAPM Poster SU-E-T-469. 2012.

68. Monte Carlo Method [Internet].: Wikipedia; 2016 [updated 22 May 2016;]. Available from: https://en.wikipedia.org/wiki/Monte_Carlo_method.

69. Mathworld - A Wolfram Web Resource [Internet].; 2016 []. Available from: http://mathworld.wolfram.com/LawofLargeNumbers.html.

70. Walters B, Kawrakow I, Rogers DWO. DOSXYZnrc UsersManual. 2011.

71. D.W.O. Rogers, B. Walters, I. Kawrakow. BEAMnrc Users Manual. 2011.

72. Kawrakow I, Mainegra-Hing E, Rogers DWO, Tessier F, Walters BRB. The EGSnrc Code System: Monte Carlo Simulation of Electron and Photon Transport. NRCC Report PIRS-701. May 10 2011.

73. Berger MJ. Monte Carlo calculation of the penetration and diffusion of fast charged particles. . 1963.

74. Podgoršak EB. External Photon Beams: Physical Aspects. In: Radiation Oncology Physics: A Hondbook for Teachers and Students. Austria: International Atomic Energy Agency (IAEA); 2005. p. 161-217.

75. Podgoršak EB. Clinical treatment planning in external photon beam radiotherapy. In: Radiation Oncology Physics: A Hondbook for Teachers and Students. Austria: International Atomic Energy Agency (IAEA); 2005. p. 219-272.

APPENDIX A:

Coordinate transformations for EGSnrc simulations of non-head first supine patients

Abstract: One application of the EGSnrc Monte Carlo (MC) software package is the dosimetric verification of clinical radiotherapy treatment plans. To perform such verifications, the treatment planning system (TPS) parameters describing the clinical treatment geometry must be transformed to the corresponding EGSnrc parameters. This transformation is non-trivial, and requires understanding of the relationships between all involved coordinate systems. Previous publications derived transformations for patients planned in a Head First Supine (HFS) position. Using a similar approach, this paper extends these works by deriving a set of coordinate transformations for three other standard patient orientations used clinically in radiotherapy: Feet First Supine (FFS); Head First Prone (HFP), and Feet First Prone (FFP). Modifications to the EGSnrc module CTcreate were necessary to correctly handle these other patient orientations. The coordinate transformations were validated by comparing MC and TPS-generated dose distributions for 8 treatment geometries of varying degrees of complexity. The derived transformations and modified CTcreate code will enable EGSnrc users to perform dosimetric verifications of clinical treatment plans for four commonly used patient orientations.

Key words: Monte Carlo, Coordinate Transformations, Treatment Planning Systems

PACS numbers 87.55.K-, 87.55.D-

A.1 Introduction

Monte Carlo (MC) simulation is widely accepted as an accurate method of dose calculation in the presence of tissue heterogeneities. One of the most commonly used MC codes in radiotherapy is EGSnrc, a software package developed and distributed by the National Research Council of Canada (1). BEAMnrc and DOSXYZnrc are two components of this package, which are used to simulate radiation transport through the linear accelerator (linac) components and patient geometry, respectively.

The conversion of the treatment planning system (TPS) parameters describing a treatment plan to those required by the EGSnrc software to simulate the same plan is non-trivial (2). Typically, a TPS defines a clinical treatment plan using the International Electrotechnical Commission (IEC) 61217 standard for radiotherapy equipment (3). IEC parameters specifying the plan geometry include: collimator jaw positions (X1,X2,Y1,Y2), multi-leaf collimator (MLC) positions, gantry angle (θ_G), table angle (θ_T), collimator angle (θ_C), source axis distance (SAD), beam quality and energy. The gantry, table and collimator angles describe the beam direction and collimator rotation in the TPS with respect to a *fixed machine* coordinate system.

Computed tomography (CT) images are used by the DOSXYZnrc module CTcreate to generate a 3D *density matrix* file, required to calculate absorbed dose distributions. This density matrix used by DOSXYZnrc is defined using the same DICOM patient coordinate system established at the time of the CT scan. DOSXYZnrc implements a *patient-specific* spherical polar coordinate system, with angles θ and φ describing the beam direction, and φ_{col} specifying the rotation in the collimator plane. A third coordinate system is used by BEAMnrc to define jaw and MLC positions, which differs slightly from the one used by IEC-compliant TPSs. The relationships

and transformations necessary to translate TPS plan geometry to the corresponding EGSnrc geometry are illustrated in Figure A.1.

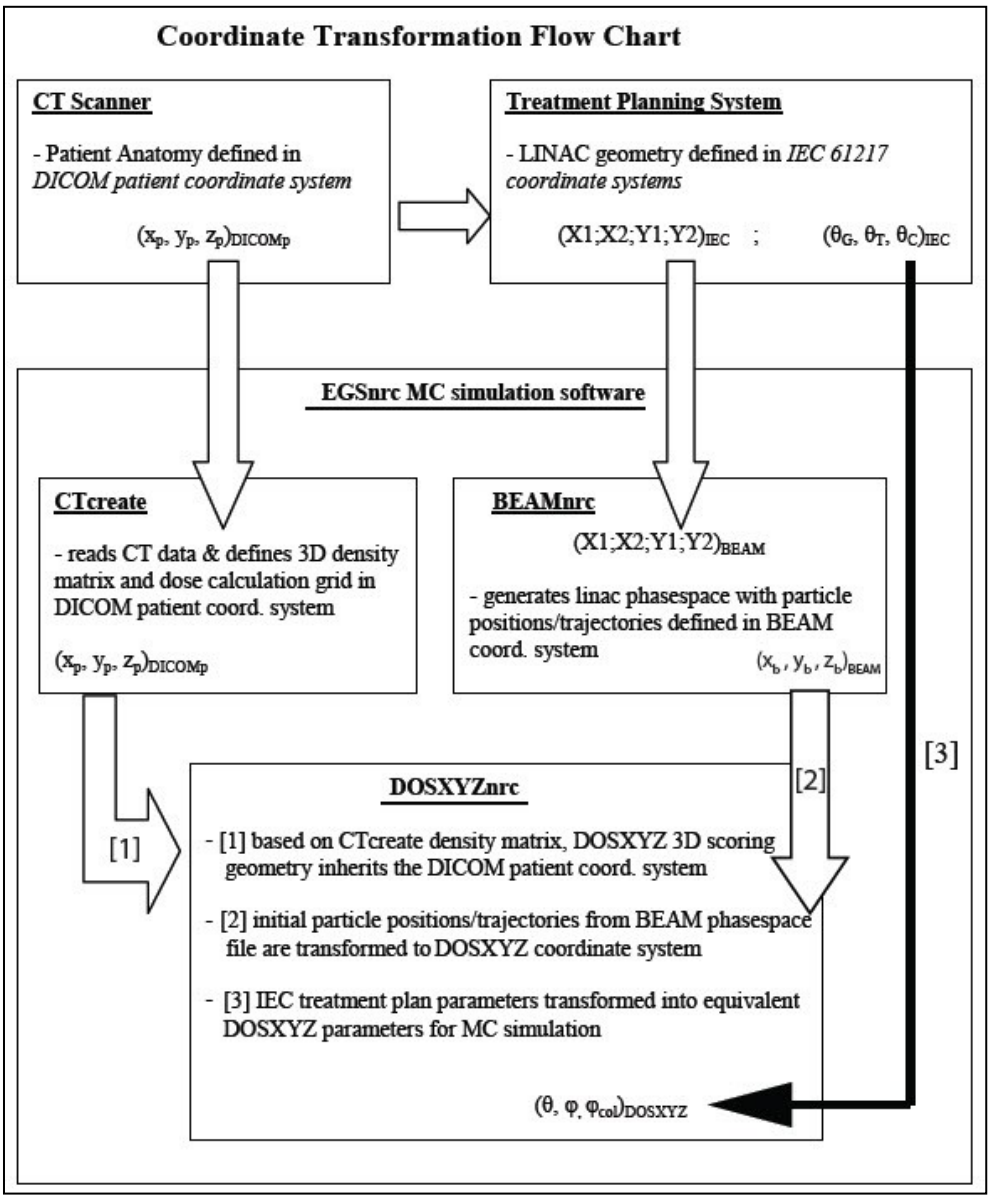

Figure A.1 The simulation of the dose distribution in DOSXYZnrc requires a CTcreate generated density matrix [1], a BEAMnrc simulated phase space [2], and transformed geometric parameters from the TPS [3].

A coordinate transformation utilizing rotation matrices was proposed by Thebault et al (4), and has been further refined by Bush et al and Zhan et al (5, 6). These previous works, however, only considered a Head First Supine (HFS) imaging and treatment position. We extend previous work by deriving coordinate transformations for three additional patient orientations: Feet First Supine (FFS); Head First Prone (HFP); and Feet First Prone (FFP). (*It is noted that during completion of this paper, we discovered that Thebault et. al had submitted a paper on the same subject to an online prepublication. They addressed the same problems as we did, but used a different method* (7).) The associated coordinate transformations for each orientation were derived using rotation matrices to define the beam direction $(\theta, \varphi)_{DOSXYZ}$. The method proposed by Zhan et al for projecting the table angle into the collimator rotation plane, was used to determine the transformation for φ_{col}. The modification of the resulting transformation for φ_{col} when using a BEAMnrc generated phase space source is explained in detail by examining DOSXYZnrc code. Our coordinate transformations for all patient orientations were validated using test cases of increasing geometric complexity. In addition, we identify several shortcomings of the CTcreate module, and describe the corrections necessary to generate density matrices for the three additional patient orientations.

A.2 Background & Theory

A.2.1 CTcreate and the Density Matrix

Typically, the density matrix used for a MC simulation in DOSXYZ is created by the program CTcreate. CTcreate reads in a CT data set and outputs a .egsphant text file containing the information needed to score dose in the patient anatomy. Thus the density matrix inherits the DICOM patient coordinate system of the CT data. User input to CTcreate is used to define the

"ramp" function for converting CT data into material types and densities, and to select the sub-volume of the CT data and the voxel resolution for the generated density matrix. Information in the .egsphant file includes: the number of voxels in x, y, and z; the coordinates of the intersecting planes of these voxels (in the DICOM patient coordinate system); the number and names of materials present; the material and physical density for each voxel (slice-by-slice).

A.2.2 Coordinate Systems

The coordinate systems involved in a radiotherapy treatment plan include the patient coordinate system of the CT scan, and the machine coordinate systems used to define the geometry of the treatment beams (3). In this work we assume these are DICOM-compliant and IEC 61217-compliant, respectively.

A.2.2.1 IEC 61217 Treatment Planning Coordinate Systems

The machine coordinate system is comprised of a series of parent-daughter coordinate systems, with each being assigned to a part of the equipment that can be moved independently. The angles $(\theta_G, \theta_T, \theta_C)_{IEC}$, and the $(X1,X2,Y1,Y2)_{IEC}$ positions of the collimator jaws fully define the geometry of an unmodulated (no MLC) treatment plan with respect to isocenter. The relevant coordinate systems are summarized in Table A.1 and Figure A.2.

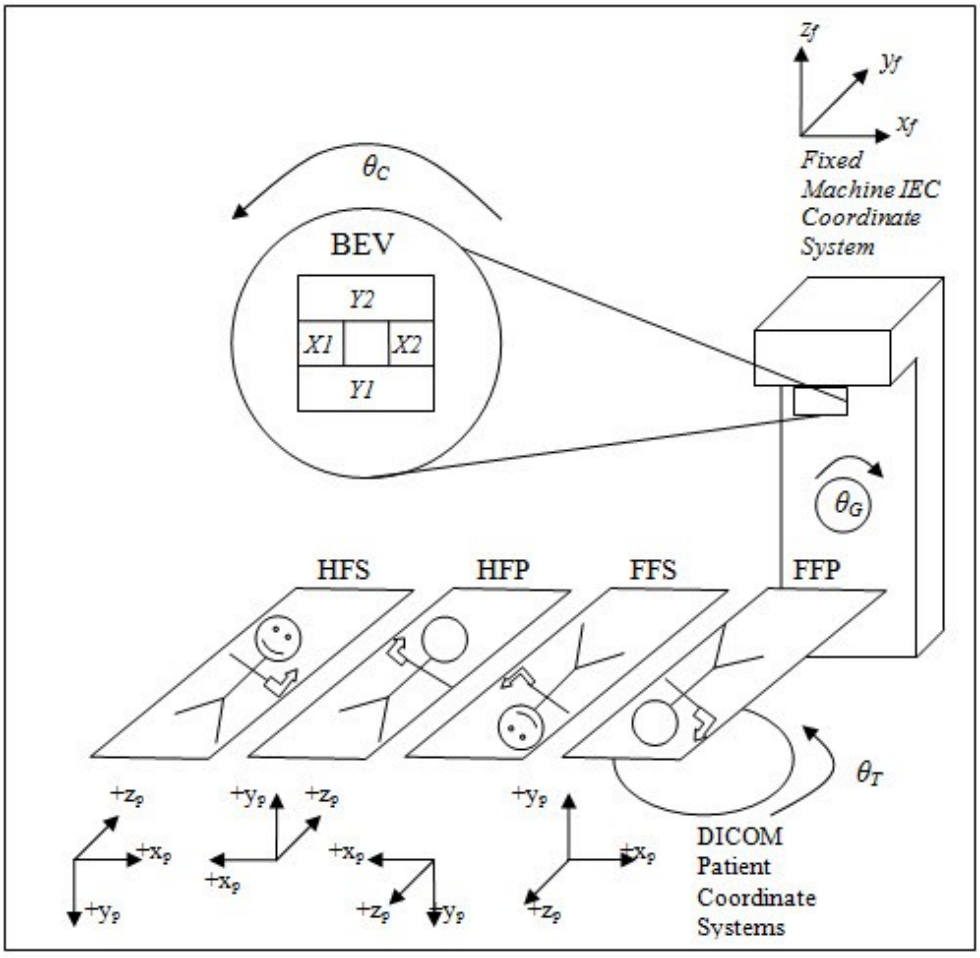

Figure A.2 Coordinate System Orientations, IEC coordinate system parameters in italics, DICOM patient coordinate system orientations shown for four patient orientations. The patients left hand is indicated by an arrow.

Coordinate System	Orientation	Origin location	Comment
Patient (DICOM CT)	$+x_p$ = patient left $+y_p$ = patient posterior $+z_p$ = patient superior	User-defined; typically at centre of CT field-of-view in x,y	Moves with patient and table
Machine Fixed	(facing gantry) $+x_f$ = right $+y_f$ = towards gantry $+z_f$ = upward	Isocenter	Fixed in space, does not move with machine. Parent of other IEC coordinate systems
Gantry	θ_G = clockwise rotation (facing gantry)	$\theta_G = 0$ when gantry at 12 o'clock	Defines rotation of gantry relative to machine fixed system
Beam Limiting Device	θ_C = counter-clockwise rotation in beams eye view (BEV) $(X1,X2,Y1,Y2)_{IEC}$ = distance from origin at isocenter plane	$\theta_C = 0$ when normal to Y1 jaw points along $-y_f$ Isocenter ; $+x_{IEC}$ axis points towards X2 jaw and $+y_{IEC}$ points towards Y2 jaw (Figure 5)	For collimator and MLC positions $(X1,X2,Y1,Y2)_{IEC}$ specified at the plane perpendicular to the central axis at isocenter
Patient Support	θ_T = counter-clockwise rotation (viewed from above)	$\theta_T = 0$ when head of table faces gantry	Defines rotation of table, and therefore of DICOM patient coordinate system relative to fixed machine system

Table A.1 Radiotherapy coordinate system descriptions

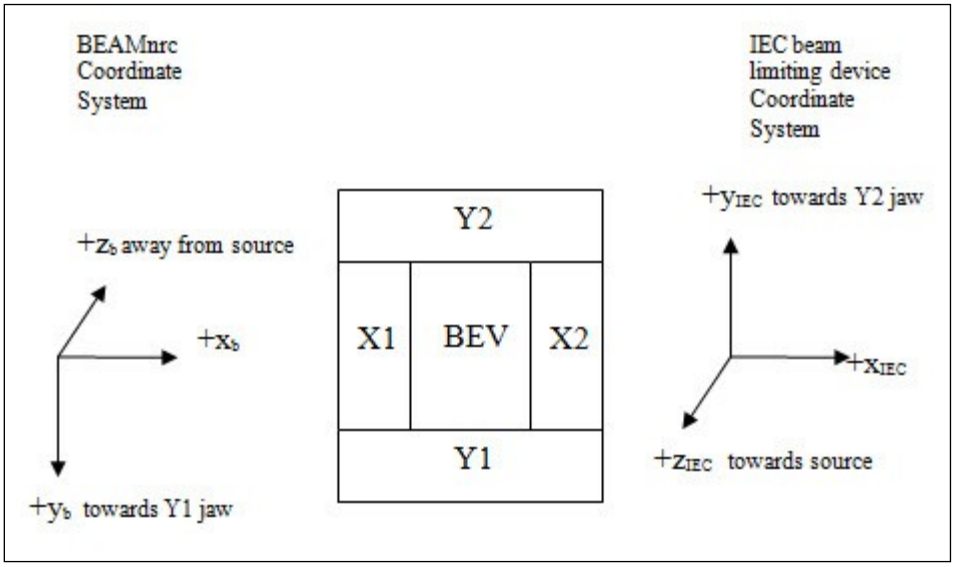

Figure A.5 Beams eye view of collimator, with IEC and BEAMnrc coordinate systems used to define jaw positions.

To perform dose calculations, a TPS registers the patient CT scan with the linac geometry. Analogously, to run a MC simulation of a particular treatment, the machine and patient geometry must be registered by converting the $(\theta_G, \theta_T, \theta_C)_{IEC}$, and $(X1,X2,Y1,Y2)_{IEC}$ parameters to the equivalent values that replicate the same treatment geometry in the MC software. The DICOM patient coordinate system associated with a CT image series is attached to the patient, always preserving a LPS (+x Left, +y Posterior, +z Superior) orientation (Figure A.2). Hence, a different coordinate transformation from the TPS to DOSXYZnrc parameters is required for each unique patient orientation.

A.2.2.2 EGSnrc Monte Carlo coordinate systems

The BEAMnrc and DOSXYZnrc codes of the EGSnrc package are used for modeling particle interactions with linac components and patient anatomy respectively. Each has an associated right handed coordinate system.

(i) The BEAMnrc coordinate system is used for MC simulation of radiation transport through the linac components, and is attached to the collimator. The generated MC phase space contains the locations and directions of the particles from the simulated linac head.

(ii) DOSXYZnrc uses polar coordinate parameters θ and φ to define the source direction relative to isocenter (Figure A.3). Rotation of the phase space in the collimator plane is given by a third parameter φ_{col}. Since it uses a different coordinate system than BEAMnrc, DOSXYZnrc applies the parameters $(\theta, \varphi, \varphi_{col})_{DOSXYZ}$ with its own internal coordinate transformation when using a MC phase space generated by BEAMnrc. The vector $(x_{iso}, y_{iso}, z_{iso})_{DICOMp}$ defines the position of isocenter in the patient coordinate system used by DOSXYZnrc, and the scalar d_{source}

is the distance from $(x_{iso}, y_{iso}, z_{iso})_{DICOMp}$ to the center of the phase space. Together these five parameters fully define the beam orientation relative to the patient in DOSXYZnrc (Figure A.3).

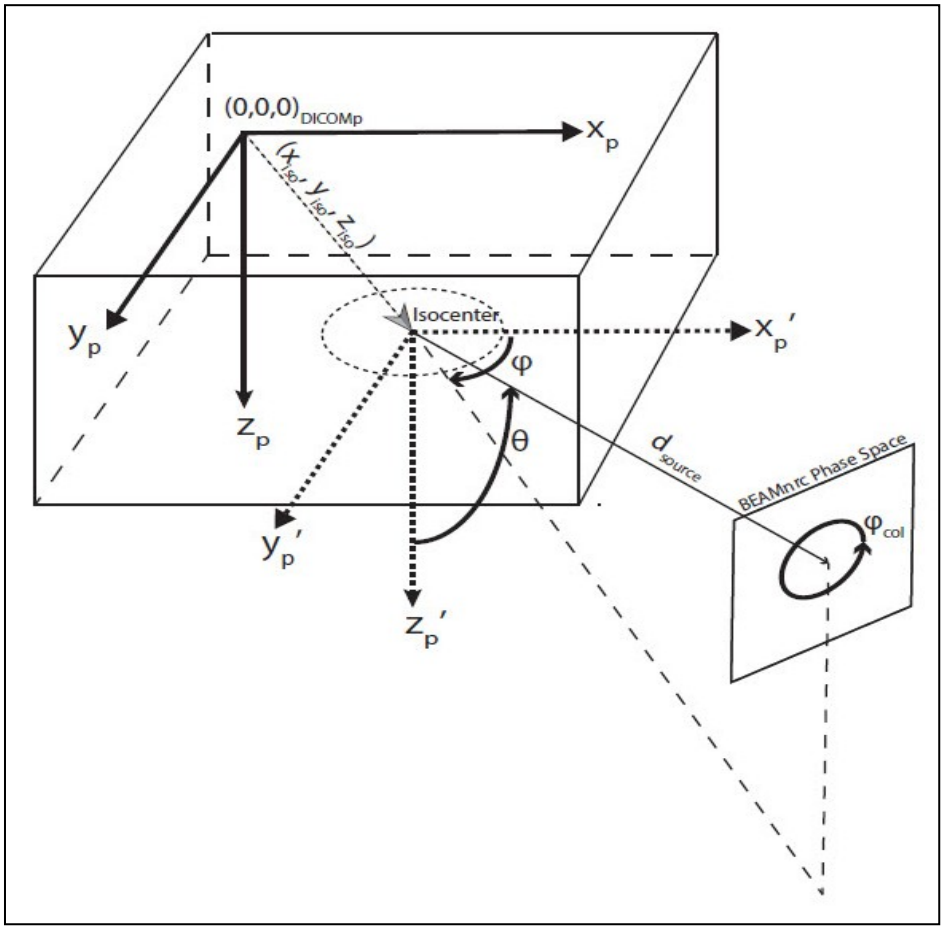

Figure A.3 DOSXYZnrc Cartesian/Polar Coordinate System diagram (isource=2)
Diagram shows: (i) DICOM patient coordinate system axes and origin ; (ii) Translation by $(x_{iso}, y_{iso}, z_{iso})_{DICOMp}$ to isocenter; (iii) Polar coordinate parameters $(\theta, \varphi, \varphi_{col})_{DOSXYZ}$ to describe beam direction, and distance d_{source} from isocenter to the center of the phase space.

A.3 Methods

In order to run the MC simulation, we must first generate density matrices for all four patient orientations. This requires modifications to the DOSXYZnrc module CTcreate, and is covered in section A. Then we must characterize the relationships between all of the involved coordinate

systems, and derive appropriate coordinate transformations. Figure A.4 below highlights the important relationships for each stage of this process.

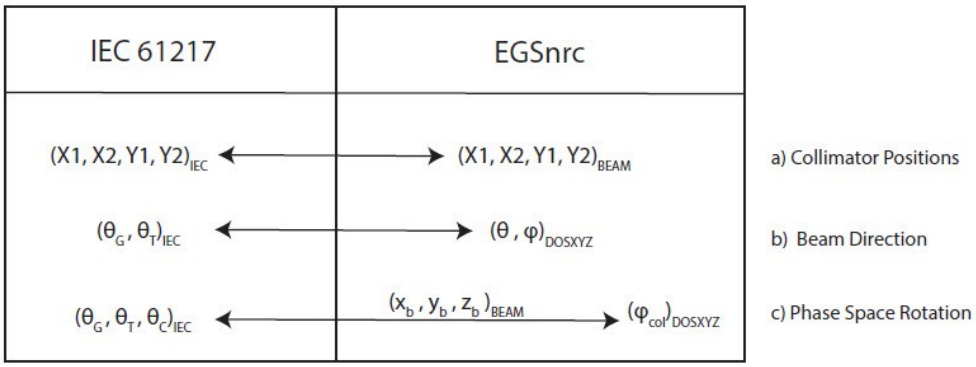

Figure A.4 EGSnrc and IEC Coordinate system parameters and their relations.

Section B.1 deals with relating the collimator positions defined in the TPS to their equivalent values in BEAMnrc, in order to generate the MC phase space which will serve as the particle source for the DOSXYZnrc simulation. At this stage we need to properly model both the source's direction and rotation. The coordinate transformation for beam direction in DOSXYZnrc will be derived in section B.2 using a rotation matrix approach, relating $(\theta, \phi)_{DOSXYZ}$ to $(\theta_G, \theta_T)_{IEC}$. The collimator rotation when using a BEAMnrc generated phase space is more complex, and involves not two but three coordinate systems. One must consider the relations between the IEC, BEAMnrc, and DOSXYZnrc coordinate systems, and the transformations in the DOSXYZnrc code applied to particles from a BEAMnrc phase space source. These relations will be dealt with in sections B.3 and B.4, respectively.

A.3.1 Generalizing CTcreate to other patient orientations

During our investigation, we discovered some undocumented limitations of CTcreate (1). CTcreate only generates density matrices correctly for a HFS patient orientation, and not for the less common orientations (HFP, FFS, FFP). CTcreate uses the DICOM tag "Image Position Patient" (0020,0032) for each CT slice to calculate the geometry of the resulting density matrix planes. This DICOM tag contains the coordinates in the patient coordinate system of the center of the first voxel (top left) for each slice. CTcreate assumes the corresponding values are the most negative coordinates in x and y, and then populates the planes of the CT data *in the positive direction* given the known number of voxels and their resolution. This assumption is only true for HFS; for other orientations the end of the CT data range is erroneously used as the starting point for the x and/or y directions, resulting in a range shifted by the field of view (FOV) width in that dimension.

Feet first cases are affected by another issue. When present, CTcreate uses the DICOM "Slice Location" (0020,1041) tag to populate the density matrix planes in the z direction. For patients scanned feet first, the slice location variable has the opposite sign relative to its value in the DICOM patient coordinate system defined in Image Position Patient. This results in an inverted density matrix range in z for feet first orientations. This inversion also affects the relation between the density matrix planes and the associated CT data for each voxel. Consequently, an incorrect subset of the CT data is used for generation of the density matrix in for feet first patient orientations.

CTcreate's use of the "Image Position Patient" DICOM attribute as the starting point for its density matrix planes results in an additional issue affecting *all* patient orientations, including HFS. In DOSXYZnrc, the planes define the boundaries (not centers) of the voxels. CTcreate

uses the center of the top left voxel as the starting point for its generated density matrix planes. Therefore, CTcreate-generated density matrices exhibit a half voxel shift in the x and y locations of the voxels. Interestingly, CTcreate does correctly account for this half voxel shift in the z direction.

As a result of these issues, the CTcreate density matrix generation for non-HFS patient orientations will be incorrect in 2 of the three directions. To overcome these limitations, we modified the source code to extract and use one more DICOM attribute, namely the "Patient Position" tag (0018,5100) defining the scanned patient orientation. The details of the required changes to CTcreate can be obtained by emailing the author.

A.3.2 Coordinate Transformations

A.3.2.1 Translating Collimator Positions from IEC to BEAMnrc

As illustrated in Figure A.5:

- The BEAMnrc coordinate system $+z_b$ axis points in the beam direction along the central axis, $+y_b$ points towards the Y1 jaw, and the $+x_b$ axis points towards the X2 jaw (8).
- The $+z_{IEC}$ axis of the beam limiting device IEC coordinate system points *towards* the radiation source (3).

Thus the $+x_b$ axis used in BEAMnrc is parallel, while the $+y_b$ and $+z_b$ axes are antiparallel, to those of the IEC beam limiting device coordinate system. Therefore TPS jaw positions defined by their distance from the central axis in the 2D isocenter plane are transformed to their equivalent BEAMnrc positions by *inverting the sign of the y coordinates*.

A.3.2.2 Derivation of EGSnrc Angles θ and ϕ

The next step is the transformation of TPS beam direction parameters $(\theta_G, \theta_T)_{IEC}$ to the EGSnrc angles $(\theta, \phi)_{DOSXYZ}$. This requires a series of non-commutative rotation matrices about the axes of a Cartesian coordinate system of the form

$$\mathbf{R}_x(\alpha) = \begin{pmatrix} 1 & 0 & 0 \\ 0 & \cos(\alpha) & -\sin(\alpha) \\ 0 & \sin(\alpha) & \cos(\alpha) \end{pmatrix} \quad \text{Equation A.1a}$$

$$\mathbf{R}_y(\beta) = \begin{pmatrix} \cos(\beta) & 0 & \sin(\beta) \\ 0 & 1 & 0 \\ -\sin(\beta) & 0 & \cos(\beta) \end{pmatrix} \quad \text{Equation A.1b}$$

$$\mathbf{R}_z(\gamma) = \begin{pmatrix} \cos(\gamma) & -\sin(\gamma) & 0 \\ \sin(\gamma) & \cos(\gamma) & 0 \\ 0 & 0 & 1 \end{pmatrix} \quad \text{Equation A.1c}$$

resulting in a transformation matrix **T,**

$$\mathbf{T} = \begin{pmatrix} T_{11} & T_{12} & T_{13} \\ T_{21} & T_{22} & T_{23} \\ T_{31} & T_{32} & T_{33} \end{pmatrix} \quad \text{Equation A.2}$$

Our method involves three distinct steps and rotation matrices. We begin in the DICOM patient coordinate system used by DOSXYZnrc, with a unit vector $(x_{p.}, y_p, z_p)_{DICOMp}=(0,0,1)$ described in polar coordinates by $(\theta, \phi)_{DOSXYZ}=(0,0)$. This unit vector is anti-parallel to the beam central axis, and is normal to the collimator plane. Referring to Figure A.2 will help to visualize the following steps:

1) The unit vector is rotated to the fixed IEC coordinate system linac position described by $\theta_G=0$, i.e. $(x_{f.}\ y_f, z_f)_{IEC}=(0,0,1)$.

2) The phase space is then rotated about the $+z_p$ axis in order to account for the gantry's motion, by the angle θ_G. Note that although this rotation is not in the plane of the physical gantry motion at this step, it will be rotated into the correct plane in the following step.
3) Finally, the phase space is rotated about $+y_p$ by θ_T to account for the couch motion.

After applying these rotations to the BEAMnrc phase space, DOSXYZnrc translates the vector to the DICOM patient coordinates of isocenter $(x_{iso}, y_{iso}, z_{iso})_{DICOMp}$ and scales it by d_{source} (although this step is done internally, and does not affect our coordinate transformations).

The resulting transformation matrices can be summarized by the equations below. The differences in these equations between the four patient orientations are simply sign changes of the argument of one or more of the rotation matrices. This is because two of the axes about which the rotations are taking place point in opposite directions when comparing the patient coordinate system axes between any of the 4 patient orientations (Figure A.2). The first rotation about $+x_p$ puts the phase space above the patient, this will be a $+\pi/2$ rotation for supine patients and a $-\pi/2$ rotation for prone patients. The second rotation accounts for the gantry rotation about the $+z_p$ axis, which points in opposite directions between the head-first and feet-first cases. The third rotation accounts for table motion about the $+y_p$ axis, which points in opposite directions between the supine and prone cases.

$$T_{HFS} = R_{y_p}(\theta_T)R_{z_p}(\theta_G)R_{x_p}\left(\frac{\pi}{2}\right) \qquad \text{Equation A.3a}$$

$$T_{HFP} = R_{y_p}(-\theta_T)R_{z_p}(\theta_G)R_{x_p}\left(-\frac{\pi}{2}\right) \qquad \text{Equation A.3b}$$

$$T_{FFS} = R_{y_p}(\theta_T)R_{z_p}(-\theta_G)R_{x_p}\left(\frac{\pi}{2}\right)$$ Equation A.3c

$$T_{FFP} = R_{y_p}(-\theta_T)R_{z_p}(-\theta_G)R_{x_p}\left(-\frac{\pi}{2}\right)$$ Equation A.3d

The elements of the transformation matrix **T** for all four patient orientations are provided in Table A.2.

	HFS	HFP	FFS	FFP
T_{11}	$\cos(\theta_T)\cos(\theta_G)$	$\cos(\theta_T)\cos(\theta_G)$	$\cos(\theta_T)\cos(\theta_G)$	$\cos(\theta_T)\cos(\theta_G)$
T_{12}	$\sin(\theta_T)$	$\sin(\theta_T)$	$\sin(\theta_T)$	$\sin(\theta_T)$
T_{13}	$\cos(\theta_T)\sin(\theta_G)$	$-\cos(\theta_T)\sin(\theta_G)$	$-\cos(\theta_T)\sin(\theta_G)$	$\cos(\theta_T)\sin(\theta_G)$
T_{21}	$\sin(\theta_G)$	$\sin(\theta_G)$	$-\sin(\theta_G)$	$-\sin(\theta_G)$
T_{22}	0	0	0	0
T_{23}	$-\cos(\theta_G)$	$\cos(\theta_G)$	$-\cos(\theta_G)$	$\cos(\theta_G)$
T_{31}	$-\sin(\theta_T)\cos(\theta_G)$	$\sin(\theta_T)\cos(\theta_G)$	$-\sin(\theta_T)\cos(\theta_G)$	$\sin(\theta_T)\cos(\theta_G)$
T_{32}	$\cos(\theta_T)$	$-\cos(\theta_T)$	$\cos(\theta_T)$	$-\cos(\theta_T)$
T_{33}	$-\sin(\theta_T)\sin(\theta_G)$	$-\sin(\theta_T)\sin(\theta_G)$	$\sin(\theta_T)\sin(\theta_G)$	$\sin(\theta_T)\sin(\theta_G)$

Table A.2 Transformation Matrix **T** elements

This method is similar to that described by Zhan et al (6), but is simplified, using three steps and rotation matrices rather than five. The additional two steps used by Zhan et al. account for collimator/phase space rotation in the transformation matrix. However, since the derivation of this matrix only serves to obtain the parameters describing the beam direction, these additional steps prove unnecessary: as expected conceptually, $(\theta, \phi)_{DOSXYZ}$ are functions of $(\theta_G, \theta_T)_{IEC}$ only.

The column $T_{13;}T_{23};T_{33}$ in Table A.2 is shaded in grey, because it is the only column which will affect our rotation of the unit vector describing beam direction in DOSXYZnrc ($x_{p.}$ y_p, z_p)=(0,0,1) discussed in section B.2. Notice that with our simplified version of this derivation there is no θ_C present in our transformation matrix, since it has no effect on the direction of the vector connecting isocenter to the center of our phase space. The resulting transformation for a HFS orientation obtained using our method is the same as published by Zhan et al.

The phase space for $\theta=\phi=0$ is initially aligned with the $+z_p$ axis, and can be described by the unit vector ($x_{p.}$ y_p, z_p)=(0,0,1). After applying the transformation matrix **T** to this unit vector, we obtain the resulting vector $\vec{v}$ defining the direction of the center of the phase space source from isocenter described by $(\theta_G, \theta_T)_{IEC}$.

$$\vec{v} = \begin{pmatrix} v_x \\ v_y \\ v_z \end{pmatrix} = \mathbf{T} \begin{pmatrix} 0 \\ 0 \\ 1 \end{pmatrix} = \begin{pmatrix} \cos(\theta_T)\sin(\theta_G) \\ -\cos(\theta_G) \\ -\sin(\theta_T)\sin(\theta_G) \end{pmatrix} \qquad \text{Equation A.4}$$

From the definitions of the polar and azimuthal angles in a spherical-polar coordinate system, Eq. 4 yields:

$$\theta_{HFS} = \cos^{-1}(v_z) = \cos^{-1}\left(-\sin(\theta_T)\sin(\theta_G)\right) \qquad \text{Equation A.5}$$

$$\phi_{HFS} = \tan^{-1}\left(\frac{v_y}{v_x}\right) = \tan^{-1}\left(\frac{-\cos(\theta_G)}{\cos(\theta_T)\sin(\theta_G)}\right) \qquad \text{Equation A.6}$$

It is important to note that the two argument arc-tangent function must be used in Equation A.6, which takes into account the sign of the numerator and denominator separately. The results of this derivation for all four patient orientations are shown below in Table A.3.

Patient Position	θ	φ
HFS	$\cos^{-1}\left(-\sin(\theta_T)\sin(\theta_G)\right)$	$\tan^{-1}\left(\frac{-\cos(\theta_G)}{\cos(\theta_T)\sin(\theta_G)}\right)$
HFP	$\cos^{-1}\left(-\sin(\theta_T)\sin(\theta_G)\right)$	$\tan^{-1}\left(\frac{\cos(\theta_G)}{-\cos(\theta_T)\sin(\theta_G)}\right)$
FFS	$\cos^{-1}\left(\sin(\theta_T)\sin(\theta_G)\right)$	$\tan^{-1}\left(\frac{-\cos(\theta_G)}{-\cos(\theta_T)\sin(\theta_G)}\right)$
FFP	$\cos^{-1}\left(\sin(\theta_T)\sin(\theta_G)\right)$	$\tan^{-1}\left(\frac{\cos(\theta_G)}{\cos(\theta_T)\sin(\theta_G)}\right)$

Table A.3 DOSXYZnrc Polar Coordinate Transformations: Coordinate transformations for DOSXYZnrc polar and azimuthal angles θ and ϕ for four studied patient orientations.

A.3.2.3 Phase Space Rotation: Transformation of $(\theta_G, \theta_T, \theta_C)_{IEC}$ to ϕ_{col}

Zhan et al. describes a method for projecting the couch rotation into the collimator plane in order to relate $(\theta_G, \theta_T, \theta_C)_{IEC}$ and ϕ_{col} in DOSXYZnrc (6). The result is shown in Equation A.7 below.

$$\varphi_{col} = \left(\theta_C - \frac{\pi}{2}\right) + \tan^{-1}\left(\frac{-\sin(\theta_T)\cos(\theta_G)}{\cos(\theta_T)}\right) \qquad \text{Equation A.7}$$

Zhan et al. adds that there is an additional conversion of Equation A.7 when using a BEAMnrc generated phase space (amounting to a sign change and a 180^0 shift), due to the difference in the BEAMnrc and DOSXYZnrc coordinate systems. An explanation for this additional conversion is not provided. In order to understand it, further consideration of the coordinate transformation applied within the DOSXYZnrc code when using a BEAMnrc phase space source is required.

A.3.2.4 DOSXYZnrc Internal Transformation for a BEAMnrc Phase Space Source

It was necessary to examine the DOSXYZnrc code to determine how the location and direction of each particle was being internally transformed from the phase space in the BEAMnrc coordinate system. The full transformation matrix $\mathbf{I}_{\text{BEAM>DOSXYZ}}$ found in the DOSXYZnrc code is shown in Table A.4 below.

Matrix Element	Equation
I_{11}	$\boldsymbol{cos(\varphi)cos(\theta)cos(\varphi_{col}) + sin(\varphi)sin(\varphi_{col})}$
I_{12}	$\boldsymbol{-cos(\varphi)cos(\theta)sin(\varphi_{col}) + sin(\varphi)cos(\varphi_{col})}$
I_{13}	$\boldsymbol{-cos(\varphi)sin(\theta)}$
I_{21}	$\boldsymbol{sin(\varphi)cos(\theta)cos(\varphi_{col}) - cos(\varphi)sin(\varphi_{col})}$
I_{22}	$\boldsymbol{-sin(\varphi)cos(\theta)sin(\varphi_{col}) - cos(\varphi)cos(\varphi_{col})}$
I_{23}	$\boldsymbol{-sin(\varphi)sin(\theta)}$
I_{31}	$\boldsymbol{-sin(\theta)cos(\varphi_{col})}$
I_{32}	$\boldsymbol{sin(\theta)sin(\varphi_{col})}$
I_{33}	$\boldsymbol{-cos(\theta)}$

Table A.4 DOSXYZnrc Internal Transformation Matrix I

We decomposed this single transformation matrix into 3 steps shown in Equation A.11 below:

$$I_{BEAM>DOSXYZ} = R_{z_p}(\pi+\varphi)R_{y_p}(\pi-\theta)R_{z_p}(\varphi_{col}) \qquad \text{Equation A.11}$$

The steps can be summarized as follows:

1) Rotate the initial values of the particle coordinates and directions (as defined in the BEAMnrc system) about the $+z_p$ axis by angle ϕ_{col} to account for collimator rotation.
2) Rotate coordinates/directions by angle $(\pi-\theta)$ about the $+y_p$ axis. This accounts for the fact that the $+z_b$ direction is the beam travel direction in BEAMnrc, whereas $+z_p$ is antiparallel to beam travel in DOSXYZnrc (for $\theta=\phi=0$). We therefore rotate by 180^0 to invert the direction of beam travel for DOSXYZnrc. We subtract θ from this rotation so that the phase space has the appropriate relation to the new DOSXYZnrc $+z_p$ axis, since in polar coordinates θ is the azimuthal angle which defines the declination from the +z axis.
3) Rotate coordinates/directions by angle $(\pi+\varphi)$ about the $+z_p$ axis. When performing a 180^0 rotation about one axis, the relative position of the other two axes become antiparallel to their initial positions. Since we inverted the direction of particle travel in step 2, we need an additional 180^0 rotation so that x and y coordinates of particles from the phase space have the appropriate relation to the linac jaws.

As a result of this internal coordinate transformation, a further modification to Equation A.7 is required when using a BEAMnrc generated phase space. For all four patient orientations the sign of ϕ_{col} is inverted due to the mapping of coordinates between BEAMnrc and DOSXYZnrc. This is because ϕ_{col} was derived to give the correct phase space rotation in DOSXYZnrc, but when

using a BEAMnrc phase space we immediately invert this rotation in step 2. In addition, this initial rotation of the phase space (step 1) using the parameter ϕ_{col} occurs about the $+z_p$ axis, which is pointing in the opposite direction between the head first and feet first cases (Figure A.2). Therefore the equations for ϕ_{col} for the head first and feet first cases differ by 180^0.

$$\varphi_{col}^{(beamHF)} = \pi - \phi_{col} = \frac{3\pi}{2} - \theta_C - \tan^{-1}\left(\frac{-\sin(\theta_T)\cos(\theta_G)}{\cos(\theta_T)}\right) \qquad \text{HFS \& HFP} \qquad \text{Equation A.12a}$$

$$\varphi_{col}^{(beamFF)} = -\phi_{col} = \frac{\pi}{2} - \theta_C - \tan^{-1}\left(\frac{-\sin(\theta_T)\cos(\theta_G)}{\cos(\theta_T)}\right) \qquad \text{FFS \& FFP} \qquad \text{Equation A.12b}$$

To summarize the use of the transformations: refer to chapter II section B.1 for translating collimator positions from the IEC to BEAMnrc coordinate systems; then, Equations *5, 6, and 12* for transforming the IEC parameters $(\theta_G, \theta_T, \theta_C)_{IEC}$ from the TPS to those used by DOSXYZnrc $(\theta, \varphi, \varphi_{col})_{DOSXYZ}$.

A.3.3 Test Cases

To validate our coordinate transformations, we made use of 8 test cases of increasing complexity shown in Table A.5 below. We first varied each of the three input parameters $(\theta_G, \theta_T, \theta_C)_{IEC}$ independently , then in combinations of two, and finally used three arbitrary angles. We chose an asymmetric $2x5cm^2$ field placed in quadrant one, i.e. $(X1,X2,Y1,Y2)_{IEC}$ = (0cm,5cm,0cm,2cm) with one corner adjacent to isocenter in order to avoid false positives due to rotational symmetry. For example, a square field centered on isocenter would have four-fold degeneracy of the resulting dose distribution for rotations of 90 degrees about the central axis.

Similarly a rectangular field centered on isocenter would have two fold degeneracy for rotations of 180^0 about the central axis. Geometric verification of the derived coordinate transformations were performed for all four patient orientations. BEAMnrc generated phase spaces were used in DOSXYZnrc, and MC simulations were run with one billion histories. The resulting dose distributions were then imported into the RayStation treatment planning software (9) and compared to the TPS dose calculation for geometric verification.

Test case	θ_G [deg]	θ_T [deg]	θ_C [deg]
1	0	0	0
2	0	0	270
3	0	270	0
4	290	0	0
5	270	0	270
6	120	90	60
7	270	180	120
8	160	70	220

Table A.5 Geometric Test Cases

A.4 Results

A.4.1 CTcreate Modifications

Density matrices for all four patient orientations were generated using both the original CTcreate code, as well as with our modified version. As seen shaded in grey in Table A.6 below, the original code results in errors for two of the three directions in the resulting density matrix range when used for non-HFS patient orientations. The ranges shifted by the FOV width due to misinterpretation of the starting point of the density matrix planes in x and/or y are present for all non-HFS orientations. The inverted ranges due to misinterpretation of the sign of the CT slice coordinates in z for both feet-first cases have an asterisk beside them. The half voxel error is

present in all x and y coordinates of the original density matrices. All of these errors are seen to be corrected by our modified CTcreate code.

		CTcreate Original	CTcreate Modified
HFS	x range [cm]	[-12.500, 12.500]	[-12.524,12.476]
	y range [cm]	[2.700,27.70]	[2.676,27.676]
	z range [cm]	[0.075,17.775]	[0.075,17.775]
HFP	x range [cm]	[12.500, 37.500]	[-12.479, 12.524]
	y range [cm]	[-2.700, 22.300]	[-27.676, -2.676]
	z range [cm]	[-11.950, 4.850]	[11.950, 4.850]
FFS	x range [cm]	[12.500, 37.500]	[-12.476, 12.524]
	y range [cm]	[2.700, 27.700]	[2.676, 27.676]
	z range [cm]	[0.300,16.500] *	[-16.500, -0.300]
FFP	x range [cm]	[-17.500, 17.500]	[-17.534, 17.466]
	y range [cm]	[2.300, 37.300]	[-32.666, 2.334]
	z range [cm]	[-0.200, 17.000] *	[-17.000, 0.200]

Table A.6 CTcreate Voxel Ranges

A.4.2 Coordinate Transformation Validation

Density matrices generated using our modified CT create code were used with our coordinate transformations in order to run MC simulations for all four patient orientations (HFS, HFP, FFS, FFP). Calculated dose distributions were read into the RayStation TPS and compared geometrically to the standard dose calculation in order to validate that both the beam direction and collimator rotation were correctly modeled using our transformations in DOSXYZnrc. All test cases passed our analysis for all patient orientations studied (32 cases total). Figure A.6 below shows a comparison of the default dose calculation beside the imported MC dose distribution for test case #8 with a FFP scanned and treated patient position. Both dose distributions agree geometrically, and align with the projected collimator edges in all three views (top: transverse ; bottom left : sagittal; bottom right: coronal).

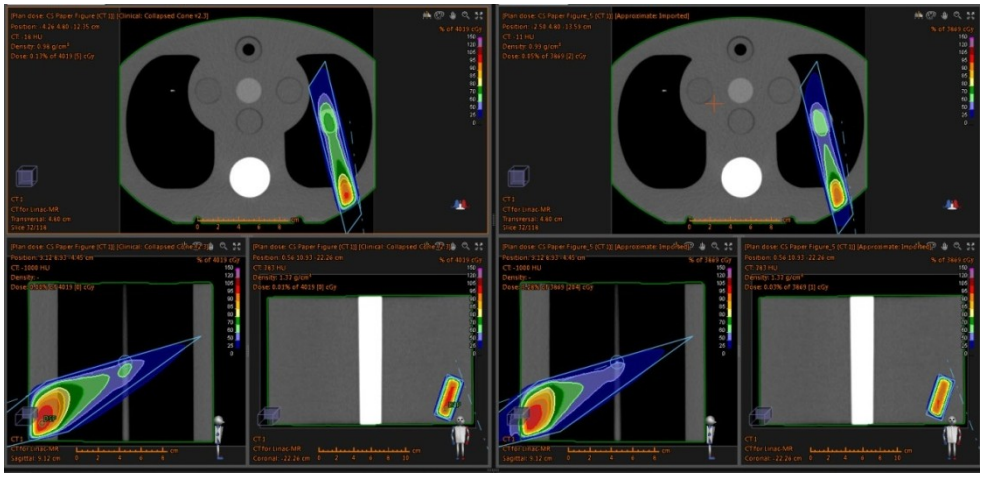

Figure A.6 Coordinate Transformation Validation for FFP patient orientation a) RayStation TPS default calculation (left) and b) MC simulated using DOSXYZ (right)

It is worth noting that the *scanned* patient position determines the DICOM patient coordinate system, and hence the density matrix generation, whereas the *treated* patient position determines the coordinate transformation to be used. For example, if a patient is scanned FFS, but is treated FFP, the FFP coordinate transformation must be used for the MC simulation.

A.5 Discussion & Conclusion

Several critical shortcomings of CTcreate when used for non-HFS patient orientations were identified and characterized. These shortcomings were corrected by modifying the CTcreate source code, and validated for all four patient orientations. A simpler method was proposed for deriving the coordinate transformations required for MC simulation of clinical treatment plans using EGSnrc and a BEAMnrc generated phase space. This derivation was performed for 3 additional standard patient orientations (HFP/FFS/FFP), and was validated using the EGSnrc Monte Carlo packages BEAMnrc and DOSXYZnrc. The subtle relationships between all relevant coordinate systems were studied in detail. Of particular interest was the way in which the derived parameters are applied within the DOSXYZnrc code to transform the coordinates of

particles from a BEAMnrc phase space. Study of this internal transformation provided understanding of the additional modifications to the transformation for φ_{col} when using a BEAMnrc phase space. The derived transformations were then validated using the RayStation TPS, and carefully chosen geometric test cases. The derived coordinate transformations and corrected CTcreate code will enable EGSnrc users to perform dosimetric verifications of clinical treatment plans for four commonly used patient orientations.

REFERENCES

1. Walters B, Kawrakow I, Rogers DWO. DOSXYZnrc UsersManual. Ottawa, ON, Canada: National Research Council of Canada; 2011.

2. Sherouse G. Coordinate transformation as a primary respresentation of radiotherapy beam geometry. Med Phys. 1991;19(1):175,176, 177,178, 179.

3. Radiotherapy equipment. Coordinates, movements and scales / Strahlentherapie-Einrichtungen. Koordinaten, Bewegungen und Skalen / Appareils utilisés en radiothérapie. Coordonnées, mouvements et échelles. [Internet]. BSI Standards Limited; 2012. Available from: http://login.ezproxy.library.ualberta.ca/login?url=http://search.ebscohost.com/login.aspx?direct=true&db=edsbsi&AN=edsbsi.30206861&site=eds-live&scope=site

4. Thebaut J, Zavgorodni S. Coordinate transformations for BEAM/EGSnrc Monte Carlo dose calculations of non-coplanar fields received from a DICOM-compliant treatment planning system. [Internet]. ; 2006. N441 p. Available from: http://login.ezproxy.library.ualberta.ca/login?url=http://search.ebscohost.com/login.aspx?direct=true&db=edswsc&AN=000242619200027&site=eds-live&scope=site

5. Bush KK, Zavgorodni SF. IEC accelerator beam coordinate transformations for clinical monte carlo simulation from a phase space or full BEAMnrc particle source. Australasian Physical & Engineering Sciences In Medicine [Internet]. 2010(4):351. Available from: http://login.ezproxy.library.ualberta.ca/login?url=http://search.ebscohost.com/login.aspx?direct=true&db=edsgao&AN=edsgcl.290638937&site=eds-live&scope=site

6. Zhan L, Jiang R, Osei EK. Beam coordinate transformations from DICOM to DOSXYZnrc. Phys Med Biol [Internet];57(24):N513-24. Available from: http://login.ezproxy.library.ualberta.ca/login?url=http://search.ebscohost.com/login.aspx?direct=true&db=edsbl&AN=RN330076882&site=eds-live&scope=site

7. Schmitz R, Telfer O, Townson R, Zavrgorodni SF. Generalized Coordinate Transformations for Monte Carlo (DOSXYZnrc and VMC++) verifications of DICOM compatible radiotherapy treatment plans.
arXiv:1406.0014v1 [physics.med-ph]
http://arxiv.org/ftp/arxiv/papers/1406/1406.0014.pdf

8. D.W.O. Rogers, B. Walters, I. Kawrakow. BEAMnrc Users Manual. Ottowa, ON, Canada: National Research Council of Canada; 2011.

9. RaySearch Laboratories. RayStation 3.0 Reference Manual. Stockholm, Sweden: ; 2012.

APPENDIX B:

Validation of modified EGSnrc codes

This appendix contains the details of the validation of the EGSnrc codes modified by Dr. Amir Keyvanloo from our research group at the Cross Cancer Institute. This consisted of three distinct components: 1) the validation of the BEAMnrc code that was modified to incorporate non-uniform 3D magnetic fields in the head of the linac ; 2) the validation of the dose deposited in DOSXYZnrc in the presence of magnetic fields ; 3) the validation of the DOSXYZnrc code modified to generate beamlet dose kernels in a bixelated geometry.

Part 1 was done by comparing the track for a single electron in vacuum for the modified EGSnrc code, to the GEANT4 (Monte Carlo) and OPERA-3D (finite element) simulation packages (1). This was done in the presence of both simple (uniform) and complex (3D varying) magnetic fields. For the simple case the gyroradii of the electrons differed by less than 1% from the analytical prediction for both GEANT4 and the modified BEAMnrc code, confirming their accurate modeling of electron transport (in vacuum) in the presence of uniform magnetic fields (1). For the complex magnetic field, Figure B.1 below shows the tracks of the electron for all three simulations (left), as well as the Euclidean distance between the tracks (right) (1) . The tracks for all three simulations overlap, with a maximum difference between electron tracks of ~0.8mm across 1200mm of travel in the z direction. This confirms that the modifications to the BEAMnrc code by Dr. Keyvanloo enabled accurate simulation of non-uniform magnetic fields, by benchmarking against other commonly used radiation transport simulation codes.

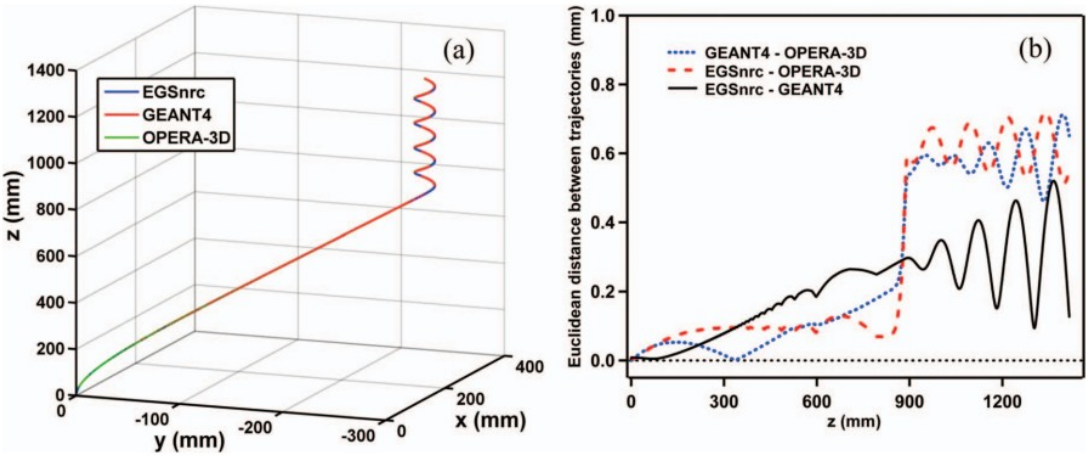

FIG. 4. (a) The electron trajectories from the EGSnrc, GEANT4, and OPERA-3D are shown in a 3D plot, where the electron originates at (0,0,0). (b) The Euclidean distance between the tracks in (a).

Figure B.1 Electron trajectories simulated in GEANT4, OPERA-3D, and modified EGSnrc in the presence of a complex 3D varying magnetic field. (left) Electron tracks for all three simulations originating at (0,0,0) shown in 3D plot ; (right) Euclidean distance between tracks. (1)

Part 2 was done by comparing the dose deposited in a 30x30x30cm^3 water tank by a 6MV 10x10cm^2 photon beam under the influence of a uniform 3T magnetic field (oriented either parallel and perpendicular to the beam direction). This scenario was simulated in both EGSnrc (DOSXYZnrc) and GEANT4, and the resulting dose distributions were compared using PDDs and central axis (CAX) dose profiles at various depths. This validation (unpublished) was done in house by Dr. Keyvanloo. Figure B.2 below shows the PDDs and CAX profiles at 1.25cm/15cm/27.5cm depths for the perpendicular magnetic field orientation. The curves for EGSnrc (red) and GEANT4 (blue) overlap in all four plots, confirming that the EGSnrc simulation results were consistent with GEANT4. GEANT4 has been experimentally validated in the presence of magnetic fields by Raaijmakers et al. (2) .

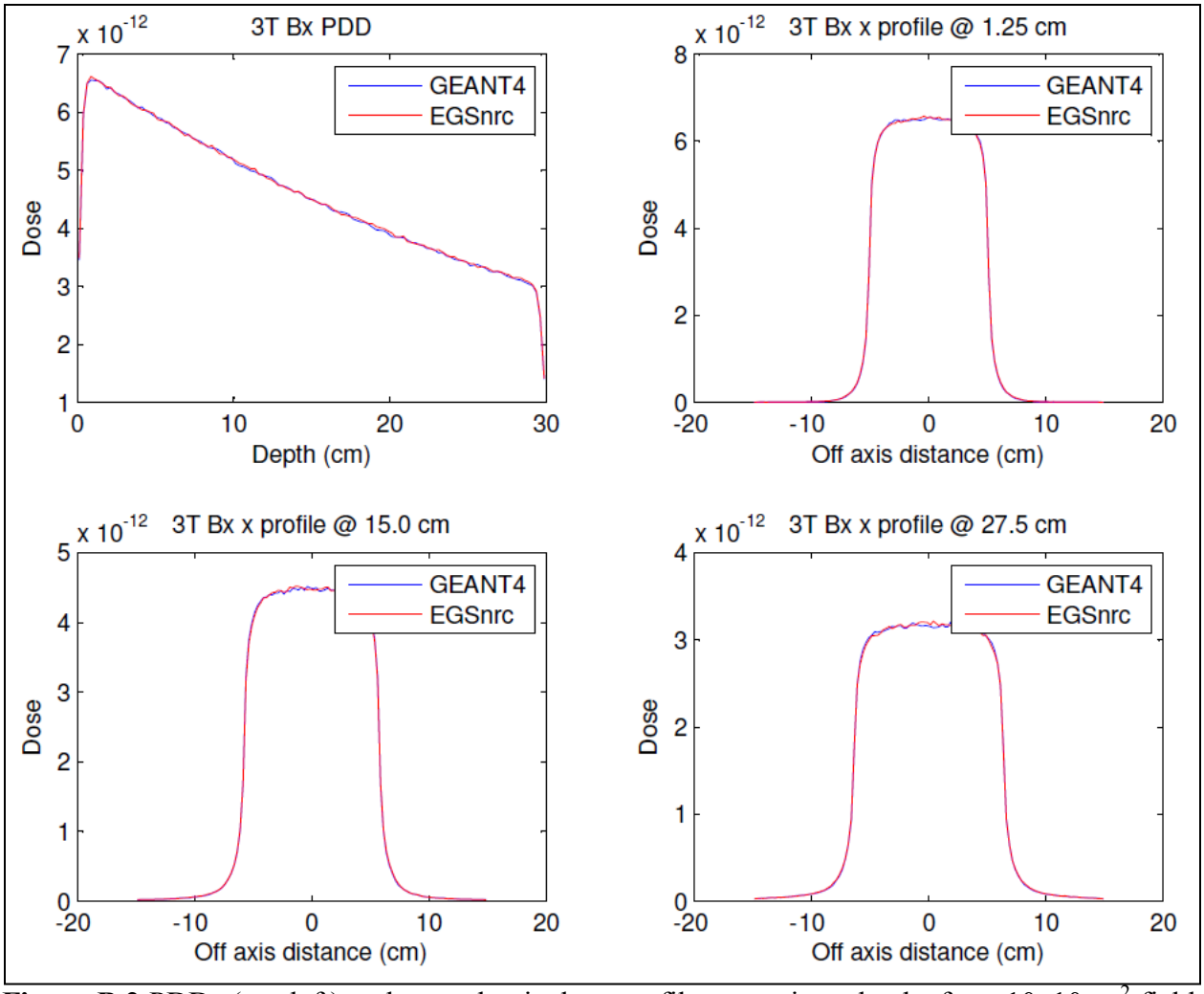

Figure B.2 PDDs (top left) and central axis dose profiles at various depths for a 10x10cm^2 field incident on a 30x30x30cm^3 water tank, under the influence of a 3T uniform magnetic field perpendicular to the beam direction. EGSnrc calculation in red, and GEANT4 calculation in blue.

Finally, part 3 was done by running simulations for a 6MV 10x10cm^2 photon beam on a 30x30x30cm^3 water tank using both the standard distributed version of DOSXYZnrc, and the modified beamlet-generating DOSXYZnrc. The resulting dose distributions were compared using PDDs, and CAX dose profiles at 1.5cm/10cm depths. Figure B.3 and B.4 below show the PDDs and CAX dose profiles respectively, for both the bixelated field and the standard EGSnrc code. The data from both simulations overlap in both Figures confirming that the modified EGSnrc beamlet was consistent with the standard distributions of EGSnrc. The average percent

difference for the PDD of modified EGSnrc simulation relative to the standard version was -0.1%, with a maximum percent difference of -0.4%. At 1.5cm depth, within the field edges the average difference for the X profile was 0% with a maximum percent difference of -0.4%. At 10 cm depth the average percent difference for the X profile was -0.1% with a maximum difference of -0.5%.

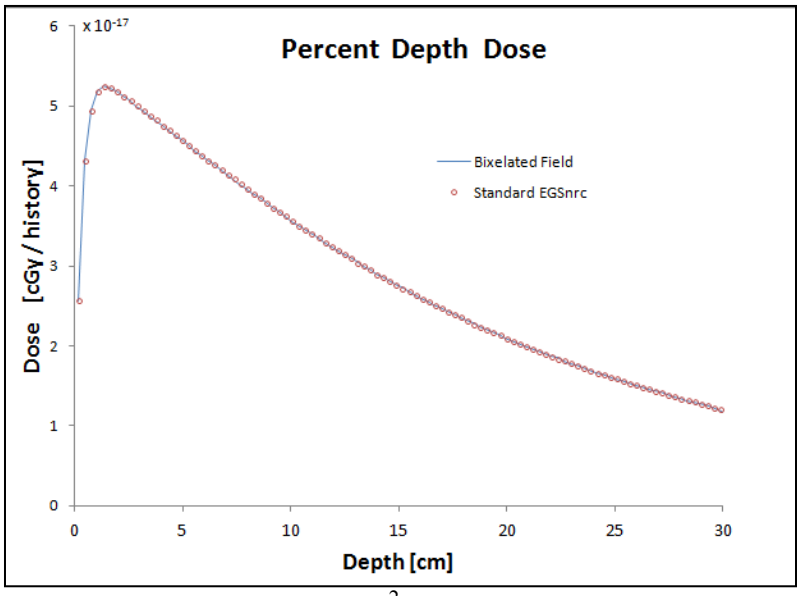

Figure B.3 Percent depth doses for a 10x10cm^2 photon beam incident on a 30x30x30cm^3 water tank. The dose from the modified EGSnrc code which bixelated the field is shown in blue, with the dose from the standard EGSnrc code overlayed in red.

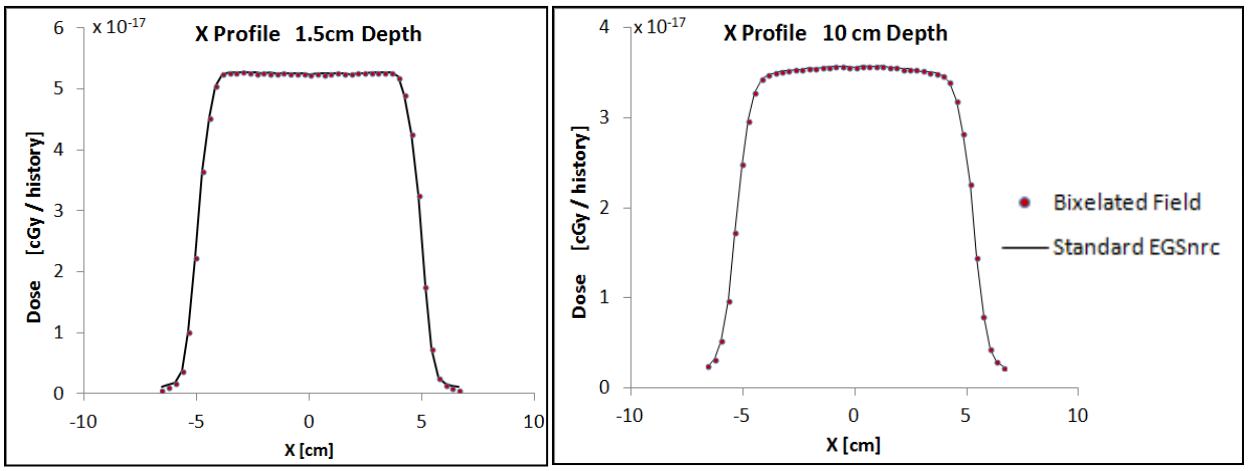

Figure B.4 CAX dose profiles at 1.5cm depth (left) and 10cm (right). The dose from the modified EGSnrc code which bixelated the field is shown as a blue line, with the dose from the standard EGSnrc code overlayed in red circles.

References

1. Keyvanloo A, Burke B, Warkentin B, Tadic T, Rathee S, Kirkby C, et al. Skin dose in longitudinal and transverse Linac-MRIs using Monte Carlo and realistic 3D MRI field models. Med Phys. 2012 Oct;39(10):6509-21.

2. Raaijmakers AJ, Raaymakers BW, Lagendijk JJ. Experimental verification of magnetic field dose effects for the MRI-accelerator. Phys Med Biol. 2007 Jul 21;52(14):4283-91.